Novel Remote Heart Rate Monitoring Systems Based on mm-Wave FMCW Radar

(ミリ波 FMCW レーダに基づく新型リモート心拍モニタリングシステム)

January 2024

Electrical Engineering Major

Graduate School of Science and Technology

Doctoral Course

Nihon University

HU YAOKUN

TABLE OF CONTENTS

LIST OF FIGURES

LIST OF TABLES

LIST OF ALGORITHMS

LIST OF SYMBOLS

$v(t)$	Relative velocity of the object and the radar
$f_{\mathrm{d}}(t)$	Doppler frequency
c	Speed of light
f_{c}	Carrier frequency of the radar transmitted signal
λ	Wavelength of the radar transmitted signal
f_{min}	Start frequency of chirp
f_{max}	End frequency of chirp
T_{c}	Chirp time
K_{s}	Slope of chirp
B	Sweeping bandwidth
$s_{\mathrm{t}}(t)$	Radar transmitted chirp signal
A_{t}	Magnitude related to the transmit power
t_{d}	Time delay
R_0	Distance between the radar and the subject
$s_{\mathrm{r}}(t)$	Radar received chirp signal
A_{r}	Magnitude related to the receive power
$s_{\mathrm{if}}(t)$	IF signal
f_{b}	Frequency of the IF signal
$\varphi(t)$	Phase of the IF signal
$x(t)$	Chest movement (radar vital sign)
$\varphi'(t)$	Phase extracted from the received complex signal

$R(t)$	Real part of the received complex signal
$I(t)$	Imaginary part of the received complex signal
dc_{r}	DC term of the real part of the received complex signal
dc_{i}	DC term of the imaginary part of the received complex signal
$\vec{s}_l$	Received signal
$\vec{p}_l$	Original signal
$\vec{n}_l$	Phase noise
L	Number of chirps per frame
φ	Phase after accumulation
A_{h}	Maximal chest displacement caused by heartbeat
A_{b}	Maximal chest displacement caused by breathing
f_{he}	Frequency of heartbeat
f_{be}	Frequency of breathing
n_{c}	Interference of the body's shaking and the clutter
$X(t)$	Radar vital sign after LI processing
$\mathrm{M}(\dots)$	Signal's local mean value
β_0	Noise amplitude coefficient of EMD
i	Number of times that noise is added to the original signal
$w^i(t)$	A realization of zero-mean white Gaussian noise
E_k	k th IMF decomposed by EMD
$\mathrm{IMF}_k(t)$	k th IMF
y_p	Heart rate measured by each observation window

o_p	Number of observation windows
$s^2(l)$	Peak value of the signal spectrum
$\sum s^2(f)$	Total energy of the signal spectrum
$\boldsymbol{D}_{\mathrm{i}}$	initial-DRM
$\alpha^{K}{}_{\mathrm{optimal}}$	Correct range bin cell at the beginning (K th frame)
$\alpha^{K+j}{}_{\mathrm{max}}$	Upper limits of the peak search range of $K+j$ th frame
$\alpha^{K+j}{}_{\mathrm{min}}$	Lower limits of the peak search range of $K+j$ th frame
$\alpha^{K+j}{}_{\mathrm{optimal}}$	Peak-seeking results of $K+j$ th frame
R_{bin}	Length of each range bin cell
$v^{K+j}{}_{\mathrm{m}}$	Instantaneous velocity of the subject from frame $K+(j-1)$ to the frame $K+j$
$\beta^{K+j}{}_{\mathrm{p}}$	Protection cells
η	Coefficient of protection cells
$v^{K+j}{}_{\mathrm{p}}$	Subject's velocity in frame $K+j$
$r_n(t)$	Residual of EMD
T_{r}	Rotation period
$\theta_{\mathrm{r}}^{kM+1}$	Rotation angle for frame $kM+1$
T_{f}	Frame period
$\boldsymbol{A}_{\mathrm{TCM}}^{kM+1}$	A target candidate matrix for frame $kM+1$
R_{kM+1}	Distance from the radar
v_{kM+1}	Instantaneous velocity information
θ	Instantaneous angle of the object

$\Delta\omega$	Phase difference
d	Pitch of the receiver antennas
$\theta_{\mathrm{a}}^{kM+1}$	An angle is formed by the initial and current radar orientations
$\boldsymbol{A}_{\mathrm{TM}}^{kM+1}$	A matrix including all target candidates within a specific range
$\boldsymbol{A}_{\mathrm{DM}}^{kM+1}$	Rotation decision matrix
$\bar{\theta}^{kM+1}$	Angle between the subject and the positive direction of the radar module
r_{s}^{kM+1}	Radius of the specific range
a_{s}	Subject's acceleration
β_{s}	Protection unit
θ_{s}	Rotation angle threshold value
θ_{step}	Step angle of the stepping motor
θ_{left}	Radar's horizontal left-half power angle
R_{min}	Minimum measurement distance
v_{p}	Speed at which the person moves under normal conditions
γ	Correlation coefficient
F	Data measured by the radar
E	ECG data used as a reference
μF	Mean of data measured by the radar
μE	Mean of ECG data
σF	Standard deviation of data measured by the radar
σE	Standard deviation of ECG data

HRR	Heart rates measured by each observation window
HRE	Reference heart rate (ECG data) for each observation window
R_{w}	Distance warning threshold
R_0^{kM+1}	Current distance exceeds the threshold value
θ_{t}	Threshold for direction adjustment
R_{maxd}	Range's upper thresholds
R_{mind}	Range's lower thresholds
H_{r}	Chest portion of the adult body from ground

Chapter 1 Introduction

1.1 Background

The heart rate originates from the sinus and atrioventricular nodes of the heart and is influenced by the sympathetic and parasympathetic nerves [1]. The heart rate is centrally related to the brain and is one of the four critical vital signs of the human body. Heart rate variability contains information on the regulation of the cardiovascular system by neurohumoral factors, which may be a valuable predictor of sudden cardiac death and arrhythmic events [2].

Population aging is a concern for humanity, and according to a 2019 survey, Japan's population aging rate was the highest in the world, at 27% [3]. The number of seniors living alone and in nursing homes is rising because of longevity. Additionally, the chance of isolation is increased by the presence of COVID-19. Thus, it is difficult to detect potential medical problems in the body of a senior person. However, cardiovascular disease is the primary cause of death in Japan, accounting for 25.5% of all deaths [4]. The development of an indoor heart rate monitoring system for older people living alone is urgently needed because of this growing social issue.

The conventional techniques for measuring the heart rate in contact include finger pressure pulse measurement, electrocardiography (ECG), photoplethysmography, and phonocardiography [5]-[8]. However, contact measures are inappropriate for continuous, round-the-clock monitoring, which

may be an inconvenient daily [9]-[10]. Additionally, wearing these devices may not be appropriate for seniors with skin issues. Therefore, research on non-contact radar-based heart rate measurements has recently gained popularity.

The principle of radar-based vital signs monitoring technology is that electromagnetic waves transmitted by radar are reflected off the subject's chest and received by the receiver antenna to create the IF signal. The IF signal contains information on the displacement of the subject, and the chest area oscillates at a certain frequency due to the movement of the lungs and heart. Therefore, by processing the IF signal with an appropriate algorithm, the respiration and heartbeat signals can be extracted.

Radar-based vital signs monitoring technology has a wide range of applications, including indoor medical monitoring applications and disaster relief, because it is capable of long-range, long-duration detection and is less affected by environmental factors such as weather and light.

Applications in the field of medical health care monitoring:

A. Health monitoring for home use

Older people and infants are not likely to be able to contact their families promptly in the event of physical abnormalities, and their families are not always around 24 hours a day. Therefore, a device that monitors the physical condition of older people and infants instead of the family is expected. Respiration and heart rate are important parameters that reflect the normal activity of essential functions of the human body, and it is

known that older people and infants are likely to experience rapid changes in respiration and heart rate when their physical condition becomes abnormal. Radar-based vital signs monitoring technology is ideal for home monitoring of the elderly and infants because it can perform non-contact detection over long distances and provide timely feedback of respiration and heart rate information with minimal interference to the subject.

B. Medical monitoring for hospitals

Some patients require hospitals to monitor their physiological changes for extended periods. Conventional detection devices are contact-type detection devices, and prolonged wearing of contact-type detection devices may cause discomfort to patients. On the other hand, non-contact vital signs detection technology using radar can effectively reduce patient discomfort caused by wearing a detection device for long periods. In addition, for some particular patients (e.g., severe burns and scalds), contact detection methods may cause a second injury, and the use of radar-based non-contact detection methods can avoid a second injury for particular patients.

Applications in the fields of disaster relief:

After a disaster strikes, radar-based biometric detection technology can help rescuers find survivors on time. For example, when disasters such as earthquakes, floods, building collapses, and forest fires occur, radar-

based, non-contact biometric detection devices can detect survivors in complex environments that are invisible to the naked eye. This technology can significantly improve the efficiency of disaster relief and reduce the loss.

1.2 Literature Review and Problems with Previous Technologies

Currently, the most commonly used radar types for non-contact vital sign monitoring are Continuous Wave Doppler Radar (CW-Doppler Radar), Impulse-Radio Ultra-Wideband Radar (IR-UWB Radar), and Frequency Modulated Continuous Wave Radar (FMCW Radar).

Continuous wave (CW) radar has long been used in many fields, such as vehicle speed measurement and storm tracking [11]. Before 2000, it had been applied in the field of biomedical signals. Dr. J. Lin of the Department of Electronics and Information Engineering at the University of Florida, USA, proposed the application of CW radar to detect vital signs as early as 1975 and successfully developed a vital signs detection system using CW radar [12]. The early radars were larger and more expensive for civilian use due to limitations in the manufacturing process and equipment such as antennas. However, nowadays, efforts are being made to develop portable measuring instruments with lower power consumption, lighter weight, and smaller size [13]. The research group of C. Li at Texas Tech University conducted much research on CW radar-based vital signs detection technology and developed a detection system using ka-band CW

radar in 2006 [14]; in 2008, a radar chip for vital signs detection using 0.18-micron CMOS technology was developed, enabling highly accurate estimation of a subject's respiration and heartbeat frequencies[15]; in 2010, a CW radar vital signs detection system using orthogonal demodulation architecture was proposed, which could achieve 80% detection accuracy at 2.5 m [16]; in 2017, a CW radar biometric detection system was proposed, which could achieve a long distance detection accuracy at a transmitting low-power continuous-wave radar vital signs detection system that can accurately measure long distances at -13 dBm power [17].

Compared to CW radar, UWB radar has ranging capability, more robust anti-jamming capability, and multi-target resolution. However, it has disadvantages, such as lower spectrum utilization efficiency and higher sampling rate requirements [18]-[19]. A. G. Yarovoy et al. at Delft University of Technology in the Netherlands started research on the application of UWB radar to detect human vital signs in 2006 [20]. In 2012, J. Li et al. proposed a UWB radar-based application for human vital signs detection through walls, and the designed system can measure the position of a subject through walls and detect vital signs [21].

FMCW radar combines the advantages of CW and UWB radar and has ranging, speed measurement capability, multi-target resolution, high sensitivity, and strong anti-jamming capability [22]-[23]. In 2009, L. Anitori started research on human vital signal detection using FMCW radar and presented a method to extract respiration and heartbeat signals by using the phase of IF signals [25]. FMCW radar system (center frequency 5.8 GHz, bandwidth 160 MHz) developed by Texas

Tech University in the U.S. successfully extracted respiratory and heartbeat signals [26]. 2015, F. Adib et al. at MIT achieved vital signal detection using FMCW radar at long distances with a maximum detection distance of 8 m [27]. In 2016, Ferreras studied the interference problem caused by the random motion of the human body in FMCW radar-based vital signal detection and proposed to place the radar in front of and behind the human body to sum the two IF signals and reduce the effect of random motion [28]. S. Wang in Germany developed an FMCW radar vital signal detection system with a center frequency of 80 GHz and a bandwidth of 10 GHz to obtain high distance resolution [29].

The wavelength of a 77 GHz FMCW radar is around 4 mm, and a minor movement might result in a substantial phase change of the IF signal. Therefore, mm-wave FMCW radar is also used in this study to attain great range accuracy.

In most radar-based vital sign estimation studies [9]-[29], subjects were required to remain stationary, such as standing, sitting on a chair, or lying on a bed. Measurements were made in a single direction. This facilitated the acquisition of displacement signals from the skin of the subject's body, which improved the measurement accuracy. However, maintaining a stationary state as a prerequisite for measurement limits the development and application prospects of radar-based vital sign monitoring systems. Therefore, there is a critical need for a method that can accurately measure the vital signs of moving targets.

Moreover, because of the radar characteristics, the measurement range may be constrained. It is challenging to cover the entire room, even with beamforming

techniques. When the angle is too large, the beam widens, the antenna gain drops, and the performance suffers. If there are several radars in the room, they can interfere with each other and increase background noise. Moreover, these methods increase the cost of the measurement system, which is not conducive to the popularity of the application.

Furthermore, the measurement accuracy decreases when the subject is far from the radar and obscured by other objects. Besides, the orientation and posture of the subject will affect the measurement results, so to enhance the robustness of the measurement, it is necessary to design a movable measurement system.

1.3 Research Objectives

A. To solve the problem of being able to measure only from the front or back of the person. There is a need to propose a method to improve the phase quality of IF signals for measurements made from multiple directions. The desired error should be less than 5 bpm (the value of most conventional measurement methods) when measuring from the front at 1 m from the radar. When measuring from other directions, the expected error should be less than 10 bpm.

B. To solve the problem of being able to measure only when the subject remains stationary. There is a need to propose a method to measure the heart rate of persons with a walking speed of about 1 m/s. The measurement accuracy should be more than 90%, and the high accuracy can be maintained when the target is within 5 m from the radar.

C. To solve the problem that the characteristics of the radar module limit the valid

measurement range. The proposed method should track the target accurately and adaptively change the measurement range of the radar. The proposed method should ensure that the target is within the optimal measurement range even when the target is walking laterally at a normal speed at a distance of 0.5 meters from the radar. Within 6 m of the radar origin, the proposed method should ensure that heart rate measurements are more than 90% accurate.

D. To solve the problem of measuring effectively when the subject is at a long distance. The proposed method should ensure that the target is not obscured by other objects or at a distance. The accuracy of heart rate measurements needs to be maintained above 90%.

E. To solve the problem of how to visualize and upload measurement results to the application in real-time. The developed application lets users check the target's current and past heart rate records in real-time.

1.4 Thesis Organization

In this thesis, some vital signs measurement methods [30]-[40] based on mm-wave FMCW radar proposed by the author are presented. These methods address the problems discussed at the end of subsection 1.2. The principle of FMCW radar-based vital sign detection is explained in Chapter 2. The PA-LI joint ICEEMDAN method described in Chapter 3 solves the problem of a single measurement direction. By using the improved adaptive range bin selection method described in Chapter 4, it is possible to measure a person’s heart rate while they are walking. A method using a stepping motor to change the orientation of the radar module,

which increases the effective measurement range to 360 degrees, is described in Chapter 5. A movable vital signs monitoring robot is presented in Chapter 6. A web application for uploading measurement data to the cloud for processing and visualization is presented in Chapter 7. Chapter 8 summarizes the entire article.

Chapter 2 Principle for Heart Rate Monitoring

2.1 Doppler Effect

The Doppler effect is named in honor of the Austrian physicist and mathematician Christian Johann Doppler, who first proposed the theory in 1842. The wavelength of an object's radiation changes because of the relative motion of the wave source and the observer. In front of a moving wave source, the wave is compressed, the wavelength becomes shorter, and the frequency becomes higher (blueshift); the opposite effect occurs when behind a moving wave source. The wavelength becomes longer, and the frequency becomes lower (redshift); the higher the speed of the wave source, the greater the effect produced. Depending on how much the wave is redshift (or blueshift), the speed at which the wave source moves in the observation direction can be calculated.

Initially, the Doppler effect had applications only in fields related to acoustics, but now it is used regularly in electromagnetism as well. Assuming that there is relative motion between the object and the radar and its relative velocity is $v(t)$, the Doppler shift resulting from the motion of the measured target can be expressed as:

$$f_{\mathrm{d}}(t) = \frac{2f_{\mathrm{c}}}{\mathrm{c}} v(t) = \frac{2\big(v(t)\big)}{\lambda} \tag{2.1}$$

where c is the speed of light (3×10^8 m/s), $f_{\mathrm{d}}(t)$ is the Doppler frequency, f_{c} is the carrier frequency of the radar transmitted signal, and λ is the wavelength of the

radar transmitted signal.

2.2 FMCW Radar Principle for Heart Rate Monitoring

Fig. 2.1 shows a schematic representation of the FMCW radar-based vital signs measurement. The transmitted and received chirp signals of an FMCW radar in the frequency domain are shown in Fig. 2.2. Combining the above two figures shows that the ramp generator periodically outputs a chirp signal whose frequency increases linearly with time. Each chirp signal's frequency is swept linearly from $f_{\min}$ to $f_{\max}$ inside T_c, with a slope of K_s. Therefore, the chirp signal's sweeping bandwidth can be described as $B = f_{\max} - f_{\min} = K_s T_c$.

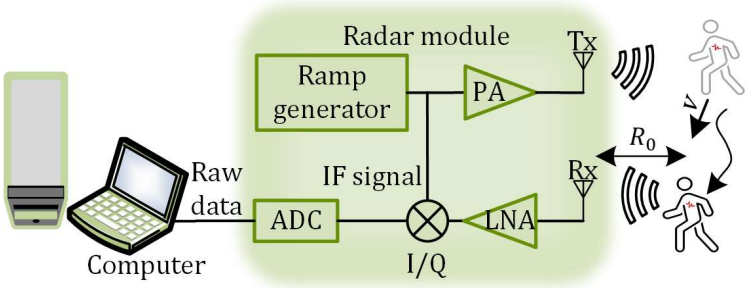

Fig. 2.1 The Block diagram of the FMCW radar module. The analog-to-digital converter, low-noise amplifier, and power amplifier are each denoted by the acronyms PA, LNA, and ADC. The computer receives the raw data to process the signals.

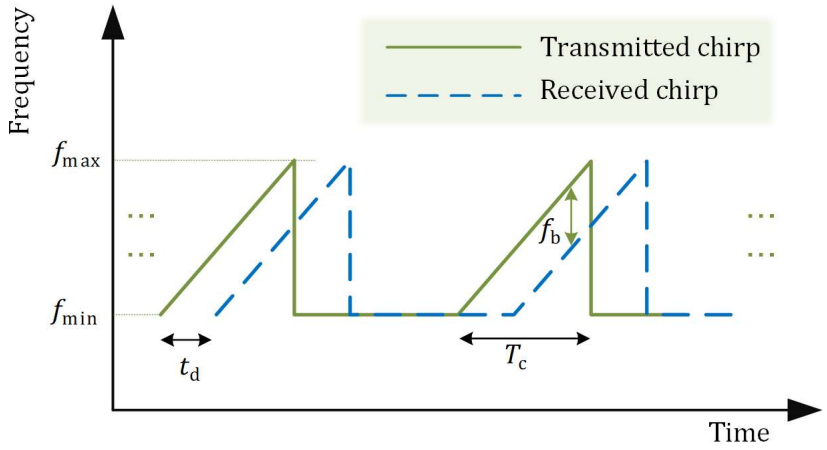

Fig. 2.2 The time-frequency diagram of the transmitted and received chirps.

The power amplifier amplifies the transmit chirp signal. The amplified signal will then be transmitted via the transmitter antenna. The received chirp signal is amplified by the low-noise amplifier (LNA) and correlated with the transmit signal via the I/Q (In-phase and Quadrature) mixer, which produces the IF signal. The in-phase and quadrature components of the IF signal are then sampled separately to generate the received complex signal to preserve its phase information, subsequently processed in a PC (i7-9700 CPU 3 GHz). The instantaneous frequency difference can be used to calculate the subject's distance from the radar.

In terms of mathematical formulas, the radar transmitted chirp signal is stated as follows:

$$s_{\mathrm{t}}(t) = A_{\mathrm{t}} \exp\left(j(2\pi f_{\min} t + \pi K_{\mathrm{s}} t^2)\right), 0 < t < T_{\mathrm{c}}, \tag{2.2}$$

where A_{t} denotes the magnitude related to the transmit power and $f_{\min}$ denotes the start frequency of the chirp. The transmitted signal is reflected on the subject and received with a time delay t_{d} and R_0 represents the distance between the radar and the subject. The relationship between t_{d} and R_0 is shown in Eq. 2.3.

$$t_{\mathrm{d}} = \frac{2R_0}{\mathrm{c}}, \tag{2.3}$$

where c represents the speed of light. The received chirp signal is $s_{\mathrm{r}}(t) = A_{\mathrm{r}} s_{\mathrm{t}}(t - t_{\mathrm{d}})$, where A_{r} has a relationship to A_{t} by radar equation. To summarize, the IF signal is defined by the equation below.

$$s_{\mathrm{if}}(t) = A_{\mathrm{t}} A_{\mathrm{r}} \exp\left(j\left(2\pi f_{\min} t_{\mathrm{d}} + 2\pi K_{\mathrm{s}} t_{\mathrm{d}} t - \pi K_{\mathrm{s}} t_{\mathrm{d}}^2\right)\right)$$

$$\approx A_{\mathrm{t}}A_{\mathrm{r}}\exp\left(j(2\pi f_{\min}t_{\mathrm{d}}+2\pi K_{\mathrm{s}}t_{\mathrm{d}}t)\right),\ t_{\mathrm{d}}<t<T_{\mathrm{c}}, \tag{2.4}$$

where $\pi K_{\mathrm{s}}t_{\mathrm{d}}^2$ in Eq. 2.4 can be omitted because it is tiny. By substituting Eq. 2.3 into Eq. 2.4, we can obtain the frequency and phase of the IF signal, which can be expressed as follows.

$$f_{\mathrm{b}}=\frac{2K_{\mathrm{s}}R_0}{\mathrm{c}},\qquad \varphi(t)=4\pi f_{\min}\frac{\left(R_0+x(t)\right)}{\mathrm{c}}, \tag{2.5}$$

where R_0 represents the instantaneous distance between the subject and the radar, and $x(t)$ represents the chest movement (radar vital sign) induced by breathing and heartbeat.

Chapter 3 Heart Rate Monitoring Using a PA-LI Joint ICEEMDAN Method for Stationary Subjects

3.1 Research Background for Chapter 3

The IF signal phase analysis can accurately measure the radar vital sign (human vital signs detected by the radar) in Chapter 2. The radar vital signs still include the body shaking of the subject and interference from other objects within the same range bin besides the subject's respiratory and heartbeat signals. A band-pass filter (BPF) is a common way of separating the respiratory and heartbeat signals from the radar vital sign. However, the frequency of breathing and heart rate are very close; the heart rate is interfered with by the harmonic of the respiratory signal, and it cannot be solved by BPF [41]. On the other hand, the authors of [17], [42] employed wavelet transform (WT) to extract the heartbeat signal. However, the heart rate varies from person to person, making the basic function of WT challenging to pick.

A time-frequency domain analysis of the radar vital sign is performed to resolve the abovementioned concerns. Empirical mode decomposition (EMD) was proposed by Huang N.E. et al. in 1998, which is an adaptive signal processing method to analyze nonlinear and non-stationary signals [43]. In [44]-[46], they employed EMD or EEMD to measure heart rate using radar. Nonetheless, the EMD method is constrained by the phenomena of "mode mixing." EEMD [47] was

presented as an improved EMD approach that resolves the problem by adding white Gaussian noise. However, EEMD has one major flaw: the decomposed signal contains residual noise. The issues discussed above might lead to instability in heart rate estimates. M.E. Torres et al. presented the complete ensemble empirical mode decomposition with adaptive noise (CEEMDAN) in 2011 [48]. By including adaptive white noise throughout each decomposition stage, this technique can eliminate the residual noise issue. Despite that, CEEMDAN still has some shortcomings, such as the signal information appears "later" than in EEMD with some "spurious" modes in the early stages of the decomposition. Three years later, an improved complete ensemble empirical mode decomposition with adaptive noise (ICEEMDAN) method was presented in [49]. This method can handle the problem of "mode mixing" without producing "spurious" modes and the residual noise. Therefore, we applied the ICEEMDAN method to perform time-frequency domain analysis on the radar vital sign [31]-[32]. However, because the heart intrinsic mode function (IMF) decomposed using the conventional ICEEMDAN method does not always have a high SNR, finding the peak and estimating the heart rate might be problematic.

Prior to time-frequency domain analysis, we presented a phase accumulation-linear interpolation (PA-LI) processing for FMCW radar signals. This approach can boost the SNR of the original signal fast and effectively, making it easier to detect the peak value of the heart IMF spectrum. In addition, the PA-LI technique's validity was established in combination with the EEMD method [30].

According to the advantages of the ICEEMDAN method and the PA-LI method discussed above. This is the first attempt to employ the PA-LI joint ICEEMDAN method to estimate the heart rate.

In terms of experimentation, most studies, such as paper [24], [50], had their subjects lying on the bed or sitting in a chair, and they monitored the heart rate solely from the front of the item. The authors of [14], [29], [51] took measurements from multiple horizontal directions (e.g., front, back, left, and right). In [52], T. Sakamoto et al. measured the heart rate from the top of the head. This study utilize the suggested measurement technique to estimate heart rate from multiple directions, assess the influence of different directions on the accuracy, and illustrate the validity and usefulness of the suggested approach.

3.2 PA-LI Joint ICEEMDAN Method

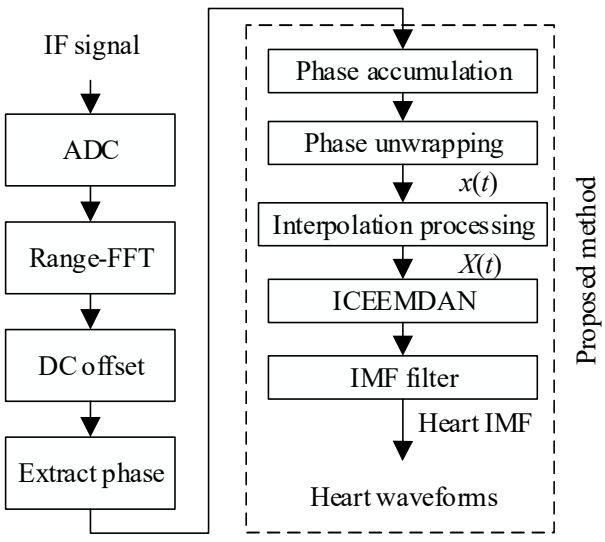

Fig. 3.1 Flow chart of the proposed signal processing.

The proposed method of vital signs monitoring is shown in Fig. 3.1. This study assumes that each IF signal (received complex signal) is sampled m points by the ADC, and the total number of chirps for the whole measurement period is n_{chirp}. Following ADC sampling, the range-FFT computation is performed on the received complex matrix ($[m, n_{\text{chirp}}]$) along the fast-time dimension to get a range profile matrix (RPM), which comprises subject's distance information. The surface weak vibration of the subject may then be detected by extracting the phase of the range-bin in which the subject is located. However, the DC term of the received complex signal is created by leakage from Tx to Rx, which interferes with the phase quality [53]. This indicates that the phase $\varphi'(t)$ extracted from the received complex signal is not equal to the phase $\varphi(t)$ in Eq. 2.5, and their connection is shown as follows:

$$\varphi'(t) = \arctan\left(\frac{I(t) + dc_{\text{i}}}{R(t) + dc_{\text{r}}}\right) \neq \varphi(t), \tag{3.1}$$

where $R(t)$, $I(t)$, dc_{i}, and dc_{r} are the real part, the imaginary part, the DC term of the imaginary part, and the DC term of the real part of the received complex signal. To eliminate the DC term, we utilize nonlinear least squares (NLLS) to estimate the center of the discrete data on the received complex signal's constellation diagram and then move the center to the origin.

Next, the collected phase information is subjected to phase accumulation-linear interpolation (PA-LI) processing to reduce phase noise and increase the SNR of radar vital sign $x(t)$ [30]. Generally, measured phase change due to the chest

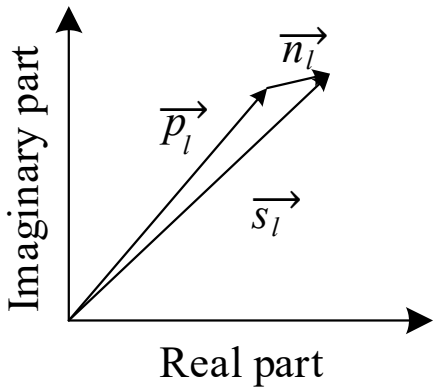

Fig. 3.2 Phase diagram of the received signal.

movement is very slow, and heart rate is 0.8-2.0 Hz under normal conditions. Therefore, in most studies, such as [24], [50], there is only one chirp in one frame, and the frame period is generally set at 50-100 ms according to the Nyquist-Shannon sampling theorem, corresponding to a sampling rate of 10-20 Hz (5-10 times the usual maximum heart rate). However, in the scenario, the time utilization is very poor due to the excessive idle time between frames. Besides, the phase analysis processes under highly non-linearity. Therefore, we proposed transmitting multiple chirps in each frame period and then accumulating all received signals in a single frame period to eliminate phase noise, called phase accumulation (PA) [30].

The phase diagram of the range-bin in which the subject is positioned is shown in Fig. 3.2, where $\vec{s}_l$, $\vec{p}_l$, and $\vec{n}_l$ represents the received signal, the original signal, and phase noise, respectively. The PA-LI processing is shown in Fig. 3.3, and we assume that the number of chirps per frame is L, and the phase after accumulation can be written as the follows:

$$\varphi = \arctan\{\langle(\vec{p}_l + \vec{n}_l)\rangle\}, \qquad l = 1, 2, 3 \ldots L, \tag{3.2}$$

where $\langle \ldots \rangle$ is the ensemble average of the data. Since $\vec{p}$ is essentially constant in a frame period and $\vec{n}$ is small and random, the effect of phase accumulation is that $\vec{p}$ will be amplified numerous times and $\vec{n}$ will cancel each other out, and it is minuscule compared to the accumulated $\vec{p}$. Both the DC offset and the PA methods deal with the signal phase, but the former applies to the entire measurement period or an observation window period, whilst the latter is done frame by frame.

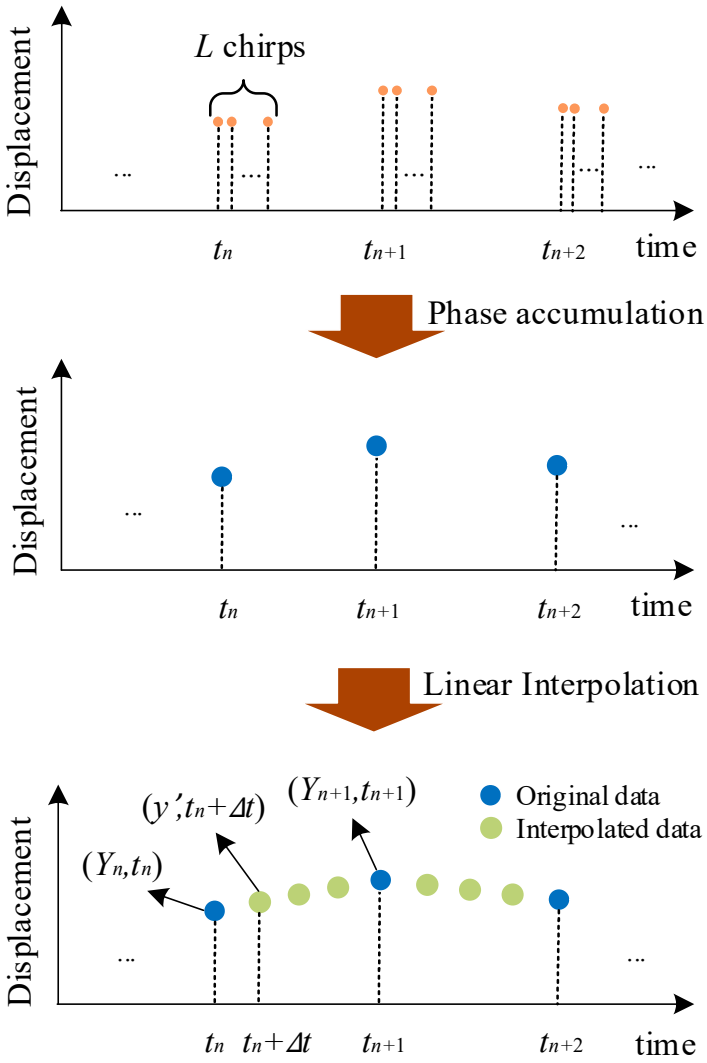

Fig. 3.3 Flow chart of PA-LI method.

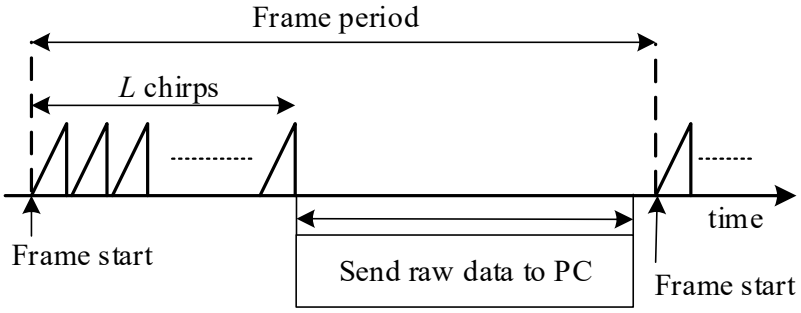

Fig. 3.4 Data transmission diagram of the FMCW Radar.

The phase data are unwrapped after phase accumulation to compute the radar vital sign $x(t)$, which can be written as the following formula:

$$x(t) = A_{\mathrm{h}}\sin(2\pi f_{\mathrm{he}}t) + A_{\mathrm{b}}\sin(2\pi f_{\mathrm{be}}t) + n_{\mathrm{c}}, \tag{3.3}$$

where A_{h},A_{b},f_{he}, and f_{be} represent the maximal chest displacement caused by heartbeat and breathing, and the frequency of heartbeat and breathing, respectively. n_{c} refers to the interference of the body's shaking and the clutter. The above parameters vary from person to person. Furthermore, a person's heart rate is not always consistent, and bodily shaking during the measurement is unavoidable. $x(t)$ is thus a non-linear and non-stationary signal.

To extract heartbeat signals with high SNR from $x(t)$, we apply linear interpolation (LI) on the collected $x(t)$ to enhance the sampling rate before performing ICEEMDAN processing because the movement of the chest is quite slow. As shown in Fig. 3.3, the ordinate value of a certain interpolation point between two adjacent original data is expressed as:

$$y' = Y_n + \Delta t\frac{Y_{n+1} - Y_n}{t_{n+1} - t_n}, \tag{3.4}$$

where Δt is the time elapsed between the interpolation point and the prior original

data. The radar vital sign is defined as $X(t)$ after LI processing. For two reasons, this does not contradict the previously indicated phase accumulation.

1. First, as shown in Fig. 3.4, the raw data in each frame period will be kept in the buffer and then sent to the PC once all of the chirps in the frame period have been transmitted. This means that when processing data from several frames directly, the data sampling rate is not consistent.
2. Second, due to the time used in data transmission, the frame period in the real experiment should not be shorter than 50 ms (the matching sampling rate cannot be higher than 20 Hz); otherwise, data loss is easily caused.

The previous work [30] indicates that when L is 32 and the sampling rate is 80 Hz, $X(t)$ has a high SNR. Therefore, we chose the optimal settings for this experiment from the above-mentioned.

Following PA-LI processing, we suggest using the ICEEMDAN method to adaptively decompose $X(t)$ into several IMF components and a residual component, followed by separation of the heartbeat signal from noises. The first IMF of $X(t)$ decomposed by EMD is

$$\mathrm{IMF}_1(t) = E_1\big(X(t)\big) = X(t) - \mathrm{M}\big(X(t)\big), \tag{3.5}$$

where $\mathrm{M}(\dots)$ is the signal's local mean value and $E_1(\dots)$ is the signal's first IMF of EMD. It is worth noting that compared to EEMD, ICEEMDAN does not directly add white Gaussian noise. Firstly, break down the white Gaussian noise with EMD, and then add the corresponding decomposed white Gaussian noise while computing the kth IMF of ICEEMDAN. So, the initial signal with noise may be

represented as:

$$X^{(i)}(t) = X(t) + \beta_0 E_1\left(w^i(t)\right), \qquad i = 1, 2, 3 \dots I, \tag{3.6}$$

where i is the number of times that noise is added to the original signal, β_0 is the noise amplitude coefficient, and $w^i(t)$ is a realization of zero-mean white Gaussian noise. The first IMF of $X(t)$ decomposed using ICEEMDAN is then expressed as follows:

$$\mathrm{IMF}_1(t) = \langle E_1\left(X^{(i)}(t)\right)\rangle = X(t) - \langle M\left(X^{(i)}(t)\right)\rangle. \tag{3.7}$$

In summary, the decomposition steps of ICEEMDAN are shown as follows:

1. Using EMD to decompose $X^{(i)}(t)$ to obtain the first residual component and the first IMF.

$$r_1(t) = \langle M\left(X^{(i)}(t)\right)\rangle, \quad \mathrm{IMF}_1(t) = X(t) - r_1(t). \tag{3.8}$$

2. Calculating the kth residual component.

$$r_k(t) = \langle M\left(r_{k-1}(t) + \beta_{k-1}E_k\left(w^i(t)\right)\right)\rangle, \qquad k = 2, 3, 4 \dots n, \tag{3.9}$$

where E_k is the kth IMF decomposed by EMD. β_{k-1} is the noise amplitude coefficient of the white Gaussian noise added during the kth decomposition and it is usually chosen to be 0.1-0.3 [54].

3. Calculating the kth IMF.

$$\mathrm{IMF}_k(t) = r_{k-1}(t) - r_k(t). \tag{3.10}$$

4. Repeat step 2 and 3 until a total of n IMFs and a residual component r_n are obtained, and the original signal can be illustrated by:

$$X(t) = \sum_{k=1}^{n} \mathrm{IMF}_k(t) + r_n(t), k = 1, 2, 3 \dots n. \quad (3.11)$$

After decomposing $X(t)$ with ICEEMDAN, we perform FFT spectrum analysis on all IMFs.

Under typical conditions, the volunteer's heart rate changes are not substantial during a single observation window cycle; therefore, the heartbeat signal is more concentrated in energy on the spectrum and has a single peak. Furthermore, the ICEEMDAN technique successfully solves the mode mixing problem, enabling the heartbeat signal to be decomposed into a single IMF. Even if an IMF is formed in the 0.8-2.0 Hz range by noise, mode mixing, and spurious modes, its SNR will be lower than the real heart IMF with a single peak. Therefore, the IMFs of peak frequency at 0.8-2.0 Hz are selected by the IMF filter, and the one with the highest SNR is the heart IMF for the heartbeat signal reconstruction. In addition, if no IMF whose peaks in this range or the SNR of the heart IMF from several consecutive observation windows is low, it is considered an abnormality. The system will output the IMF closest to the regular heart rate band as a result. This situation is extremely uncommon, and we believe that it will only occur when the subjects have an abnormal heart rate. Therefore, when the proposed heart rate measurement system is employed in actual medical monitoring, the SNR threshold of heart IMF will be set, and an alarm is sent if an abnormal condition arises.

3.3 Experiment

3.3.1 Hardware

Table 3.1 Radar parameters.

Parameters	Value
Bandwidth	3.99 GHz
Sweep time	57 μs
Frame period	100 ms
Slope	70 MHz/μs

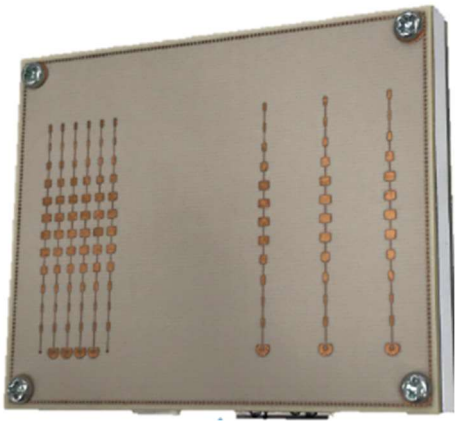

Fig. 3.5 The radar module based on a Texas Instruments IWR1443 chip.

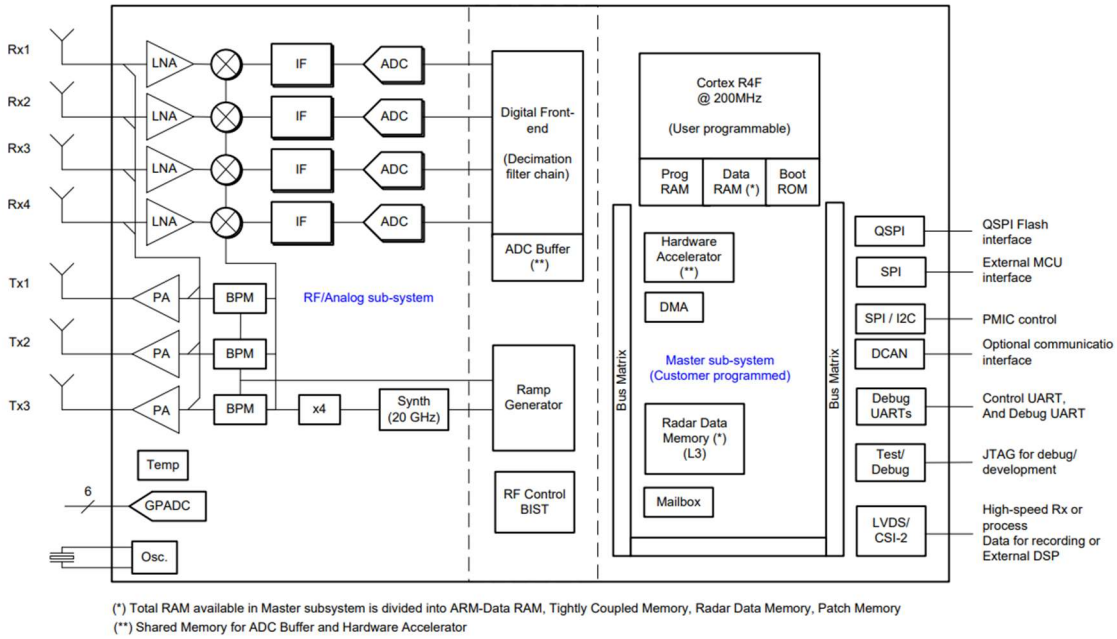

Fig. 3.6 The functional block diagram of the Texas Instruments IWR1443 chip.

The experiments employed an FMCW radar module (Fig. 3.5) based on the

Texas Instruments IWR1443 chip with an operational frequency range of 77 to 81 GHz, the functional block diagram is shown in Fig. 3.6. The maximum effective isotropic radiated power (EIRP) is 21 dBm, which complies with FCC regulations and will not hurt the human body. Besides, the radar module is allowed to be used according to the Japanese Radio Law. The parameters of the radar module are shown in Table 3.1.

3.3.2 Experimental Method

Table 3.2 Radar position.

Position	Elevation angle [°]	Distance [m]
Front	0	1
Front	0	1.5
Front	0	2
Front	30	1.5
Front	60	1.5
Front (Top)	90	1.3-1.5
Back	0	1
Left	0	1
Right	0	1

Four of volunteers (A height: 166 cm, weight: 60 kg; B height: 179 cm, weight: 64 kg; C height: 177 cm, weight: 75 kg; D height: 173 cm, weight: 60 kg) maintained a standing position during the heart rate measurements. As indicated in Table 3.2 and Fig. 3.7, the radar module was successively positioned in different places to investigate the influence of different measurement orientations on heart rate estimates. First, we measured one meter in front of the radar module and compared the findings to previous studies to demonstrate the reliability of our proposed method. Secondly, we take measurements through the radar module placed in front, behind, left, and right of the volunteers (distance: 1 m) and compare the results with and without PA-LI method to demonstrate PA-LI's

validity discussed in paper [30]. Next, the elevation angle between the volunteer and the radar module was held at 0 degrees. Its effect on the accuracy of the proposed method's heart rate measurements was tested by varying the distance between them (1 m, 1.5 m, 2 m). Finally, since the distance from the ceiling to the shoulder is about 1.5 m when a person is standing, we kept the distance between the radar module and the volunteer at 1.5 m. We varied the elevation angle between them (0˚, 30˚, 60˚, 90˚) to observe the effect of its variation on heart rate estimation. Some of the experimental scenarios are shown in Fig. 3.8.

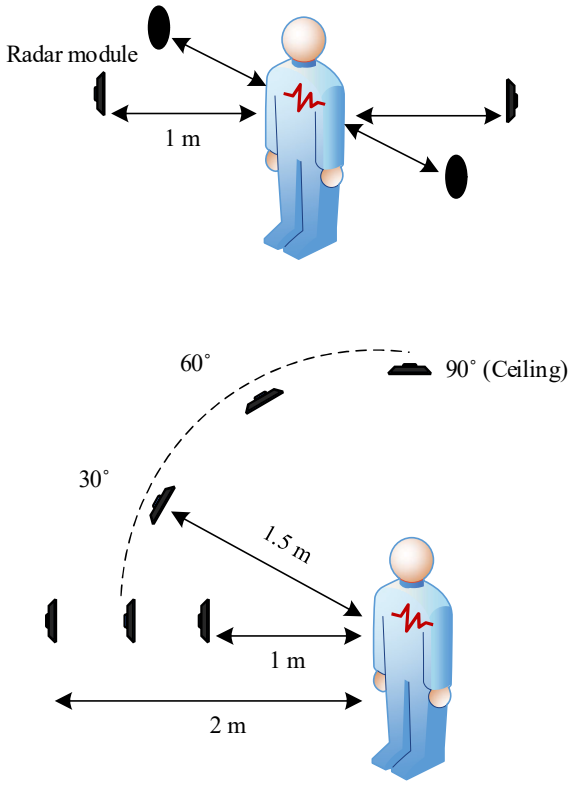

Fig. 3.7 A radar module was placed at 9 different positions for heart rate measurements, and only one volunteer was measured at the same time.

(a) Experimental scenario 1 (Distance: 1.5 m; Elevation angle: 60˚).

(b) Experimental scenario 2 (Distance: about 1.5 m; Elevation angle: 90˚).

Fig. 3.8 In (a) and (b), the radar module is fixed by a tripod or affixed to the ceiling, respectively. In (b), the distance between the radar module and the volunteer is kept at about 1.5 m, although it varies from person to person.

To obtain an accurate reference heartbeat signal, the volunteers wore an electrocardiogram (ECG) device during the measurement time of 60 s. Then, 60 s streaming data is analyzed with a 15 s observation window and a 1 s sliding step. Next, calculate each observation window's heart rate and compare it with the ECG data to obtain the root mean square error (RMSE). The definition of RMSE is shown in the following formula:

$$\text{RMSE} = \sqrt{\frac{1}{P}\sum_{P=1}^{P}\left(y_p - o_p\right)^2}, \qquad p = 1, 2, 3 \ldots P, \tag{3.12}$$

where P, y_p, and o_p are the number of observation windows, the heart rate measured by each observation window, and the reference heart rate, respectively. In this study, the definition of SNR is as follows:

$$\text{SNR} = 10\log\left(\frac{s^2(l)}{\sum s^2(f) - s^2(l)}\right), \tag{3.13}$$

where f and l are the index number corresponding to each frequency component and the peak of the signal spectrum, respectively. Therefore, $s^2(l)$ means the peak value of the signal spectrum and $\sum s^2(f)$ is the total energy of the signal spectrum.

3.3.3 Experimental Result

Table 3.3 Heart rate estimation results at 1 m from the radar module.
(RMSE: [bpm], SNR: [dB])

	Front				Back			
Subject	Without PA-LI		With PA-LI		Without PA-LI		With PA-LI	
	RMSE	SNR	RMSE	SNR	RMSE	SNR	RMSE	SNR
A	5.69	-12.98	4.09	-8.27	8.14	-10.15	5.95	-7.16
B	4.60	-13.12	2.61	-6.00	8.79	-12.70	4.60	-5.00
C	4.27	-15.06	2.59	-7.05	10.52	-12.29	7.30	-7.04
D	4.47	-10.57	3.01	-4.96	8.42	-9.88	6.45	-3.45
Mean	4.76	-12.93	3.08	-6.57	8.97	-11.26	6.08	-5.66
	Left				Right			
Subject	Without PA-LI		With PA-LI		Without PA-LI		With PA-LI	
	RMSE	SNR	RMSE	SNR	RMSE	SNR	RMSE	SNR
A	10.80	-13.44	5.90	-12.91	15.70	-5.73	19.66	-5.89
B	10.09	-22.87	7.77	-14.36	31.60	-17.43	21.67	-10.08
C	8.84	-17.32	6.02	-14.01	26.71	-10.37	25.55	-11.56
D	6.73	-12.95	5.95	-8.04	17.82	-6.31	18.89	-7.89
Mean	9.12	-16.65	6.41	-12.33	22.96	-9.96	21.44	-8.86

Table 3.4 Heart rate estimation results measured from directly in front of the radar module. (RMSE: [bpm], SNR: [dB])

Subject	Front 1 m		Front 1.5 m		Front 2 m	
	RMSE	SNR	RMSE	SNR	RMSE	SNR
A	4.09	-8.27	4.11	-9.79	5.62	-10.41
B	2.61	-6.00	5.69	-9.00	5.96	-12.48
C	2.59	-7.05	4.24	-10.74	5.32	-9.34
D	3.01	-4.96	5.17	-12.87	5.10	-11.03
Mean	3.08	-6.57	4.80	-10.60	5.50	-10.82

Table 3.5 Heart rate estimation results measured from the oblique front of the radar module. (RMSE: [bpm], SNR: [dB])

Subject	0˚		30˚		60˚		90˚ (ceiling)	
	RMSE	SNR	RMSE	SNR	RMSE	SNR	RMSE	SNR
A	4.11	-9.79	6.07	-13.29	6.27	-10.04	8.96	-11.28
B	5.69	-9.00	5.11	-10.69	6.21	-11.59	8.54	-12.73
C	4.24	-10.74	5.94	-14.54	5.93	-14.46	7.09	-15.00
D	5.17	-12.87	5.88	-14.39	5.22	-13.49	7.48	-15.73
Mean	4.80	-10.60	5.75	-13.23	5.91	-12.40	8.02	-13.69

The heart IMFs obtained by ICEEMDAN decomposition of the radar vital sign processed by PA-LI or without PA-LI are shown in Fig. 3.9. The findings reveal that the heart rates determined by ECG data, traditional ICEEMDAN, and the proposed method were 1.230 Hz, 1.200 Hz, and 1.067 Hz, respectively, with the accuracy of the two methods being around 86.7 percent and 97.7 percent. The suggested method's accuracy was 11.0 percent greater than the comparative method's. Since sometimes the heart IMF decomposed by the conventional ICEEMDAN method does not necessarily have a high SNR, it will be difficult to find the peak and estimate the heart rate. Instead, PA-LI can effectively increase the SNR of ICEEMDAN heart IMF and make it more accurate to find the heart

IMF spectrum's peak value. This is because the PA-LI method eliminates phase noise and increases the data length within a certain period of time to improve the SNR of the original signal.

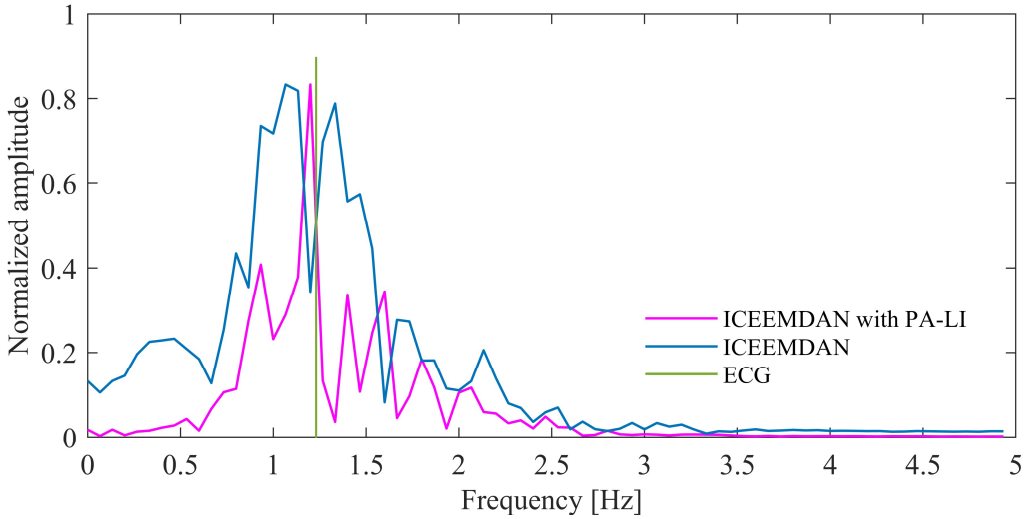

Fig. 3.9 The frequency spectrum of ICEEMDAN heart IMF of a certain observation window with or without PA-LI processing is shown in this figure.

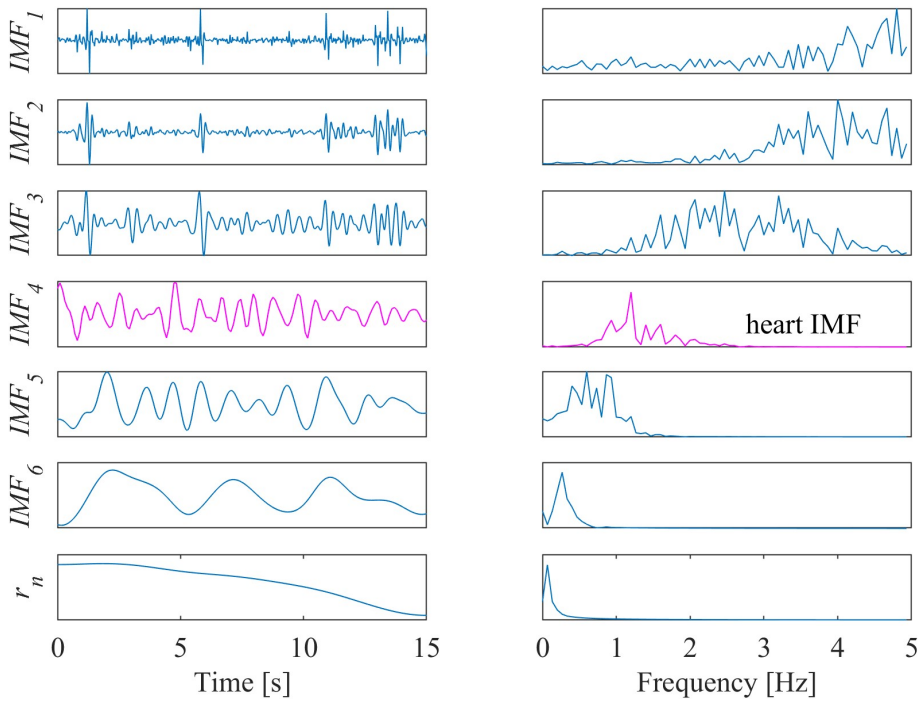

Fig. 3.10 The results of ICEEMDAN processing of the radar vital sign (measured from the front 1 m). The time-domain waveforms of each IMF and the final residual are shown on the left, and their corresponding frequency-domain is shown on the right.

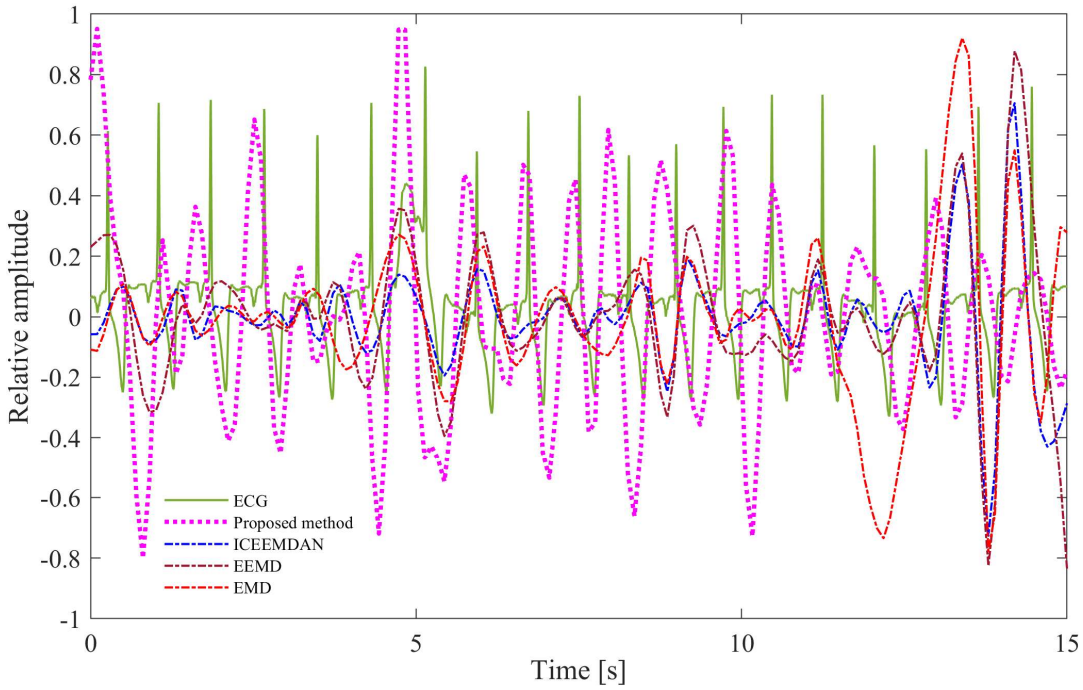

Fig. 3.11 Reconstructed heartbeat signals versus ECG waveform in the time domain.

We can also analyze the signal with a 15-second observation window rather than the 20-second observation window of [31], which improves system performance in real-time. The results of the ICEEMDAN decomposition of a certain observation window after the radar vital sign acquired by the proposed method are presented in Fig. 3.10. The peak frequency of IMF_4 (pink line) is within 0.8-2.0 Hz. In addition, as shown in Fig. 3.10, IMF_4 exhibits a high degree of consistency with the ECG signal in this observation window. Therefore, IMF_4 is the heart IMF of this observation window, and we utilize it to reconstruct the heartbeat signal.

The comparison of the reconstructed heartbeat signal obtained by the EMD, EEMD, ICEEMDAN, and proposed method with ECG data is shown in Fig. 3.11. For a single observation window, the proposed method and the comparative

methods had mean heart rate measurement accuracy of 97.7 percent, 86.7 percent (ICEEMDAN), 81.0 percent (EEMD), and 80.7 percent (EMD), respectively. The bpm (beats per minute) error of the heartbeat signal reconstructed by the proposed method is less than 1. Considering the radar module's own process manufacturing and loss issues may cause a slight measurement error. However, this small error is irresistible and acceptable. Because the RR interval (the time elapsed between two successive R waves of the QRS signal on the electrocardiogram) consistency with the ECG waveform is higher than that of the contrast methods.

The heart rate estimation results for the four directions 1 m away from the radar module are presented in Table 3.3, where the SNR is averaged over all observation windows. The results show that the mean values of SNR improved by 6.36 dB, 5.60 dB, and 4.32 dB when measured from the "front," the "back," and the "left" using the PA-LI method, and the mean values of RMSE of heart rate measurements decreased by 1.68 bpm, 2.89 bpm, and 2.71 bpm, respectively. This means that the PA-LI effectively improves the SNR and reduces the RMSE of the heart rate measurements. Heart rate was estimated from four directions using the proposed method, with the highest accuracy measured from the "front" and slightly higher accuracy measured from the "back" than the "left." It is noteworthy that the SNR of the heartbeat signal measured from the "back" is the highest among these conditions. This is supposed to be since the back's skin is less displaced, so the effect of breathing on the heart rate measurement is also reduced. However, this also results in heart rate estimates that are not as accurate as those from the "front."

Since the skin surface displacement due to the heartbeat is basically not detected from the “right,” the accuracy of the measurement from the “right” is not high, and the SNR loses its reference significance.

The heart rate measurements by the proposed method from the “front” direction different distances are shown in Table 3.4. The average value of the resulting RMSE shows that the measurement accuracy decreases with increasing distance. As the distance to the radar module increases, the SNR of the received signal will decrease, which affects the accuracy of heart rate measurement to some extent. In terms of the individual results, the degree of reduction in measurement accuracy is not absolute. The mean value of the RMSE of heart rate estimation when the distance was 1 m was 3.08 bpm. In [55], their error range of heart rate measurement of the stationary person was about -7 bpm to 5 bpm in one participant case, proving the reliability of our measurement system. In [56], their average absolute error of heart rate estimation was (2.61, 3.70, 2.12, 3.32, 4.42, mean: 3.23 [bpm]). Our measurement distance is farther than the 0.8 m they measured, and the performance is more stable. The proposed method in the paper [31] had an average RMSE of about 4.45 bpm measured from the front of 1.2 m. Therefore, in all three cases, the accuracy of heart rate measurement was maintained at a high level.

The heart rate estimation results at 1.5 m from the front of the radar module and at different elevation angles are presented in Table 3.5. Based on the results, it can be seen that the measurement accuracy decreases by about 1 bpm when the elevation angle is slightly increased, and the measurement accuracy does not

continue to decrease significantly as the elevation angle increases, and the RMSE remains at about 6 bpm. This is because the relative displacement between the chest and the radar module decreases when the elevation angle increases. When the radar module was fixed to the ceiling, the RMSE was about 8 bpm because the heartbeat produces less shoulder movement than chest movement. Despite this, measurement accuracy, in this case, exceeded the accuracy of heart rate measurements from the "back" and "left" sides based on the conventional ICEEMDAN method.

3.4 Summary of Chapter 3

This chapter proposes a PA-LI joint ICEEMDAN method for mm-wave FMCW radar-based heart rate measurement. The method can address the effects of respiratory signal harmonics, adaptively decompose the radar vital sign to extract the heartbeat signal and estimate the heart rate. Meanwhile, the PA-LI method can effectively increase the SNR of ICEEMDAN heart IMF and make it more accurate to find the heart IMF spectrum's peak value. Then, the reconstructed heartbeat signal has a high SNR, and the heart rate estimation is more accurate. Besides, we refined previous experimental approaches for investigating the influence of multi-directional observations on heart rate estimates. The experimental results show that the measurements' results in all directions (e.g., left, back, oblique front, and ceiling) are maintained at a high level of accuracy, except for the measurements from the "right" side, because the skin surface displacement (due to the heartbeat) is basically not detected from the "right" side. Considering that non-contact heart

rate measurement systems do not always face the subject in practice, in other words, the radar module is installed on the ceiling or high in the room to accommodate the real circumstance. Therefore, our proposed heart rate measurement method has the potential for practical applications.

Chapter 4 Remote Heart Rate Measurement of Walking Persons Using Improved Adaptive Range Bin Selection

4.1 Research Background for Chapter 4

In most radar-based vital sign estimation studies, subjects were required to remain stationary, such as standing, sitting on a chair, or lying on a bed [24], [29], [44], [50], [52], [55]-[57]. This facilitated the acquisition of displacement signals from the skin of the subject's body, which improved the measurement accuracy. However, maintaining a stationary state as a prerequisite for measurement limits the development and application prospects of radar-based vital-sign monitoring systems. Therefore, there is a critical need for a method that can accurately measure the vital signs of moving targets.

Some researchers have proposed using impulse-radio ultra-wideband (IR-UWB) radar-based methods to measure the heart rate of moving persons [59], [60]. However, their subjects moved slowly, and the experimental method was relatively simple. Furthermore, the signal energy levels that can be transmitted are not very high, which reduces the accuracy and signal-to-noise ratio (SNR) of IR-UWB radars [26]. CW Doppler radar is another common method for measuring heart rate [61]-[66]. However, owing to the lack of ranging capability in CW Doppler radar, measurements are susceptible to interference and are unsuitable for monitoring the vital signs of moving targets [67]. Therefore, an FMCW radar with good range and

speed measurement capability is an appropriate choice. Furthermore, the millimeter-band FMCW radar has high sensitivity, making it easy to detect tiny displacements on the surface of the skin.

A range profile matrix (RPM)-based motion compensation method using a millimeter-wave FMCW radar has been proposed to measure the heart rate of a moving person [68], [69]. The method obtains the subject's range bin cell premise to perform position correction. If there are other objects nearby, RPM peak-seeking will have difficulty correctly selecting the range bin cell where the subject is located. In addition, the subjects' average movement speed in paper [69] was only 0.01 m/s. The authors of paper [70] proposed a method for analyzing multiple range bins simultaneously. They used a 24 GHz band radar with a low range bin resolution to cover a range of 3 m with four range bins. However, the low range bin resolution may include other nontargets in a range bin cell near the subject. Owing to the high range bin resolution of millimeter-wave FMCW radar, hundreds of range bins must be processed simultaneously, which reduces the real-time performance of the measurement system.

Although there are many sophisticated tracking filters, the goal of this study is not to predict the target's position and tracking based on its current state. Instead, selecting a range bin based on the predicted value results in a secondary error. The key to extracting high-quality phase-change information for measuring vital signs is the quick and efficient selection of the range bin cell where the subject is located. Our previous work proposed an adaptive range bin selection method for millimeter-

wave FMCW radar to solve the abovementioned problem [35]. Instead of the manual post-processing form, this method automatically selects the optimal range bin cell for vital sign monitoring, and its effectiveness was demonstrated through experiments in which subjects walked back and forth in front of the radar module. Meanwhile, we proposed and evaluated methods for measuring heart rate from multiple orientations, which opens up the possibility of this research topic [32]. The adaptive range bin selection method will be improved in this study, and a comprehensive set of experimental methods will be devised to assess the accuracy and stability of the measurements. The subjects will have a maximum mean velocity of 1 m/s during the experiment and will be able to simultaneously measure the vital signs of multiple persons at the same time. Therefore, this is the first study to use FMCW radar to detect vital signs while human subjects walk at a normal speed.

4.2 Improved Adaptive Range Bin Selection

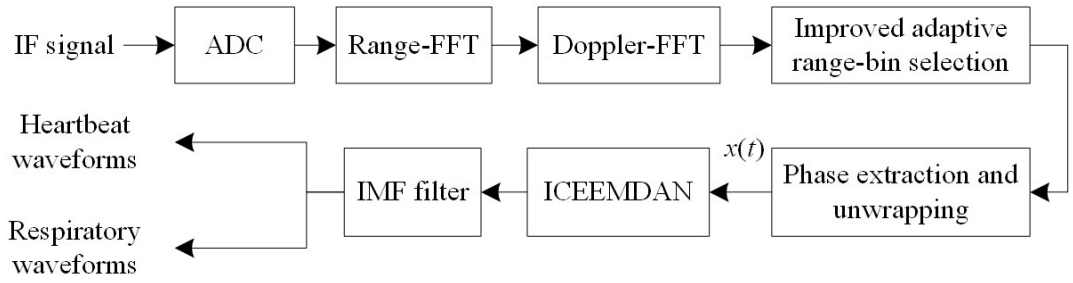

Fig. 4.1 Flow chart of the proposed signal processing.

A flow chart of the proposed signal processing method for vital sign measurements is shown in Fig 4.1. Raw data are generated in frames after the ADC samples the IF signal. The RPM can be obtained by performing a range-FFT along the fast time dimension. The change in the distance information of the target with

respect to time can be observed more intuitively by stitching the RPM of each frame along the slow time dimension. The horizontal coordinates of RPM represent the distance to the radar module. The distance represented by each range bin cell is fixed once the radar module and its configuration file are determined.

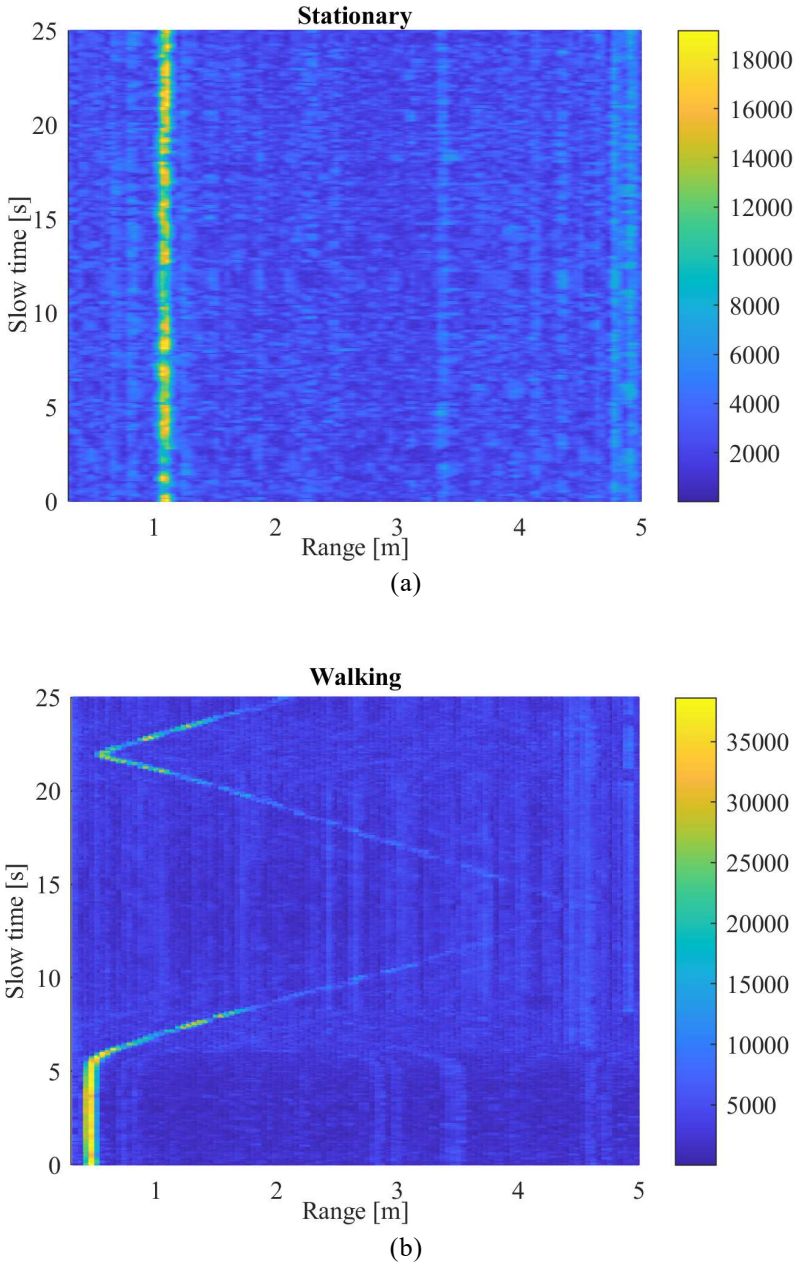

Fig. 4.2 A sample of Range profile matrix (stationary vs. walking).

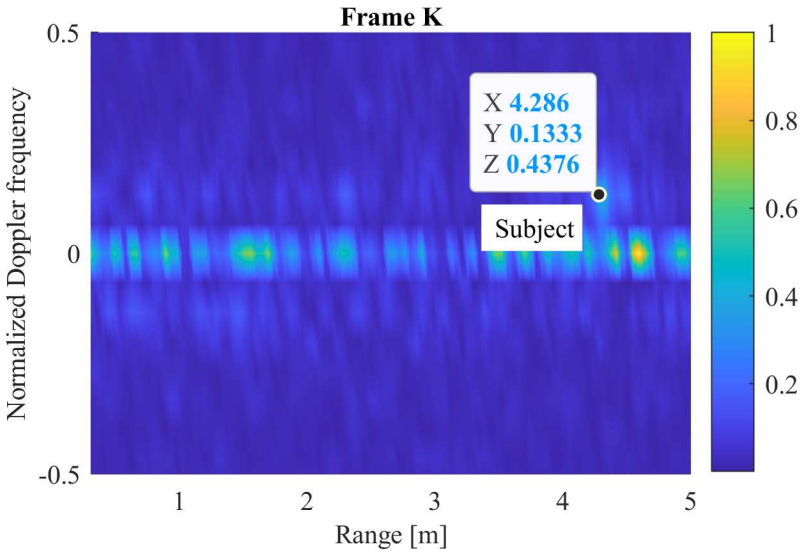

(a)

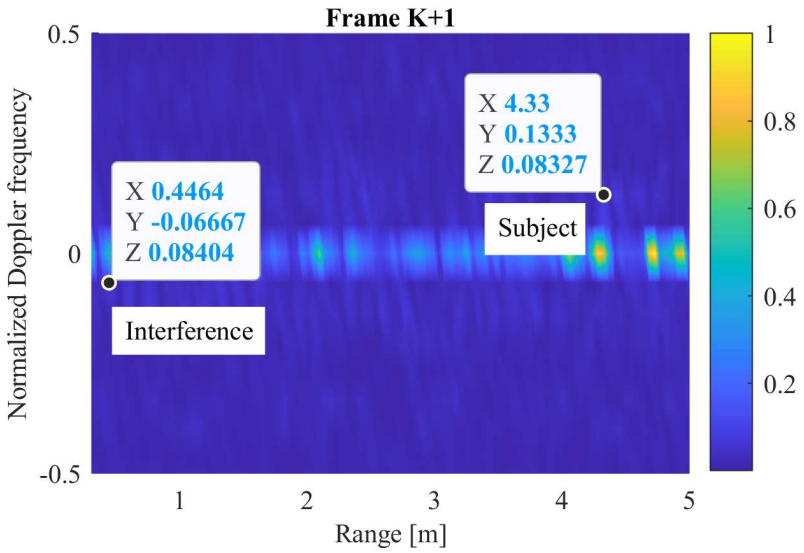

(b)

Fig. 4.3 Example of Doppler-range matrix for two consecutive frames. The interval between frames is 0.1 s, and the subject is gradually moving away from the radar module.

Most previous studies on radar-based heart rate measurements required subjects to remain stationary (sitting, standing, or lying down) during the measurement. The subject was approximately 1 m from the radar module, as shown in the upper figure of Fig. 4.2. In this case, the range bin cell where the subject is located can be easily

obtained by methods such as RPM peak finding. Moreover, once the range bin cell is identified, no adjustments are required throughout the measurement process. The phase-change information is then extracted from the most appropriate range bin cells along the time dimension, and it is unwrapped to calculate $x(t)$. By the way, in order to increase the time utilization per frame and improve the phase quality, we propose the PA-LI method of emitting multiple up-chirp signals in each frame [32]. Finally, the vital signs are typically extracted from the $x(t)$ using a band-pass filter, wavelet transform, or other means. These are the traditional radar-based vital sign measurements.

As discussed in the Introduction, there are limitations to the measurement methods mentioned above. Measurement becomes problematic when the subject walks instead of remaining stationary. As shown in the lower panel of Fig. 4.2, the subject walks back and forth between 0.5 m and 4.5 m from the radar module. In this case, continuous updating of the most suitable range bin cell is required to obtain the phase change information of the range bin cell where the subject is located during the measurement period. The extracted phase data are then stitched together along the time dimension.

RPM-based peak seeking is unstable because the reflected energy is lower when the subject is farther from the radar module. Even though the Doppler range matrix (DRM)-based peak-seeking method can separate the subject from most environmental noises using Doppler shift, there will probably be less energy than interference when the subject is far away. The DRM for two consecutive frames is

shown in Fig. 4.3. For a range outside the Doppler shift of 0, frame K can identify the range bin cell where the subject is located successfully. However, for frame K+1 after 0.1s, the peak-seeking result is the range bin cell containing the interference. The result causes an error of approximately 3.89 m, and this range bin cell does not contain information about the phase change caused by the subject's skin surface displacement.

There are already some mature methods for target tracking, such as particle filters and Kalman filters. However, the goal of this study is not to improve the accuracy of the subject location and predict its position, but rather to find a simple and efficient method to identify the appropriate range bin cells and thus extract the phase change information. By contrast, overly complex algorithms can reduce the real-time performance of measurement system.

Therefore, an improved novel adaptive range bin selection method is proposed in this study to solve the above problem. Meanwhile, this study employs the improved complete ensemble empirical mode decomposition with adaptive noise (ICEEMDAN) method to reconstruct the heartbeat and respiration signals.

A schematic diagram of the improved adaptive range bin selection method is shown in Fig. 4.4. Assuming that $\boldsymbol{L}$ up-chirp signals are emitted in each frame cycle and each signal is sampled $\boldsymbol{N}$ times, each frame obtains an RPM with $\boldsymbol{L}$ rows and $\boldsymbol{N}$ columns. A second FFT processing step is used to obtain the DRM of each frame. As an example, consider frame K+4. For ease of expression, its DRM retains only the range dimension, and the scales in Fig. 4.4 represent the range bin cell.

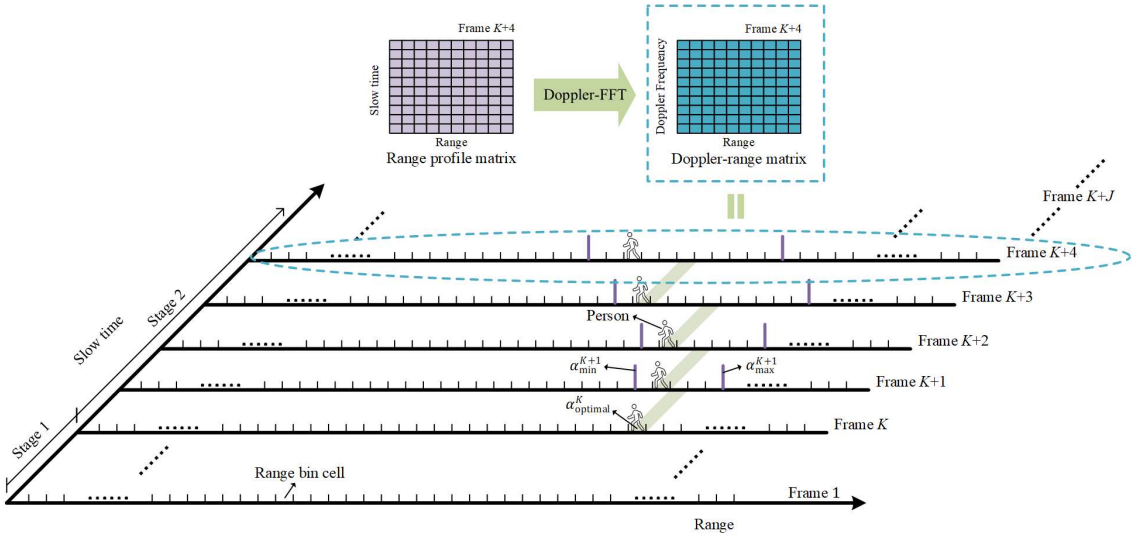

Fig. 4.4 The improved adaptive range bin selection method schematic. The Doppler-range matrix of each frame is obtained by performing Doppler-FFT processing on the range profile matrix of the respective frame. The first stage of this method obtains a reliable initial range bin cell where the target is located by accumulating data. The DRM's peak-seeking range is adaptively specified from the second stage based on the target's motion.

The method is divided into two sections: initial position confirmation and adaptive range bin selection. In the first stage, the up-chirp signals of K frames are accumulated in a short time to obtain the initial-DRM $\boldsymbol{D}_{\mathrm{i}}$. As discussed in the previous section, the data of a single frame may be disturbed by noise, and this accumulation ensures that the correct range bin cell $\alpha^{K}_{\mathrm{optimal}}$ is acquired at the beginning of the method. In the second stage, beginning with frame K+1, the peak-seeking range of the DRM for each frame is adaptively limited by the subject's instantaneous velocity, as measured by the data from the previous frames. The upper and lower limits of the peak search range and the results for frame K+j are $\alpha^{K+j}_{\mathrm{max}}$, $\alpha^{K+j}_{\mathrm{min}}$, and $\alpha^{K+j}_{\mathrm{optimal}}$, respectively ($j$ = 1, 2, 3, …….J). Their relationship can be expressed as:

$$\alpha_{\mathrm{min}}^{K+j} = \alpha_{\mathrm{optimal}}^{K+(j-1)} - \left\lceil \frac{v_{\mathrm{m}}^{K+j} T_{\mathrm{f}}}{R_{\mathrm{bin}}} \right\rceil - \beta_{\mathrm{p}}^{K+j}, \tag{4.1}$$

$$\alpha_{\max}^{K+j} = \alpha_{\text{optimal}}^{K+(j-1)} + \left\lceil \frac{v_{\text{m}}^{K+j} T_{\text{f}}}{R_{\text{bin}}} \right\rceil + \beta_{\text{p}}^{K+j}, \tag{4.2}$$

$$\beta_{\text{p}}^{K+j} = \left\lceil \eta \left(\frac{\alpha_{\max}^{K+j} - \alpha_{\min}^{K+j} + 1}{2} \right) \right\rceil, \tag{4.3}$$

where $\lceil \ldots \rceil$ rounds the element to the nearest integer greater than it, $\alpha^{K+(j-1)}_{\text{optimal}}$ is the index of the optimal range bin cell of the previous frame, R_{bin} denotes the length of each range bin cell. v^{K+j}_{m} represents the instantaneous velocity of the subject from frame $K+(j-1)$ to the frame $K+j$. The length of the protection cell, denoted by β^{K+j}_{p}, is determined by the coefficient η ($0 \leq \eta \leq 1$) and the peak-seeking range. The purpose is to avoid abrupt and significant changes in the subject's velocity. Section IV describes the selection of η in detail.

Because the velocity of the subject cannot be determined until the peak search for the frame $K+j$, v^{K+j}_{m} can only be predicted based on previous data. In a previous study [35], the plain method was used to make v^{K+j}_{m} equal to the instantaneous velocity of the subject computed in the previous frame, as determined by the Doppler shift of the DRM. However, owing to measurement errors, the instantaneous speed of a given frame can fluctuate randomly. Therefore, the moving average method is used in this study to improve it.

Assuming that v^{K+j}_{p} represents the subject's velocity in frame $K+j$. Then, v^{K+j}_{m} can be expressed as

$$v_{\text{m}}^{K+j} = \frac{\sum_{y=1}^{Y} v_{\text{p}}^{K+(j-y)}}{Y}, \tag{4.4}$$

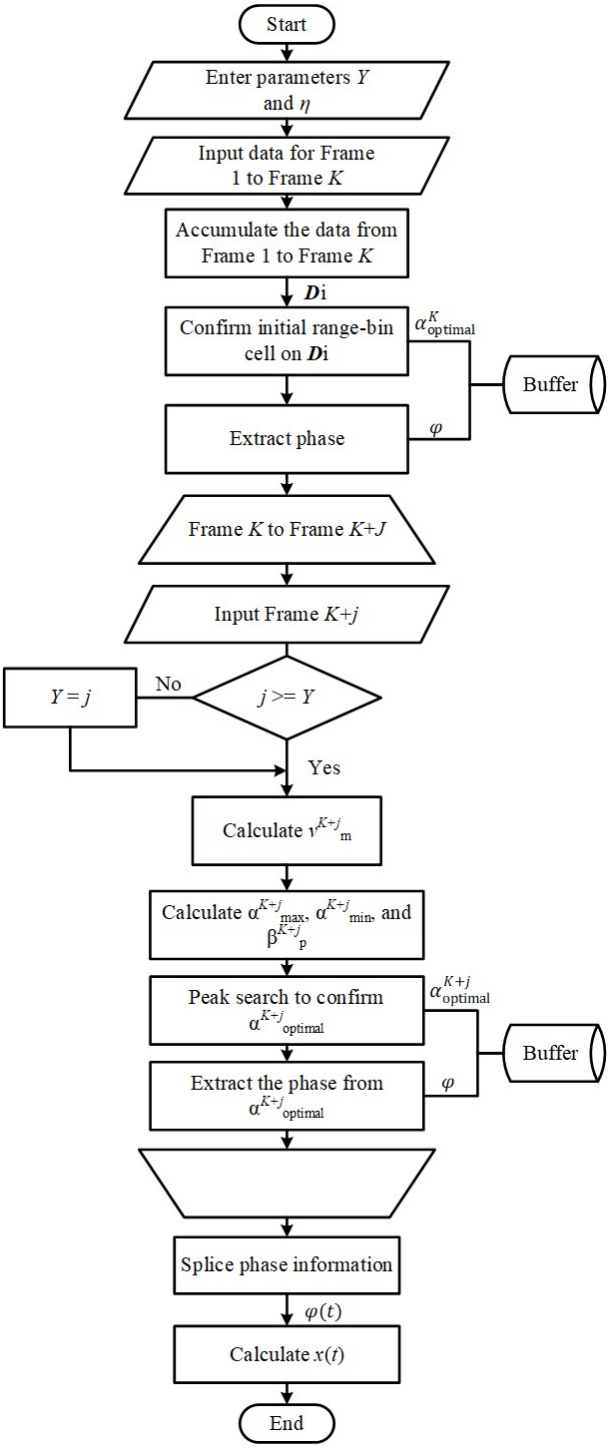

Fig. 4.5 Flowchart of the improved adaptive range bin selection method.

where Y denotes the length of the moving window. It should be noted that when Y is less than or equal to j, Y equals j.

Fig. 4.5 summarizes the flow of the improved adaptive range bin selection method. Because the subject is moving in this study, the phase part of Eq. 2.5 can be rewritten as:

$$\varphi(t) = 4\pi f_{\min} \frac{\left(R_0(t) + x(t)\right)}{\mathrm{c}} \tag{4.5}$$

where $R_0(t)$ can be obtained by calculating the optimal range bin cell and R_{bin} for each frame. Therefore, $x(t)$ containing the subject's vital signs, can be calculated using Eq. 4.5. Furthermore, by retrieving data from the buffer at regular intervals, it is possible to control the cycle length of $x(t)$ to be measured with a specific observation window, depending on the needs of the application. In the first stage, any energy above the threshold is chosen as a valid target. If more than one valid target is detected, the phase information is saved in the buffer independently.

A flow chart of the ICEEMDAN-based vital sign extraction method is shown in Fig. 4.6. ICEEMDAN decomposes $x(t)$ adaptively into several IMFs and a residual $r_n(t)$, as follows:

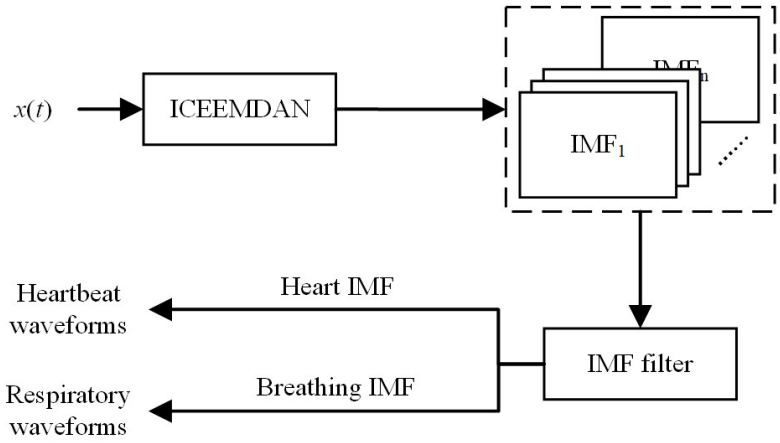

Fig. 4.6 Flowchart of the improved adaptive range bin selection method.

$$x(t) = \sum_{k=1}^{n} \mathrm{IMF}_k(t) + r_n(t), \quad k = 1, 2, 3 \ldots \ldots n. \tag{4.6}$$

Next, FFT is performed on all IMFs and $r_n(t)$ to obtain their frequency spectrum. According to the discussion in the paper [32], the IMF filter selects the IMF with a spectrum peak appearing in the range of 0.8-2.0 Hz as the heart IMF, and the corresponding breathing IMF has a peak in the range of 0.2-0.4 Hz. They are used to reconstruct the heartbeat and respiratory signals, respectively. Targets chosen as valid in the first stage of the improved adaptive selection method are deemed invalid if the ICEEMDAN results show no heart IMF or a low SNR. In practice, the first stage is repeated regularly to refresh the valid targets. If multiple targets are in the same range bin cell, ICEEMDAN can theoretically separate their vital signs, unless their frequencies are equal.

The main goal of this study is to provide an efficient tool for the millimeter-wave FMCW radar-based vital measurement system, which allows the vital signs of moving persons to be measured. Therefore, there may be better methods to extract signals such as heartbeat from $x(t)$ in other cases, which are not discussed extensively in this study, but the ICEEMDAN method was used to analyze the experimental results.

4.3 Experiment

4.3.1 Equipment and Experiment Environment

The radar module used in this study is based on the Texas Instruments Inc. IWR1443, which operates at frequencies ranging from 77 GHz to 81 GHz. Table 4.1 lists the main parameters of the radar module. The maximum effective isotropic

radiated power (EIRP) is 21 dBm, which is compliant with the FFC regulations and the Japanese Radio Law. Furthermore, it is not harmful to the human body.

This experiment included seven subjects who walked along the route shown in Fig. 4.7. Subjects walked at 0.5 m/s and 1 m/s on route A to demonstrate the efficacy of the proposed method. The other two routes walked at a speed of 0.5 m/s. Furthermore, the subjects wore electrocardiography (ECG) equipment to measure their ECG and heart rate.

Table 4.1 Radar Module Parameters.

Parameter	Value
Bandwidth	3.99 GHz
Sweep time	57 μs
Frame period	100 ms
Slope	70 MHz/μs

Table 4.2 Information About Subjects.

Subject	Height [cm]	Weight [kg]
A	179	64
B	177	75
C	173	58
D	166	55
E	169	60
F	171	62
G	172	63

Fig. 4.8 depicts the actual experimental scenario, whereas Fig. 4.7 depicts a hypothetical space designed to better understand why walking on such a route is desirable. This measurement system is not limited to living rooms; it can also be

used in wards, nursing homes, and rehabilitation rooms, and other places. Table 4.2 lists the height and weight of each experimental participant.

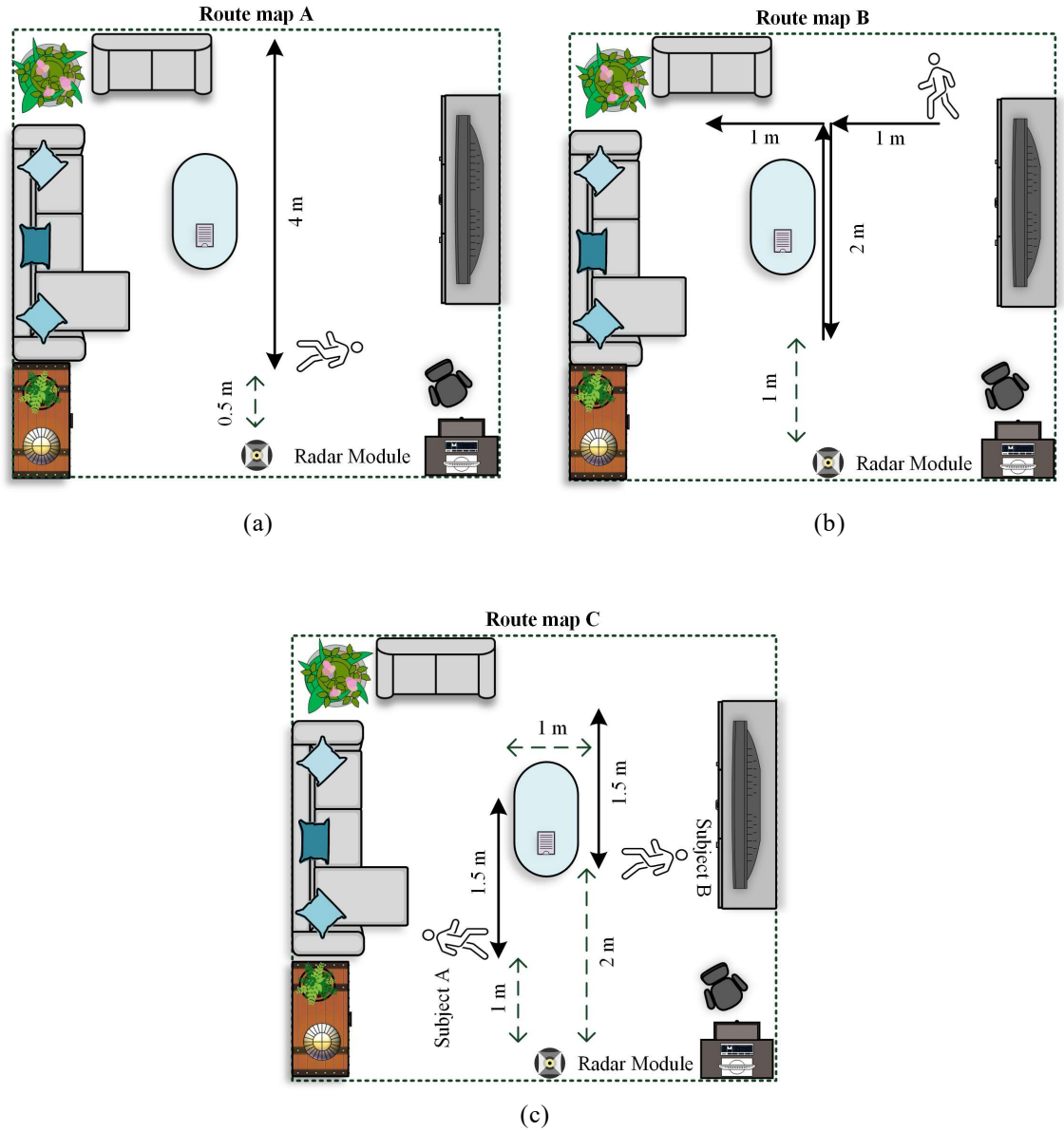

Fig. 4.7 Walking route maps of subjects. Route map A: The subject moves back and forth between 0.5 m and 4.5 m from the radar module at speeds of 0.5 m/s and 1 m/s. Route map B: The subject walks at 0.5 m/s in the direction of the arrow on the map. Route map C: At 1 m and 2 m from the radar module, both subjects walked back and forth at a speed of 0.5 m/s.

Fig. 4.8 Experimental scenario for route C.

4.3.2 Parameter Analysis

Parameter K is related to the accuracy of the initial range bin cell, but is inversely proportional to real-time performance of the measurement system. K was set to 5 in this experiment, implying that the first stage of the improved adaptive range bin selection method takes 0.5 s.

Parameter η is related to the maximum allowable speed increment per second. This experiment has a frame duration of 0.1 seconds, and when η is set to 0.1, the maximum speed increments per second allowed for initial speeds of 0.5 m/s and 1 m/s is 1.18 m/s and 2.36 m/s, respectively. Since most of the audience for this measurement system are older people and patients undergoing rehabilitation, who typically walk indoors at speeds of no more than 1 m/s, η was set to 0.1. Parameter η can be adjusted flexibly based on the application scenario and environment. Furthermore, v^{K+j}_{m} denotes the relative velocity of a subject in the radar module. Even if the subject is not directly in front of the radar, the value decreases after

converting to the relative velocity, indicating that the optimal range bin cell is not outside the range of peak-seeking.

Parameter Y was set to 5 to reduce the error that occurs when measuring the subject's instantaneous velocity through a single frame. This implies that v^{K+j}_{m} was calculated based on the velocity of the subject during the previous 0.5 s. As previously discussed, the variation in the speed of the subjects is not significant, so Y does not need to be set too high.

4.3.3 Experiment Results

A. Fixed-Route Experiments

The measurement period for routes B and C was 20 s, and the measurement period for route A was 32 s to ensure at least three back-and-forth walks. For simplicity, the two cases of route A are referred to as route A1 (mean speed of 0.5 m/s) and route A2 (mean speed of 1 m/s). Fig. 4.9 depicts the optimal range bin selection results obtained by the RPM peak-seeking method, RDM peak-seeking method, and proposed method. This figure shows the results for routes A1, A2, B, and C, from top to bottom.

As discussed in the introduction and Section III of this study, motion compensation based on either RPM or RDM peak-seeking is unstable in either case. The results show that the optimal range bin variations obtained by RPM and RDM peak-seeking are disturbed, resulting in significant random jitter.

The overall accuracy of the optimal range bin selection based on RPM peak-seeking was less than 40% at 31.7%. In particular, the worst performance was observed for route A2, where the average speed was high.

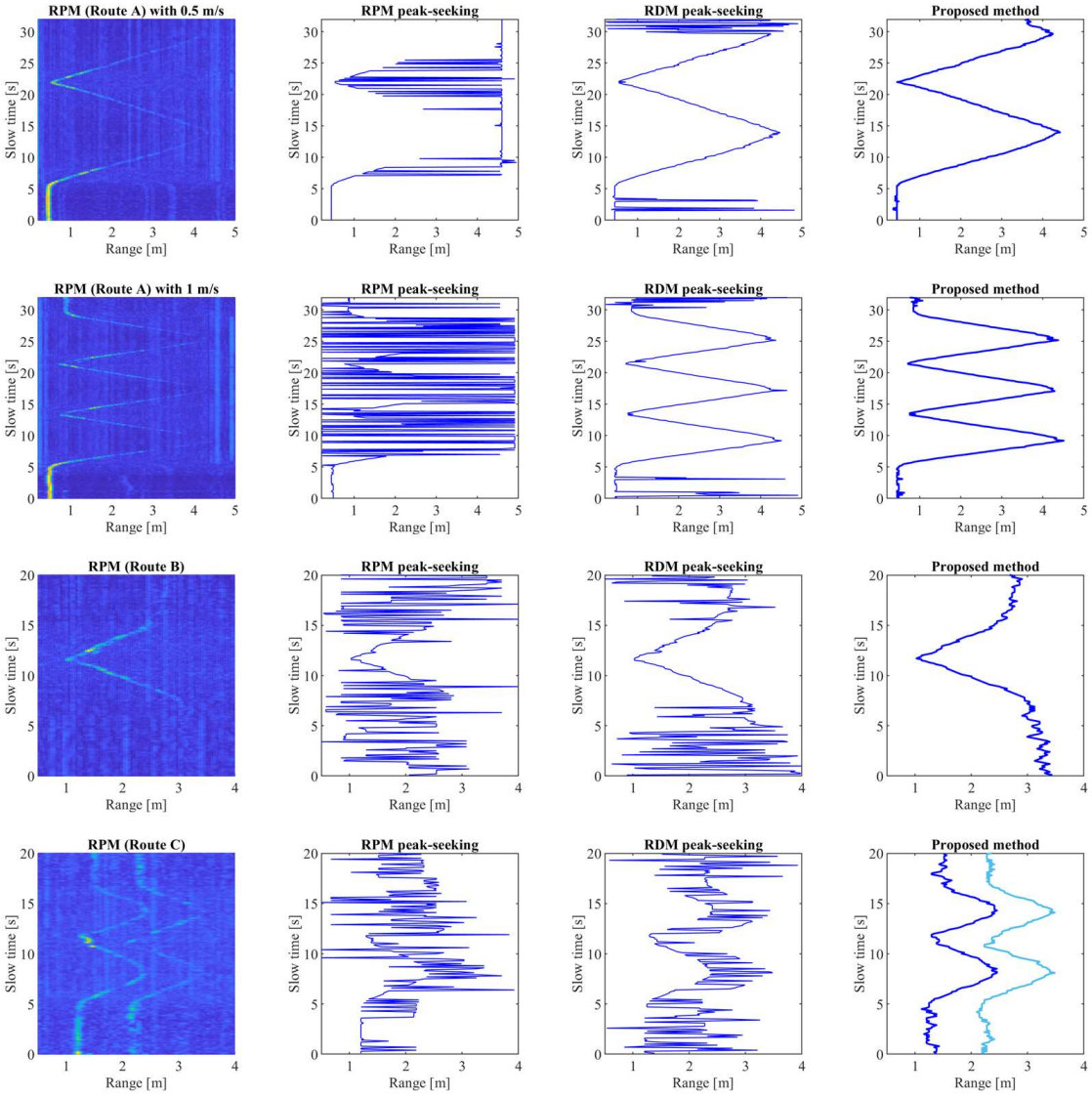

Fig. 4.9 Results of range bin cell selection. From top to bottom, the diagram shows the results for route A (with a mean speed of 0.5 m/s), route A (with a mean speed of 1 m/s), route B, and route C.

The accuracy of RDM-based peak seeking was 82.8% and 88.3% in the case of routes A1 and A2, respectively. However, there is still a significant jitter across the distance. The results for route B demonstrate the limitations of the method when the subjects walk horizontally. Furthermore, in the case of route C, the range bin selections of the two subjects interfered with each other.

The improved adaptive range bin selection method proposed in this study can solve the problems associated with comparison methods. In the case of routes A1 and A2, the accuracy of the range bin cells obtained using the proposed method was 97.8% and 94.7%, respectively. Route B shows that even when the subject faces the radar module sideways, the range bin cell can be accurately identified. Most importantly, the first stage of the proposed method can identify multiple trackable targets, allowing the vital signals of multiple moving targets to be simultaneously measured.

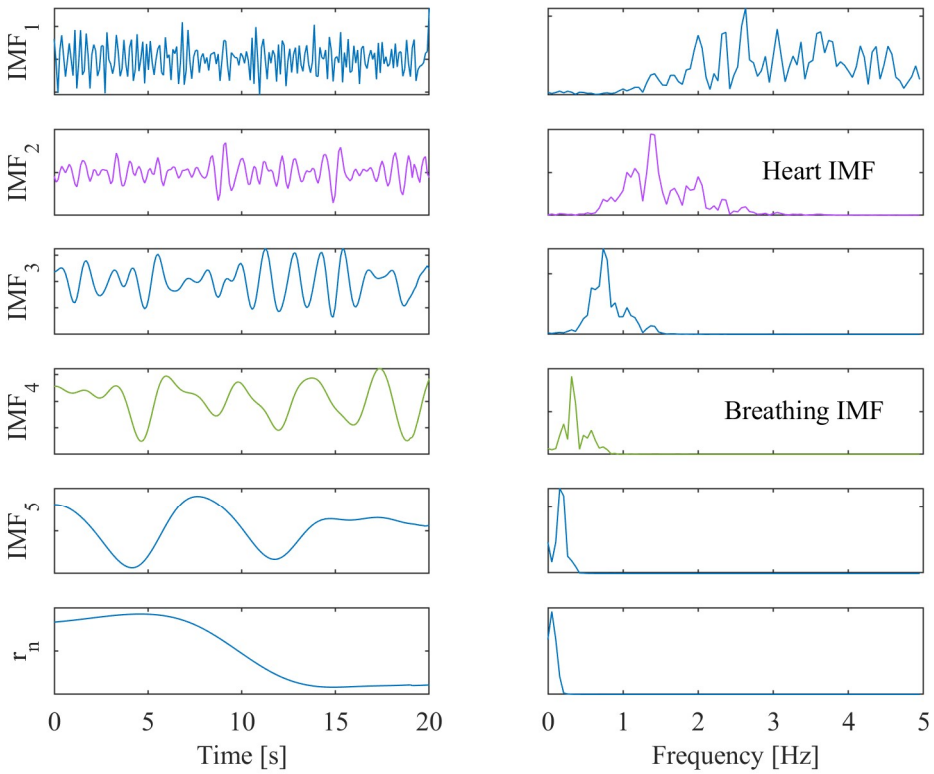

Fig. 4.10 Results of ICEEMDAN decomposition. The left and right sides are the time domain and frequency domain, respectively. The x(t) signal is obtained by the proposed method and is in the case of route B.

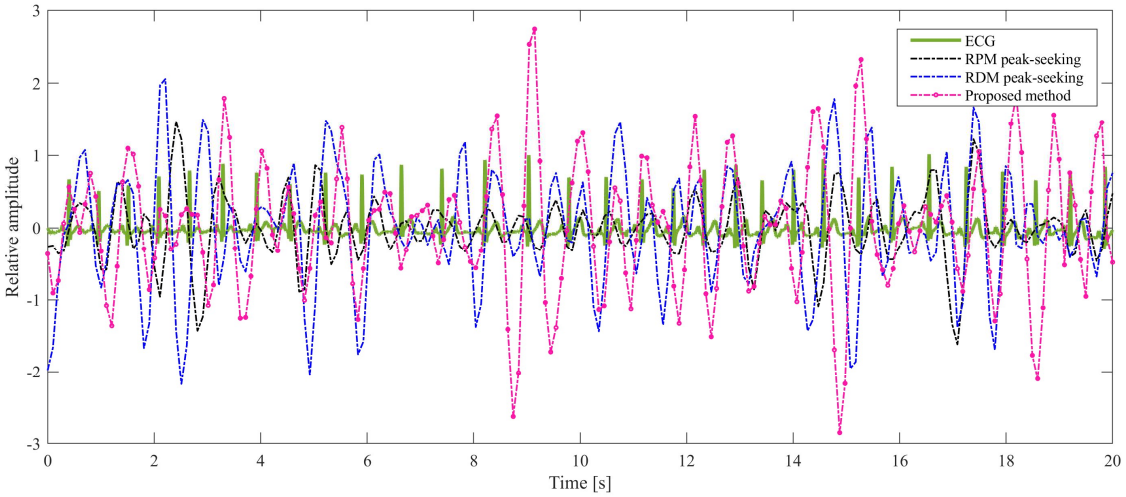

Fig. 4.11 The reconstructed heartbeat waveforms versus ECG waveform in the time domain.

Because route B is more complex than the other routes, the results of $x(t)$ signal decomposition by ICEEMDAN are shown in Fig. 4.10 to demonstrate the effectiveness of the proposed method. This observation window lasted 20 s, and the spectrum analysis revealed that IMF_2 and IMF_4 were the heart IMF and breathing IMF, respectively. Furthermore, this heart IMF has a high SNR with a significant peak to aid in the measurement of the heart rate and will reconstruct the heartbeat signal. The respiratory signal is simple to measure owing to its high amplitude and low frequency. Therefore, the measurement of the heartbeat signal is the focus of this study.

As shown in Fig. 4.11, the heartbeat signals measured by the two comparison methods and the proposed method are compared to the ECG signal. The heartbeat waveforms reconstructed by the comparison methods correlated poorly with the ECG signals. The RR interval of the heartbeat waveform acquired using the proposed method, on the other hand, remained highly consistent with that of the ECG signal even when the subject walked laterally for period of 0-6 s and 15-20 s.

At the same time, data from this observation window revealed that the heartbeat waveform fluctuated slightly when the subject turned, but the overall heart rate error was only 2.01 bpm compared to the ECG signal.

Table 4.3 displays the results of the heart rate measurements for each route condition, with the measured values and absolute errors in beats per minute (bpm). Subjects A, C, E, and G walked in the 2-3.5 m range in the route C experiment, while subjects B, D, and F walked in the 1-2.5 m range. The results showed that the accuracy of the RPM peak-seeking method in measuring the heart rate was poor and almost lost its referential value. The RDM peak-seeking method improves the accuracy of the heart rate measurement over the former method, but it is precarious and unreliable. In the case of routes A1, A2, B, and C, the mean absolute errors of heart rate measured by the proposed method were 3.11 bpm, 3.10 bpm, 3.47 bpm, and 5.24 bpm, with an overall root mean squared error (RMSE) of 4.09 bpm. In paper [69], the subjects moved very slowly and had a heart rate estimation accuracy of 90%. As in the previous study, the subjects in [59] performed only backward and forward movements at a slow speed with a measurement error range of 0-8 bpm. The authors of paper [60] used multiple radars to measure the heart rate of a moving target with an accuracy of about 86%. The mean heart rate measurement accuracy of the proposed method was 95.88%. The results for routes A1 and A2 show that even accelerating the walking speed to 1 m/s does not reduce the accuracy of the measurement results. Furthermore, the experimental results for routes B and C fully demonstrate the validity and application potential of the proposed method.

Table 4.3 Heart Rate Measurement Results.
(Measured Value: [BPM], Absolute Error: [BPM])

Route	Subject	ECG	RPM peak-seeking		RDM peak-seeking		Proposed method		
			Measured value	Absolute error	Measured value	Absolute error	Measured value	Absolute error	Accuracy
A1	A	92.76	73.14	19.62	101.28	8.52	88.14	4.62	95.02%
	B	94.38	61.86	32.52	67.50	26.88	90.00	4.38	95.36%
	C	87.84	61.96	25.88	67.52	20.32	90.02	2.18	97.52%
	D	115.14	65.64	49.50	82.50	32.64	112.50	2.64	97.71%
	E	82.68	99.36	16.68	76.86	5.82	84.36	1.68	97.97%
	F	76.86	84.36	7.50	72.13	4.73	73.14	3.72	95.16%
	G	76.20	80.64	4.44	73.14	3.06	78.78	2.58	96.61%
A2	A	99.00	80.64	18.36	86.28	12.72	101.28	2.28	97.70%
	B	98.22	90.00	8.22	101.29	3.07	100.23	2.01	97.95%
	C	99.96	69.36	30.60	82.51	17.45	97.50	2.46	97.54%
	D	105.96	86.27	19.69	88.17	17.79	103.14	2.82	97.34%
	E	80.14	69.50	10.64	73.41	6.73	76.92	3.22	95.98%
	F	93.60	78.78	14.82	101.28	7.68	88.68	4.92	94.74%
	G	84.00	73.17	10.83	93.78	9.78	88.01	4.01	95.23%
B	A	100.98	75.00	25.98	93.75	7.23	95.50	5.48	94.57%
	B	93.12	101.25	8.13	84.38	8.74	99.38	6.26	93.28%
	C	92.28	75.00	17.28	78.75	13.53	88.13	4.15	95.50%
	D	115.38	65.63	49.75	108.76	6.62	116.25	0.87	99.25%
	E	88.26	84.36	3.90	99.36	11.10	86.25	2.01	97.72%
	F	79.56	67.50	12.06	66.00	13.56	84.36	4.80	93.97%
	G	85.08	90.00	4.92	82.50	2.58	84.36	0.72	99.15%
C	A	91.38	80.64	10.74	84.36	7.02	95.64	4.26	95.34%
	B	97.44	76.86	20.58	105.00	7.56	93.78	3.66	96.24%
	C	91.74	80.63	11.11	82.50	9.24	99.36	7.62	91.69%
	D	109.80	75.00	34.80	93.78	16.02	103.14	6.66	93.93%
	E	91.20	71.28	19.92	67.50	23.70	86.28	4.92	94.61%
	F	75.90	105.00	29.10	86.28	10.38	80.64	4.74	93.75%
	G	77.94	67.50	10.44	95.64	17.70	73.14	4.80	93.84%

B. Random Walk Experiments

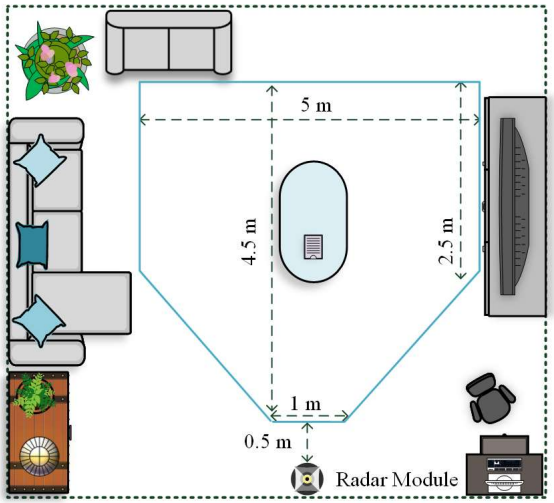

Fig. 4.12 The environment for the random walk experiment is depicted in this diagram.

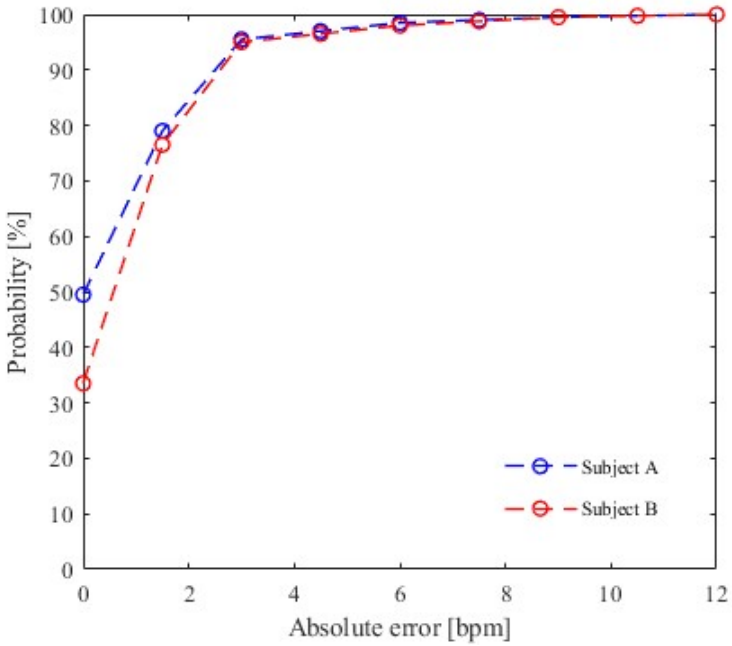

Fig. 4.13 The results of a random walk experiment's heart rate measurements. The absolute errors between the measured values and the ECG data are presented in the form of cumulative distribution functions.

Two subjects walked randomly and simultaneously in the area depicted in Fig. 4.12 at speeds ranging from 0 to 1 m/s for 10 minutes. The area is approximately 18.5 square meters, comparable to a typical bedroom or living room.

The 10-minute streaming data was analyzed using a 20-second observation window and a 1-second sliding step because route C of the fixed-route tests had a measurement period of 20 seconds. There were 581 observation windows data for each subject for the measurement time. Fig. 4.13 shows the absolute error distributions of the heart rates obtained by each window measurement compared to the corresponding ECG data. The findings of this experiment demonstrate that the vast majority of absolute errors fall between the 0 to 5 bpm range, which is consistent with the results of previous fixed-route tests. Due to the right side of the human body facing the radar for a long time or a large body shake when turning, a small number of observation windows showed an absolute error of more than 5 bpm.

Overall, the proposed method's measurement error is within acceptable limits. This experiment proved the stability of the method.

4.4 Summary of Chapter 4

In conclusion, this study proposes a novel FMCW radar-based vital sign monitoring method for moving persons. The proposed improved adaptive range bin selection method efficiently selects the optimal range bin cells to obtain high-quality phase-change information, and the reconstructed heartbeat signal using the ICEEMDAN method is highly consistent with the ECG signal. The overall RMSE for heart rate estimation was 4.09 bpm, with an accuracy of 95.88%. The experimental results showed that the accuracy of the heart rate measurement remained high regardless of whether the subjects walked at 1 m/s or with the left side of their body facing the radar. Furthermore, random walk experiments have

proved its good stability. Therefore, this measurement method has application potential. Measuring vital signs from the right side of the human body is challenging, and there is a classification problem if multiple targets are in the same range bin cell for an extended period. Therefore, we plan to use multiple radars to improve this measurement system in future studies.

Chapter 5 A Novel Remote-tracking Heart Rate Measurement Method Based on Stepping Motor and Radar

5.1 Research Background for Chapter 5

Most radar-based vital signs estimation studies call for subjects to stay still, including standing, sitting in a chair, or resting in bed [26], [44], [50], [61]-[62], [65]-[67], [71]-[80]. This limits the application of radar-based heart rate measurement methods. For this reason, the authors of [59]-[60] and [69] attempted to use IR-UWB radar and FMCW radar, respectively, to estimate the heart rate of a moving person. However, the subjects in the research mentioned above could only move slowly. To address this issue, we proposed an improved adaptive range bin selection (IARBS) method for moving subjects' heart rate measurements based on the FMCW radar [35]. The subjects maintained a high measurement accuracy when they walked at an average speed of 1 m/s. However, because of the radar characteristics, the measurement range may be constrained. It is challenging to cover the entire room, even with beamforming techniques. When the angle is too large, the beam widens, the antenna gain drops, and the performance suffers. If there are several radars in the room, they can interfere with each other and increase background noise. Moreover, these methods increase the cost of the measurement system, which is not conducive to the popularity of the application.

The authors of [81] proposed a novel approach for mounting radar on a mobile

robot. However, it may not be appropriate for older adults living alone, in senior homes, or in medically isolated observations. There is a safety risk because the senior may trip over the wires because the robot must be attached to the power source. It is difficult to continuously monitor if a charging method is employed. In [82], a method for adaptively changing radar orientation by acquiring the subject's position through a camera was proposed. However, image processing using cameras is sensitive to ambient lighting and involves personal privacy issues. Additionally, the subjects' heart rate measurements while moving were not evaluated in the abovementioned study.

In [36], we proposed and discussed the possibility of using a stepping motor to change the radar orientation but only verified it using a simple simulation. This study improves the method of [36] and proposes a novel, radar-based, adaptive remote-tracking heart rate measuring technique to address the abovementioned issues. In this study, we build an actual measurement device. The radar module is fixed to a rotatable circular plate. The radar measures the heart rate while measuring the position of the monitored person, which is then processed and transmitted to a stepping motor to drive the rotation of the radar module. A stepping motor is used in this study because for the following reasons. Because the stepping motor has no brushes, it is more reliable. Additionally, it does not accumulate the error of one step to the next step, and thus has better position accuracy. Furthermore, the motor is simple and inexpensive, because its response is based only on a digital input pulse.

The monitored person can always be within the ideal measurement range owing to the adaptively adjusted radar orientation. Next, after sampling the raw radar data, the range bins where the subject is located are selected along the time dimension using the IARBS method, and their phase information is extracted. The displacement information of the human skin surface, brought on by the body's torso, heartbeat, and breathing, can be obtained using the phase change information. We suggested using the improved complete ensemble empirical mode decomposition with adaptive noise (ICEEMDAN) approach to extract the heartbeat signal and determine its heart rate [32]. In this study, we continue to use this technique to analyze the experimental data and evaluate the accuracy of the proposed measurement system.

In this study, we build an actual measurement device, using a stepping motor to change the radar direction to adjust the ideal range for measuring the heart rate. The proposed measurement system tracks a moving subject using radar signal processing. Even though this subject walks at an average speed of 1 m/s and the horizontal angle to the radar module varies widely. This significantly increases the application potential of radar-based remote heart rate measurements. To the best of our knowledge, this is the first study that challenges this field.

5.2 Measurement Method Based on Stepping Motor and Radar

As mentioned in the introduction, the inability to alter the radar module's orientation is a drawback of conventional radar-based heart rate measurement

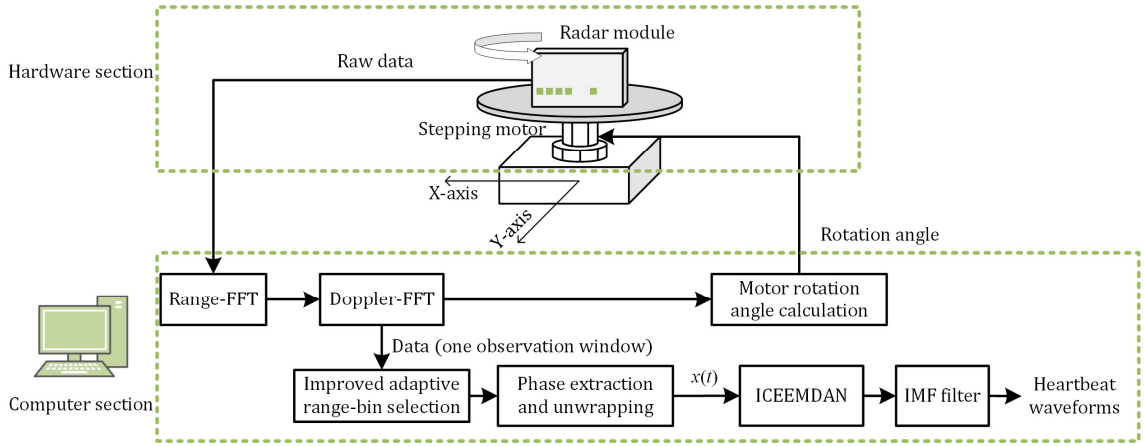

Fig. 5.1 The flow chart of the proposed processing.

methods. Therefore, it is impossible to estimate the heart rate once the subject has departed from a specific range. A heart rate measurement method with a motor combined with a millimeter-wave FMCW radar is proposed in this study as a solution to the abovementioned issue and to increase the applicability of the measurement method. The proposed approach utilizes radar signal processing to calculate the target's motion information, which is then sent to a stepping motor to adjust the orientation of the radar module. In this manner, real-time adaptive tracking heart rate monitoring is accomplished.

The signal processing flowchart of the proposed method is shown in Fig. 5.1, where the computer section is divided into sections for heart rate monitoring and stepping motor rotation control.

5.2.1 Stepping Motor Rotation Control

The ADC samples the IF signal, which is then sent to a computer in frames for signal processing. In radar-based heart rate measurement research, 0.05 s is a typical choice for the frame period [50], [77]. A frame period T_f of 0.05 s is comparable to sampling the target's heartbeat signal at a sampling frequency of 20

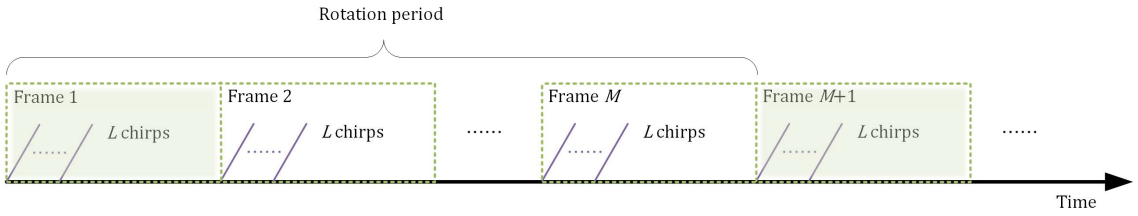

Fig. 5.2 Diagram of frame period in relation to rotation period.

Hz because the average human heart rate is less than 2 Hz, which satisfies the sampling theorem. However, excessive shortening of the frame period leads to more frequent data transmission from the radar module to the computer, which may increase the possibility of data loss. Therefore, in this study, the frame length was fixed at 0.05 s.

As shown in Fig. 5.2, this study emits L chirp signals in a single frame cycle to execute multidimensional FFT calculations, in contrast to other studies that emit only one chirp signal in each frame. A raw data matrix with L rows and N columns is generated for each frame after each chirp signal is sampled N times. A range-FFT is first performed to the fast time dimension of each frame's raw data to generate the range profile matrix (RPM). Next, a Doppler-FFT is applied to the slow time dimension of the RPM to create a range-Doppler matrix (RDM).

A flowchart of the calculation of the rotation angle of the stepping motor is shown in Fig. 5.3. Assuming a frame period of 0.05 s, the maximum distance moved in a single frame is only 10 cm, even if the subject walks at a higher speed of 2 m/s. Therefore, the distance moved by the subject in a single frame cycle is

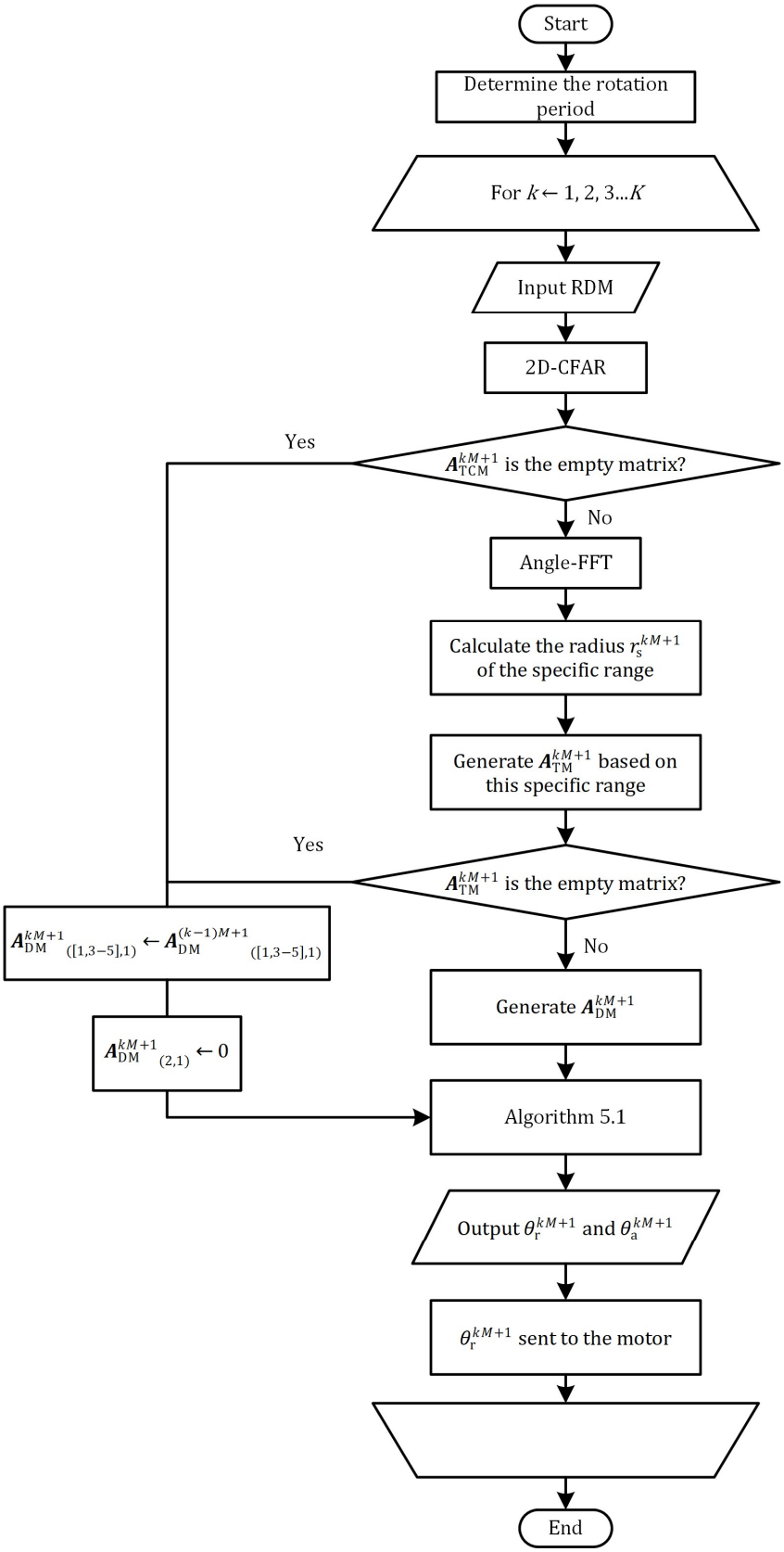

Fig. 5.3 Flowchart of calculating the rotation angle.

relatively small, and considering the high real-time requirements of this measurement method, it is not necessary to rotate the motor frame by frame. Instead, it determines whether a stepping motor is required to correct the radar alignment by detecting the subject's position every M frames (one rotation period T_r). The motor rotation angle calculation module receives the RDM of the kM+1 th frame (k=1, 2, 3…K) as input, as depicted in Fig. 5.2.

The clutter brought on by other objects and the noise produced by the radar receiver due to temperature, weather, and other factors influence the quality of the radar signal. Therefore, the range bin cells containing the target candidates and their Doppler shifts are identified by performing 2D-CA-CFAR processing for each RDM. 2D-CA-CFAR, 2D-OS-CFAR, and other CFAR algorithms are increasingly being utilized [83]-[84]. 2D-OS-CFAR performs better in scenarios with numerous strong interference targets, but the computational effort is substantial [85]. 2D-CA-CFAR is computationally simple and exhibits good performance in pure-noise situations. The 2D-CA-CFAR algorithm is chosen because the environmental background of this study is not complex, the subject is only one person, and the requirement for real-time performance is high. In addition, because the millimeter wave has a high sweep bandwidth, the range bin cell corresponds to a tiny distance interval; therefore, the protection and reference cells of the CA- CFAR algorithm do not affect the measurable range of the radar. CFAR-related algorithms are not the main topic of this work, and the correlations between false alarm probability, judgment threshold, and detection probability are discussed in more detail in [85].

Objects in the RDM that exceed the threshold after 2D-CA-CFAR processing are referred to as target candidates. The instantaneous velocities of the target candidates in the *kM*+1 th frame are calculated using the Doppler shift. All target candidates, including the subject, remain immobile when the velocities are zero. As a result, the rotation angle $\theta_{\mathrm{r}}^{kM+1}$ is zero, and the motor does not need to be adjusted to change the orientation of the radar module.

A target candidate matrix (TCM) $\boldsymbol{A}_{\mathrm{TCM}}^{kM+1}$ is created if u $(u = 1, 2, 3 \ldots U)$ moving targets are detected in the *kM*+1 th frame, with the number of columns representing the number of candidates. The first row is the distance R_{kM+1} from the radar, and the second row represents the instantaneous velocity information v_{kM+1}, as shown in eq. 5.1.

$$\boldsymbol{A}_{\mathrm{TCM}}^{kM+} = \begin{bmatrix} R_1^{kM+1} & R_2^{kM+1} & R_3^{kM+1} & \cdots & R_U^{kM+1} \\ v_1^{kM+1} & v_2^{kM+1} & v_3^{kM+1} & \cdots & v_U^{kM+1} \end{bmatrix} \tag{5.1}$$

The instantaneous angle of the object can be calculated by the following:

$$\theta = \sin^{-1}\frac{\lambda\Delta\omega}{2\pi \mathrm{d}}, \tag{5.2}$$

where λ is the wavelength, $\Delta\omega$ is the phase difference obtained after angle-FFT processing in the antenna direction based on the data obtained by RDM, and d is the pitch of the receiver antennas. The geometric significance of θ is the angle of arrival (AoA) of the object with the radar module in the horizontal plane.

It is assumed that the radar coordinate point is the origin of the coordinate system, and the initial orientation of the radar module is the positive direction of

the y-axis, from which the absolute coordinate system is established. The initial position and velocity of the target are $(0, R_1^0)$ and zero, respectively. Additionally, angle $\theta_{\mathrm{a}}^{kM+1}$ is formed by the initial and current radar orientations and is updated in real time. The orientation of the radar changes when tracking the target. Therefore, utilizing $\theta_{\mathrm{a}}^{kM+1}$ to map the target's current coordinates into the initial absolute coordinates is necessary. In this way, the TCM can be expanded to five rows, as shown in eq .5.3, with the third row representing the angle information and the fourth and fifth rows representing the x-axis and y-axis absolute coordinates, respectively. The x-axis and y-axis directions are defined in Fig. 5.1.

$$\begin{cases} \boldsymbol{A}_{\mathrm{TCM}}^{0} = \begin{bmatrix} R_1^0 \\ 0 \\ 0 \\ 0 \\ R_1^0 \end{bmatrix} \\ \boldsymbol{A}_{\mathrm{TCM}}^{kM+} = \begin{bmatrix} R_1^{kM+1} & \cdots & R_U^{kM+} \\ v_1^{kM+1} & \cdots & v_U^{kM+1} \\ \theta_1^{kM+1} & \cdots & \theta_U^{kM+1} \\ R_1^{kM+1}\sin(\theta_1^{kM+1} + \theta_{\mathrm{a}}^{(k-1)M+1}) & \cdots & R_U^{kM+1}\sin(\theta_U^{kM+1} + \theta_{\mathrm{a}}^{(k-1)M+1}) \\ R_1^{kM+1}\cos(\theta_1^{kM+1} + \theta_{\mathrm{a}}^{(k-1)M+1}) & \cdots & R_U^{kM+1}\cos(\theta_U^{kM+1} + \theta_{\mathrm{a}}^{(k-1)M+1}) \end{bmatrix} \end{cases} \tag{5.3}$$

Although the subject may generate multiple target candidates, clutter may also exist in the TCM. Therefore, a range of values is specified based on the prior motion information of the target, which is very similar to the improved range bin selection method we proposed previously [35]. The distinction is that the specified range of values in this study is expanded from a one-dimensional line to a two-dimensional surface. All target candidates within a specific range are regarded as

being produced by the subject and creating a new target matrix $\boldsymbol{A}_{\mathrm{TM}}^{kM+1}$. Then, averaging along each row of the $\boldsymbol{A}_{\mathrm{TM}}^{kM+1}$ yields a rotation decision matrix $\boldsymbol{A}_{\mathrm{DM}}^{kM+1}$ for that frame with one column and five rows, as shown in Eq. 5.4.

$$\boldsymbol{A}_{\mathrm{DM}}^{kM+1}=\begin{bmatrix}\bar{R}^{kM+}\\ \bar{v}^{kM+1}\\ \bar{\theta}^{kM+1}\\ \bar{R}^{kM+1}\sin(\bar{\theta}^{kM+1}+\theta_{\mathrm{a}}^{(k-1)M+1})\\ \bar{R}^{kM+1}\cos\left(\bar{\theta}^{kM+1}+\theta_{\mathrm{a}}^{(k-1)M+1}\right)\end{bmatrix}, \tag{5.4}$$

where $\bar{\theta}^{kM+1}$ is the angle between the subject and the positive direction of the radar module. To obtain the $\boldsymbol{A}_{\mathrm{TM}}^{kM+1}$, the specific range of values for the current TCM is defined as

1) The center coordinates of the circle are set to the values $\boldsymbol{A}_{\mathrm{DM}}^{(k-1)M+1}{}_{(4,1)}$ and $\boldsymbol{A}_{\mathrm{DM}}^{(k-1)M+1}{}_{(5,1)}$ of the preceding rotation period.

2) The human walking process can be approximated as a uniform motion, so the radius r_{s}^{kM+1} of the specific range of values can be calculated using Eq. 5.5 and Eq. 5.6. The protection unit β_{s} is also introduced to increase fault tolerance, considering that there is occasionally acceleration from the stationary state to the uniform state.

$$r_{\mathrm{s}}^{kM+1}=\left(\left|\bar{v}^{(k-1)M+1}\right|T_{\mathrm{r}}\right)+\beta_{\mathrm{s}}\,, \tag{5.5}$$

$$\beta_{\mathrm{s}}=\frac{1}{2}a_{\mathrm{s}}{T_{\mathrm{r}}}^{2}\,, \tag{5.6}$$

where a_{s} is the subject's acceleration, and the value can be adjusted based on the conditions of the environment and the application background.

3) Assume that matrix TCM has u $(u = 1, 2, 3 \ldots U)$ target candidates. Then, the target candidates satisfying Eq. 5.7 are retained to form $\boldsymbol{A}_{\mathrm{TM}}^{kM+1}$. This is compared to the matrix $\boldsymbol{A}_{\mathrm{TCM}}^{0}$ when k is zero.

$$r_{\mathrm{s}}^{kM+1} \geq \sqrt{\left(\boldsymbol{A}_{\mathrm{TCM}}^{kM+1}{}_{(4,u)} - \boldsymbol{A}_{\mathrm{DM}}^{(k-1)M+1}{}_{(4,1)}\right)^2 + \left(\boldsymbol{A}_{\mathrm{TCM}}^{kM+1}{}_{(5,u)} - \boldsymbol{A}_{\mathrm{DM}}^{(k-1)M+1}{}_{(5,1)}\right)^2} \quad (5.7)$$

When $\boldsymbol{A}_{\mathrm{TCM}}^{kM+1}$ or $\boldsymbol{A}_{\mathrm{TM}}^{kM+1}$ is empty, $\boldsymbol{A}_{\mathrm{DM}}^{kM+1}$ inherits the matrix $\boldsymbol{A}_{\mathrm{DM}}^{(k-1)M+1}$ except for the second element (instantaneous velocity information), because there is no moving target in a particular range. Hence, the value of the second element is zero.

By contrast, $\boldsymbol{A}_{\mathrm{TM}}^{kM+1}$ is averaged along the row direction to produce $\boldsymbol{A}_{\mathrm{DM}}^{kM+1}$ if it is not empty. $\boldsymbol{A}_{\mathrm{DM}}^{kM+1}{}_{(3,1)}$ is the arrival angle of the subject, and its angle with the positive direction of the y-axis in absolute coordinates is $\boldsymbol{A}_{\mathrm{DM}}^{kM+1}{}_{(3,1)} + \theta_{\mathrm{a}}^{(k-1)M+1}$.

The rotation angle threshold value θ_{s} is set to filter angle $\boldsymbol{A}_{\mathrm{DM}}^{kM+1}{}_{(3,1)}$. If the subject's movement results in only a slight angle shift, it is not essential to rotate the motor to change the radar's orientation. Thus, the proposed method can be used to ensure that the subject is always within the measured range and not precisely on the midline of the radar azimuth. Frequent, brief back-and-forth rotations may reduce the accuracy of heart rate measurements. The algorithm 5.1 calculates the angle $\theta_{\mathrm{r}}^{kM+1}$ the motor needs to rotate at each period and updates the angle $\theta_{\mathrm{a}}^{kM+1}$. Finally, the stepping motor operates according to angle $\theta_{\mathrm{r}}^{kM+1}$.

In the multi-subject scenario, regardless of whether the other subjects are

stationary, their information will not be included in the $\boldsymbol{A}_{\mathrm{TM}}$ since they are not within a specific range. Usually, the specific range is very small. For example, if the rotation period is 0.2 s and the average speed is 1 m/s, the radius of the search range is only about 0.2 m. The probability of other subjects entering this range is very low. An object may generate more than one target candidate point. Even if the other subjects are close to the tracked subject, only a few points from other subjects exist within the specific range. Then, the average processing in the calculation of $\boldsymbol{A}_{\mathrm{DM}}$ will remove their effect. Therefore, the proposed tracking method can also correctly lock the target without interference from other subjects in a multi-subject scenario.

Algorithm 5.1 Rotation Angle Calculation.

θ_{step} is the step angle of the stepping motor (a constant parameter);

$\lceil \ldots \rceil$ rounds the element to the next larger integer ;

$\lfloor \ldots \rfloor$ rounds the element down to the next lower integer ;

If $\boldsymbol{A}_{\mathrm{DM}}^{kM+1}{}_{(3,1)} < \theta_{\mathrm{s}}$ **then**

$\theta_{\mathrm{r}}^{kM+1} \leftarrow 0$;

$\theta_{\mathrm{a}}^{kM+1} \leftarrow \theta_{\mathrm{a}}^{(k-1)M+1}$;

Else

If $\boldsymbol{A}_{\mathrm{DM}}^{kM+1}{}_{(3,1)} > 0$ **then**

$$\theta_{\mathrm{r}}^{kM+1} \leftarrow \left\lceil \frac{\boldsymbol{A}_{\mathrm{DM}}^{kM+1}{}_{(3,1)}}{\theta_{\mathrm{step}}} \right\rceil \theta_{\mathrm{step}} ;$$

Else

$$\theta_{\mathrm{r}}^{kM+1} \leftarrow \left\lfloor \frac{\boldsymbol{A}_{\mathrm{DM}}^{kM+1}{}_{(3,1)}}{\theta_{\mathrm{step}}} \right\rfloor \theta_{\mathrm{step}} ;$$

$\theta_{\mathrm{a}}^{kM+1} \leftarrow \theta_{\mathrm{a}}^{(k-1)M+1} + \theta_{\mathrm{r}}^{kM+1}$;

Return: $\theta_{\mathrm{r}}^{kM+1}, \theta_{\mathrm{a}}^{kM+1}$;

5.2.2 Heart Rate Monitoring

The approach mentioned above ensures that the subject is constantly within the measurement range. By examining the RPM, the phase change information $\varphi(t)$ can be obtained from the range bin cell where the subject is located. The thoracic skin displacement $x(t)$ is determined by using the phase change information, and this displacement is then utilized to extract the heartbeat signal and determine the heart rate.

As discussed in the background of Chapter 5, subjects had to remain still (sitting, standing, or lying down) for the measurement in most earlier studies using radar-based heart rate monitoring. In addition, the subjects were typically close to the radar. In this situation, techniques such as RPM peak detection can quickly identify the range bin cell in which the subject is located. Furthermore, once the range bin cell is located, no further modifications are required for the duration of the measuring cycle.

In contrast, the subjects in this study were accompanied by two states, motion and stationary, implying that the target range bin cells were constantly changing. Additionally, because RPM peak-seeking or RDM peak-seeking is susceptible to noise, it is challenging to locate the target range bin cells using these methods alone. Therefore, we suggested the improved adaptive range bin selection approach [35], which is also utilized in this study, to collect high-quality phase information precisely and swiftly.

The initial location confirmation and adaptive range bin selection are two parts of the IARBS method. The initial DRM $\boldsymbol{D}_{\mathrm{i}}$ is obtained in the first step by

immediately accumulating the up-chirp signals of H frames, which ensures that the appropriate range bin cell $\alpha^{H}_{\text{optimal}}$ is acquired at the beginning.

In the second stage, starting with frame H+1, the instantaneous velocity of the subject, as determined by the data from the preceding frames, adaptively limits the peak-seeking range of the DRM for each frame. The following are the justifications for not directly using the data from matrix $\boldsymbol{A}_{\text{DM}}$. High real-time performance is needed for motor rotation, and the rotation angle calculation function quickly calculates the subject's approximate position per M frames. However, heart rate measurement must precisely obtain the optimal range bin cell.

a^{H+j}_{max}, $\alpha^{H+j}_{\text{min}}$, and $\alpha^{H+j}_{\text{optimal}}$ are the upper and lower bounds of the peak-seeking range and the outcomes for frame $H+j$ (j = 1, 2, 3,…J), respectively. Their relationship is defined by Eq. 5.8, Eq. 5.9, and Eq. 5.10.

$$\alpha_{\text{min}}^{H+j} = \alpha_{\text{optimal}}^{H+(j-1)} - \left\lceil \frac{v_{\text{m}}^{H+j} T_{\text{f}}}{R_{\text{bin}}} \right\rceil - \beta_{\text{p}}^{H+j}, \tag{5.8}$$

$$\alpha_{\text{max}}^{H+j} = \alpha_{\text{optimal}}^{H+(j-1)} + \left\lceil \frac{v_{\text{m}}^{H+j} T_{\text{f}}}{R_{\text{bin}}} \right\rceil + \beta_{\text{p}}^{H+j}, \tag{5.9}$$

$$\beta_{\text{p}}^{H+j} = \left\lceil \eta \left(\frac{\alpha_{\text{max}}^{H+j} - \alpha_{\text{min}}^{H+j} + 1}{2} \right) \right\rceil, \tag{5.10}$$

where $\lceil ... \rceil$ rounds the element to the next larger integer, and R_{bin} represents the length of each range bin cell. The instantaneous velocity of the subject from frame $H+(j\text{-}1)$ to frame $H+j$ is represented by v^{H+j}_{m}. The coefficient η ($0 \le \eta \le 1$) and the peak-seeking range determine the protection cell length, represented as β^{H+j}_{p}. H and η are typically set at 0.5 and 0.1, respectively, according to [35].

After choosing the optimal range bin cell, L phase information (L chirp signals per frame) can be collected for each frame and averaged to enhance the phase quality. This implies that each frame extracts a phase value in the optimal range bin to which it corresponds. Then, the phase information of each frame in an observation window is stitched together in order of time, which gives the phase information $\varphi(t)$ over time.

Sudden body shaking or noise may occur during the measurement, and longer observation windows will provide better immunity to interference. The measurement will also be more accurate because the longer the data, the higher is the resolution of the FFT bins. In contrast, a shorter observation window provides a better real-time performance. The length of the observation window should be adjusted according to the application. In addition, if the subsequent windows are consecutive, the first stage of the IARBS method can be skipped after processing for the first observation window. Finally, the subject's thoracic displacement $x(t)$ is determined using Eq. 4.5.

Along with the heartbeat signal, $x(t)$ includes the respiration signal and other noises (e.g., body and radar shaking). Wavelet transform and bandpass filter are two techniques for extracting heartbeat signals [41]-[42], [86]-[87]. However, these conventional techniques have limitations because the heartbeat signal differs from person to person and the human heart rate is close to the high-order harmonics of the respiratory frequency.

An improved empirical mode decomposition (EMD) method called

ICEEMDAN can adaptively divide a signal into a limited number of intrinsic mode functions (IMFs) depending on the time scale of the signal [43], [49]. Therefore, this study uses the ICEEMDAN method to decompose the $x(t)$ and reconstruct the heartbeat signal, which was confirmed in our previous work. The relationship between $x(t)$ and each IMF, and the residual $r_n(t)$ is given by Eq. 5.11.

$$x(t) = \sum_{i=1}^{n} \mathrm{IMF}_i(t) + r_n(t) \quad i = 1, 2, 3 \dots n \tag{5.11}$$

Then all IMFs perform a spectral analysis. The IMF with energy concentrated at 0.8 Hz to 2.0 Hz as heart IMF is extracted to reconstruct the heartbeat signal, and the heart rate can be calculated [32].

5.3 Experiment

5.3.1 Equipment

In this experiment, a stepping motor with the specification NEMA17 was employed, and an Arduino UNO development board was used to connect the motor to the computer. The angle information of the subject was transmitted from the computer to the Arduino via serial communication. This motor is a hybrid stepping motor that combines the benefits of reactive and permanent magnet types. It has a high resolution, speed, and torque, and the specific parameters are listed in Table 5.1.

The radar module used in this research was based on Texas Instruments Inc. IWR1443. It operates at frequencies in the 77-81 GHz range and can continuously chirp up to 4 GHz. However, the radar module can only send chirp signals with a

bandwidth of 3.6 GHz during operation, owing to local laws in Japan. Furthermore, the maximum effective isotropic radiated power (EIRP) complies with the Japanese Radio Law and the FFC regulations. It does not cause harm to the human body. In contrast to the SISO mode used by traditional heart rate measurement techniques, in this study, the radar uses a 1Tx4Rx mode to gather data on the subject's angle. The main parameters of the radar module are listed in Table 5.2.

Table 5.1 Motor parameters list.

Type	Bipolar stepping motor
Stepping angle	1.8 deg.
Stepping mode	Full-step
Hold torque	5500 g·cm
Rated voltage	12 V
Rated current	1.5 A

Table 5.2 Radar module main parameters.

Parameter	Value
Bandwidth	3.6 GHz
Sweep time	51.4 μs
Frame length	50 ms
Slope	70 MHz/μs

Although the MIMO mode provides a better angular resolution than the SIMO mode, the SIMO mode is utilized in this study for the following reasons.

First, the background of this application is the medical monitoring of older people living alone. In most cases, there is typically no interference from other moving targets after screening using range-FFT and Doppler-FFT processing.

Second, as discussed in Section III, after locking the target subject using the

proposed method, the range of the current target selection is restricted to the spatial plane based on the target position of the previous rotation period. Therefore, even if other subjects are present during the measurement procedure, the proposed method ensures that there is no interference from them.

Third, employing the 3Tx4Rx mode for radar will inevitably increase the frame period and the amount of computation. This will reduce the real-time performance of the motor rotation and lead to the possibility that the subject will be out of the measurement range. The SISO data is utilized to calculate the chest displacement; hence, switching to the MIMO mode while maintaining a constant frame time will reduce the length of the SISO data. The phase quality of the IF signal is subsequently reduced. To increase measurement accuracy, this study focus on the phase quality of the IF signal rather than just the angular precision and angular resolution of the target subject.

In addition, we proposed in [35] a measurement method to simultaneously measure the heart rate of multiple people while walking. The proposed method for this study tracks a target subject and measures the vital signs, aiming to maximize the measurement range. Theoretically, it can also obtain the vital signs of other people within the measurement range. Moreover, the motor rotation angle calculation algorithm can be initialized to change the target subject.

A physical diagram of the hardware is shown in Fig. 5.4. A bracket holds the radar module on a circular plate, and the stepping motor rotates the plate. A DC power supply feeds the motor.

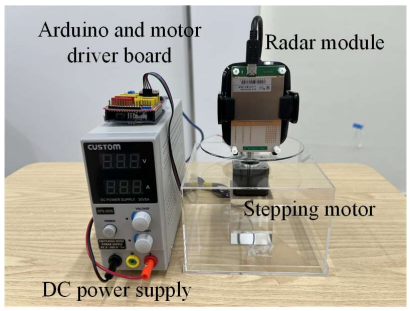

Fig. 5.4 The physical diagram of the hardware.

5.3.2 Experimental Environment and Route

The experiment for this study has four parts: a fixed route experiment, a random route experiment, an arm swing (more normal walking motion) comparison experiment, and a multi-subject scenario experiment.

There are five fixed routes, A, B, C, D, and E, as shown in Fig. 5.5 (a) and (b). Routes A, B, and C are horizontal lines with midpoints of 0.5, 1, and 1.5 m from the radar module, and their ends are at an angle of 90 degrees from the radar. Move along a straight line with an average speed of roughly 0.5 m/s and 1 m/s, starting at the right endpoint of each route. For simplicity, the routes are denoted as A1, B1, C1 (average speed of 0.5 m/s), and A2, B2, and C2 (average speed of 1 m/s), respectively. The x-axis and y-axis directions are also defined in the various subplots of Fig. 5.5.

Route D is a 180-degree arc with a radius of one meter centered on the radar coordinates. The starting point coordinates are (1, 0) and also move with an average speed of 0.5 m/s (route D1) and 1 m/s (route D2), respectively.

The above routes evaluate the feasibility of the proposed method, whereas route E is considered for its applicability. The subject traveled down route E in a 4 m × 2 m rectangle at a typical walking speed of 1 m/s. Furthermore, in the fixed

route experiment, the subject attempted to face the radar module with either the front or back of the body.

The random route is then a free walk within a 4.5 × 5 square meter area in front of the radar module to further measure the practical application potential of the proposed method.

There are two routes for the arm swing comparison experiment, as shown in Fig. 5.5 (d). Routes F1 and G1 indicate scenes without arm swings, whereas F2 and G2 indicate scenes with arm swings. The subjects moved along the route back and forth at an average speed of no more than 1m/s.

The multi-subject scenario experiment aims to demonstrate that the proposed measurement system can precisely track the target subject in this case. This experiment was conducted with three subjects simultaneously, as shown in Fig. 5.5 (e). Subject I, as the target, walked back and forth between 0.5 m and 3.5 m in front of the radar at an average speed of no more than 1m/s (with the arm swing). Subjects II and III walked randomly along a horizontal straight line 1 and 3 m from the front of the radar, respectively. This experiment can observe whether the orientation of the radar is interfered with by other people while the measurement system tracks subject I.

The subjects alternated between walking and constantly standing during each measurement period of 60 s to simulate the movement of people in the room. Fig. 5.6 depicts the actual experimental scenario. Additionally, the subject wore an ECG device to record heart rate data during the measurement.

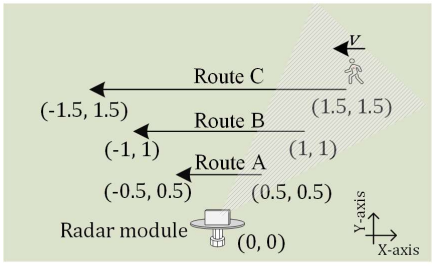

(a)

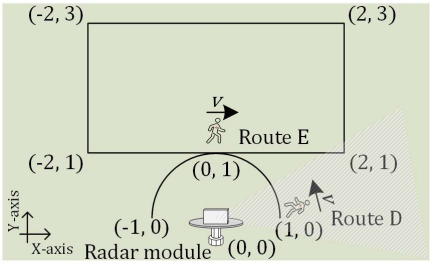

(b)

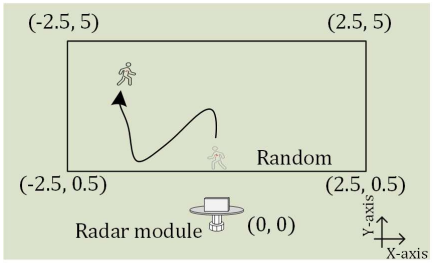

(c)

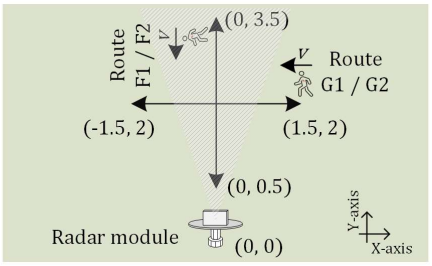

(d)

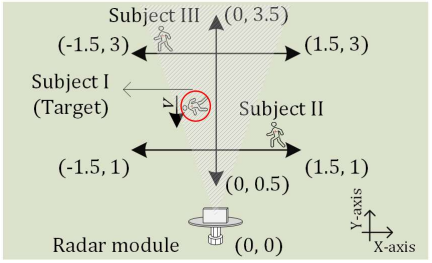

(e)

Fig. 5.5 Walking route maps of subjects.

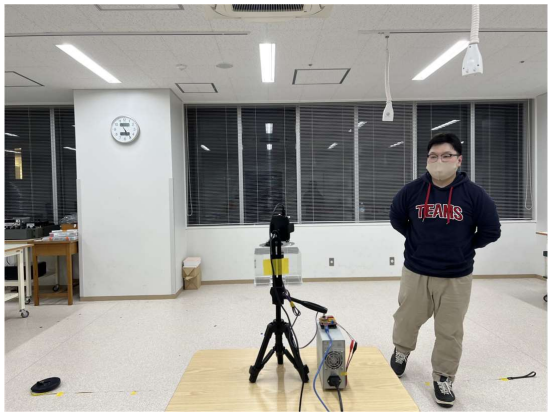

(a) Non-swinging arm scenario

(b) Arm swing scenario

(c) Multi-subject scenario

Fig. 5.6 The actual experimental scenario.

5.3.3 Parameter Analysis

The radar's horizontal left-half power angle is θ_{left}, and the minimum

measurement distance is $R_{\min}$. The following equation must be satisfied by the variables M and θ_s.

$$MT_f v_p < \frac{|\theta_{left} - \theta_s|\pi R_{\min}}{180^\circ}, \tag{5.12}$$

where v_p is the speed at which the person moves under normal conditions. As shown in Fig. 5.7, assume that the subject's distance from the radar is precisely $R_{\min}$ and that the subject's angle with the radar centerline is infinitesimally close to θ_s. In the next rotation period, the possible walking distance of the subject is at most $MT_f v_p$ to ensure that it is within the measurement range. In the context of the application of this measurement system, elderly individuals who live alone typically do not move indoors at speeds greater than 1 m/s. This experiment sets M and θ_s to 4 and 5 degrees because $R_{\min}$ is 0.5 m and the half-power angle of azimuth and elevation are about 70 and 10 degrees, respectively.

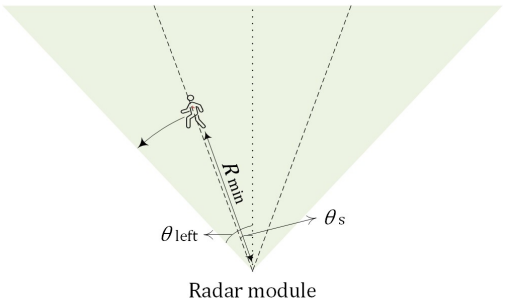

Fig. 5.7 The figure depicts how to select the appropriate minimum rotation angle by the half-power angle of radar.

5.3.4 Experimental Results

Six volunteers participated in this experiment, and Table 5.3 lists their heights and weights. In order to better evaluate the proposed approach, it is necessary to reduce the variable factors between the different subjects as much as possible.

Therefore, the height of the radar module was adjusted according to the thoracic height of the volunteer before the beginning of the measurement to try to keep both at the same horizontal plane. Each volunteer participated in all the routes of this experiment.

Table 5.3 Information about subjects.

Subject	Height [cm]	Weight [kg]
A	175	60
B	170	56
C	169	60
D	174	61
E	176	62
F	166	78

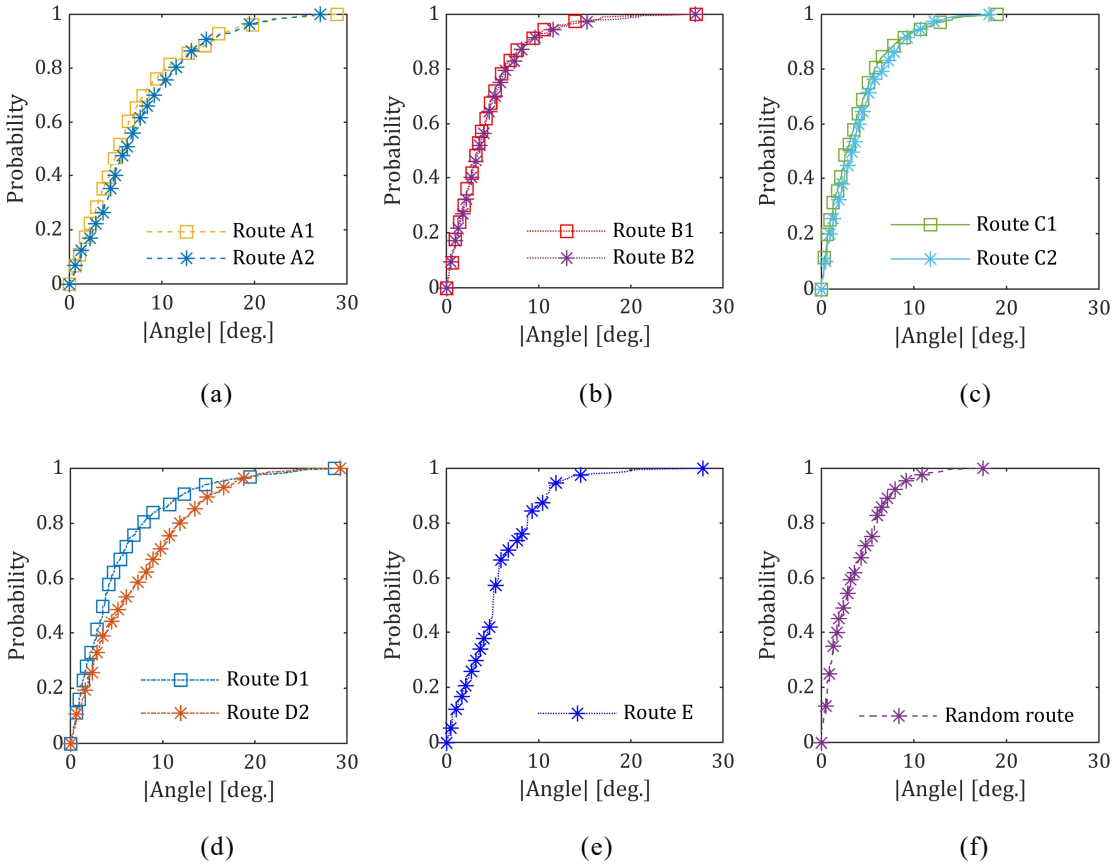

Fig. 5.8 The cumulative distribution functions of the absolute values of the measured subject's angle information. For simplicity, the routes are denoted as A1, B1, C1, and D1 (average speed of 0.5 m/s), and A2, B2, C2, and D2 (average speed of 1 m/s), respectively.

Fig. 5.8 shows the cumulative distribution functions (CDF) of the absolute values of the measured AoA (|Angle|: $\left|\boldsymbol{A}_{\mathrm{DM}}^{kM+1}{}_{(3,1)}\right|$) for each rotation period of the fixed route and the random route experiments for all subjects. Overall, the subjects remained within the ideal measurement range of plus or minus 35 degrees in front of the radar throughout the measurement cycle.

Owing to the subjects' faster angular velocity, as they moved along route A, the AoA values for route A were greater than those measured for the other routes. The results for routes B and C showed that in 90 percent of cases, the subjects had an AoA of less than 10 degrees. The AoA values increased with the movement speed of the subject. However, the effect is not particularly substantial, according to the combined results of all fixed route experiments.

The results for route D show that the measurement system tracks accurately even when the subject's angle changes by up to 180 degrees. Accordingly, depending on the requirements of the application, it is possible to position the radar module in the center of the room for 360-degree tracking measures. The angular velocity of the subject relative to the radar during route D was higher than that of routes A, B, and C, which led to a more significant difference in the results of the CDF of routes D1 and D2 than the other routes. In addition, the measurement system can accurately track the subject during random walks. In a few cases, the angle of the subject's position was approximately 30 degrees. However, no subject's position was outside the ideal measurement range, which demonstrates the reliability of the system.

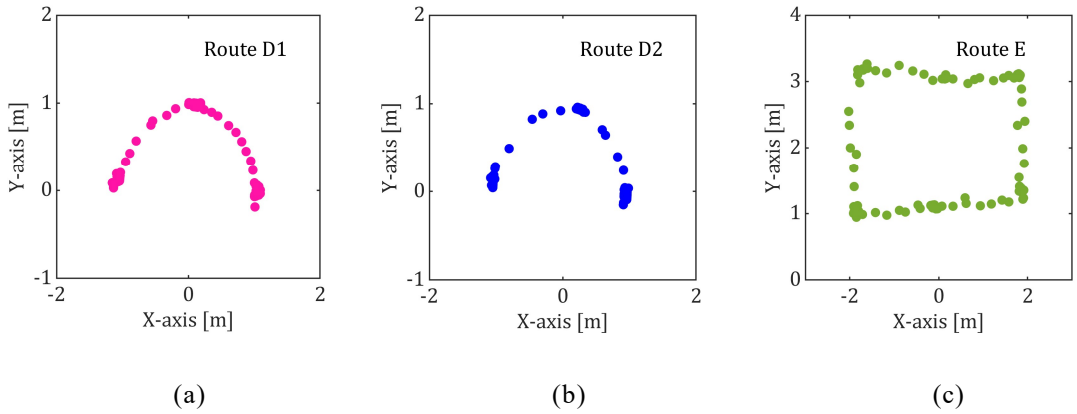

Fig. 5.9 The results of the traced trail for one subject walking along routes D and E.

Because route E contains straight lines similar to routes A-C, Fig. 5.9 shows only the results of the traced trail for one subject walking along routes D and E. The results show that the tracking trail is still rather precise, even if the proposed method quickly detects the subject's approximate location and sends it to the motor.

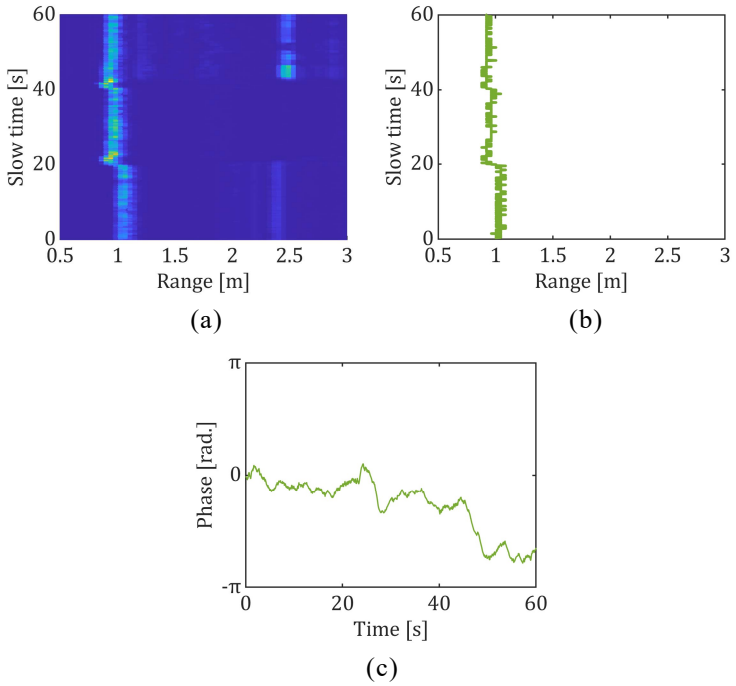

Fig. 5.10 The RPM (a) of a subject walking along route D2, the optimal range bin results (b) achieved by the IARBS method, and the stitched phase change information (c) are shown in this figure.

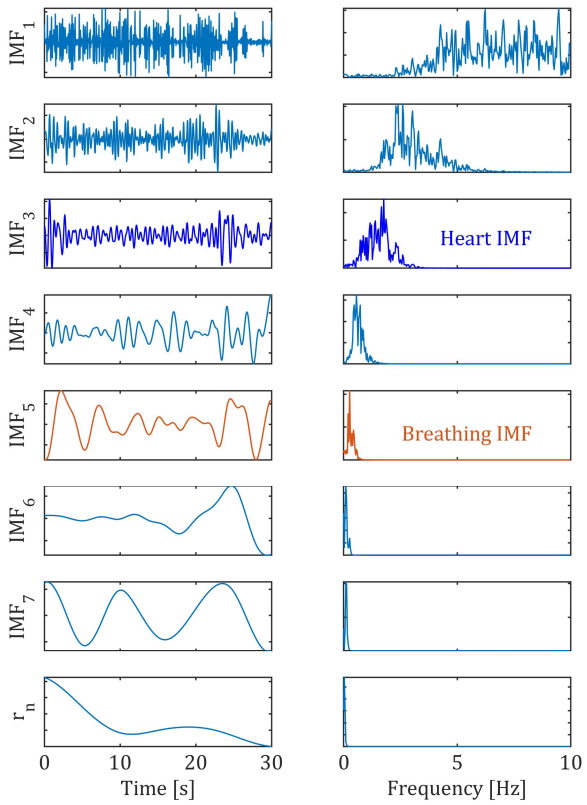

Fig. 5.11 Results of ICEEMDAN decomposition. The left and right sides are the time domain and frequency domain, respectively.

The RPM of a subject walking along route D2 and the optimal range bin results achieved by the IARBS method are shown in Fig. 5.10 (a) and (b). The phases extracted from the optimal range bins are then stitched together along the slow time dimension to calculate the $x(t)$ of the subject, as shown in Fig. 5.10 (c).

Next, $x(t)$ was decomposed into a finite number of IMFs using the ICEEMDAN method. FFT processing is performed on them to select the heart IMF among IMFs. The analysis was performed with a 30 s observation window. The results after decomposition by ICEEMDAN are shown in Fig. 5.11, with the time and frequency domains of each IMF on the left and right, respectively. According

to the frequency domain analysis, the heart IMF and breathing IMF were IMF_3 and IMF_5. This study focused on the heartbeat signal because the breathing signal is a low-frequency component that is simple to extract. Finally, the heartbeat signal was reconstructed. Finally, IMF_3 was used to reconstruct the heartbeat signal and estimate the heart rate.

In addition, the phase change data and low-frequency IMFs demonstrate that walking causes the $x(t)$ signal to vary more than when the subject is motionless [32].

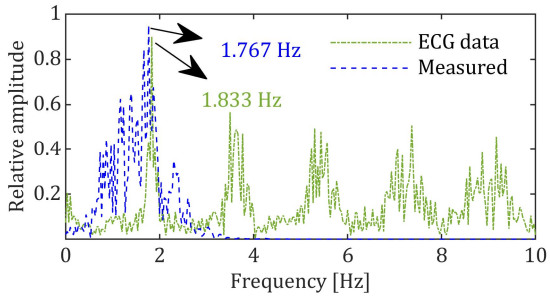

(a)

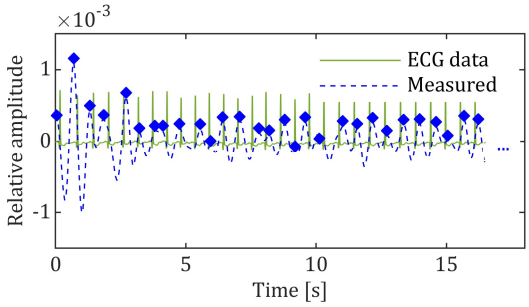

(b)

Fig. 5.12 (a) The frequency domain comparison of the reconstructed heartbeat signal and the ECG signal. (b) The time domain comparison of the reconstructed heartbeat waveforms and the ECG waveform.

Fig. 5.12 (a) shows a frequency domain comparison of the reconstructed heartbeat signal and ECG signal. These measurement data were obtained using

route D2. The heart rates obtained by the proposed method and ECG were 1.767 Hz and 1.833 Hz, respectively, with an absolute error of approximately 3.96 beats per minute (bpm), and the accuracy was approximately 96.4%.

The spectrum of the measurements is wider than that of the ECG. The following are some of the possible reasons for this phenomenon. Firstly, there is a fundamental difference between ECG, an electrical signal, and radar-based heart rate measurement, measured by a displacement signal from the skin. Secondly, the human chest skin is not plane, and the skin displacement caused by the heartbeat is slightly different at each location. Thirdly, the subject was walking, and there was inevitably a small amount of noise compared to stationary. The ICEEMDAN method has minimized the amplitude of the interference term as much as possible. In this research field, the most attention is paid to the accuracy of heart rate and RR interval measurements. Therefore, the practicality of the proposed method is not affected.

Table 5.4 Accuracy of heart rate measurement [%].

Route	**A1**	**A2**	**B1**	**B2**	**E**
Mean	98.42	97.47	97.29	96.78	97.19
Route	**C1**	**C2**	**D1**	**D2**	**Random**
Mean	97.69	96.64	98.06	97.08	96.16
Route	**F1**	**F2**	**G1**	**G2**	**Multi-subject**
Mean	97.05	96.75	97.83	97.27	96.22

Table 5.4 lists the average heart rate measurement accuracy for each route. The accuracy increased with proximity to the radar or slower speeds, and route A1 had the highest measurement accuracy at 98.42%. The results of routes F and G

show that swinging the arm while walking decreases the accuracy of the heart rate measurement by approximately 0.3% to 0.56%. The accuracy of the heart rate measurements decreased by 0.53%, while other people interfered. The overall average measurement accuracy, including the random route, was above 96%, thus maintaining a high level of accuracy.

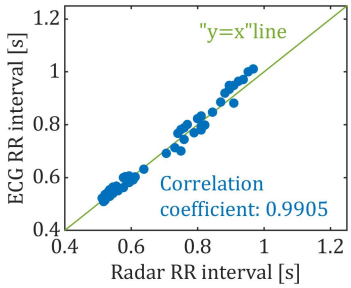

Fig. 5.13 The correlation of the RR interval measured by radar with ECG data.

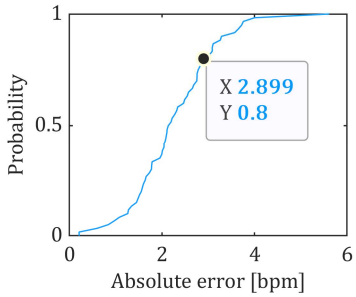

Fig. 5.14 The cumulative distribution functions of the absolute error of heart rate measurement.

To better observe the details, a portion of the reconstructed heartbeat waveform is compared with its corresponding ECG waveform in the time domain, as shown in Fig. 5.12 (b). The results showed a higher correlation between the measured heartbeat waveform's RR interval (spacing between rhombuses) and the ECG data. Meanwhile, Fig. 5.13 depicts the correlation between the mean RR interval time of all measurements of the fixed route experiment, random route experiment, and the corresponding ECG. The radar and ECG data were the

horizontal and vertical coordinates, respectively. The correlation coefficient γ of the two datasets was calculated using Eq. 5.13, and their correlation coefficient was 0.9905, indicating a high correlation between them.

$$\gamma = \frac{1}{P-1}\sum_{i=1}^{P}\left(\frac{F_i - \mu F}{\sigma F}\right)\left(\frac{E_i - \mu E}{\sigma E}\right), \tag{5.13}$$

where P and i are the total number of data and their indices, respectively. F is the data measured by the radar and E is the ECG data used as a reference. The means of the two data are μF and μE and their standard deviations are σF and σE. Fig. 5.14 shows the CDF of the absolute error of all fixed and random route experiment measurements. In 80% of the measurements, the absolute error was under 2.9 bpm. There were no instances when the absolute error exceeded 6 bpm, even when the random route results were considered.

To further quantitatively analyze the proposed method's heart rate measurement results, 60 s streaming data were analyzed with a 30 s observation window and a 1 s sliding step. Then, the heart rate for each observation window is calculated and contrasted with the ECG data to determine the root mean square error (RMSE), as shown in Eq. 5.14.

$$\text{RMSE} = \sqrt{\frac{1}{Q}\sum_{i=1}^{Q}(HRR_i - HRE_i)^2}, \tag{5.14}$$

where Q and i are the total number of observation windows and their index numbers, respectively. HRR and HRE are the heart rates measured by each

observation window and reference heart rate (ECG data), respectively.

Table 5.5 The RMSE of heart rate measurement.
(The fixed and random route experiment) [BPM]

Route \ Subject	A	B	C	D	E	F	Mean
A1	1.99	1.75	1.88	2.05	1.89	1.79	1.89
A2	3.71	3.38	3.78	2.68	3.94	1.86	3.23
B1	2.57	2.55	3.66	3.58	3.52	1.14	2.84
B2	3.99	3.82	4.67	3.85	3.25	3.74	3.89
C1	2.30	2.34	3.67	3.32	2.00	2.75	2.73
C2	5.32	3.03	4.25	3.72	3.86	4.03	4.04
D1	2.46	2.77	3.02	1.78	2.67	2.01	2.45
D2	2.64	3.91	3.83	5.23	3.05	3.44	3.68
E	4.01	2.42	3.73	5.39	2.45	4.00	3.67
Random	6.64	2.31	6.82	6.33	2.58	1.42	4.35

Table 5.6 The RMSE of heart rate measurement.
(The arm swing comparison experiment) [BPM]

Route \ Subject	A	B	C	D	E	F	Mean
F1 (No arm swinging)	3.46	1.64	2.59	3.13	3.49	3.59	2.98
F2 (Arm swinging)	3.67	3.45	2.50	3.19	3.85	4.18	3.47
G1 (No arm swinging)	3.44	3.26	4.02	3.41	3.95	4.00	3.68
G2 (Arm swinging)	4.37	3.32	4.75	2.77	4.06	4.32	3.93

Table 5.5 presents the RMSE of the heart rate measurements of the fixed and random route experiments. The results demonstrate that as the distance and speed increase, the RMSE of the heart rate estimation also increases. According to the average RMSE value for each route, the RMSE is approximately 1.2 bpm lower when the subject walks at 0.5 m/s as opposed to 1 m/s. We speculate that precision may be affected because the stepping motor rotates more frequently, causing the

fixed plate to vibrate and generate noise. Meanwhile, the experimental results of [35] demonstrated that the speed of the subject can affect how accurately the IARBS method chooses the optimal range bin. Additionally, the positive association between RMSE and distance will rise less quickly or stop being significant if the subject's distance from the radar exceeds 1 m. Likewise, when the subject moves at a speed of 1 m/s, the rate at which the RMSE increases with distance will decrease. Therefore, the experimental results showed that the RMSE values of the proposed method for heart rate estimation converged to a particular value and were stable.

The heart rate estimates are highly accurate even when the subject's angle information changes significantly, as evidenced by the mean RMSEs of 2.45 bpm and 3.68 bpm for routes D1 and D2, respectively. The results for each volunteer in the random route experiment varied significantly. However, the RMSEs were all below 6.9 bpm, with a mean value of 4.35 bpm. Some of the larger RMSEs are caused by spending extended periods with the side of the body facing the radar, which decreases the measurement accuracy.

Table 5.6 presents the RMSE of the arm swing comparison experiment's heart rate measurements. Notwithstanding individual variations, swinging of the subject's arm throughout the measurement process can affect the measurement accuracy. During the arm swing, the average RMSE of routes F and G decreased by 0.49 bpm and 0.25 bpm, respectively. This influence is caused by the left anterior thoracic muscle movement when the arm is swung, and the movement of

the upper arm also causes a change in the phase of the IF signal.

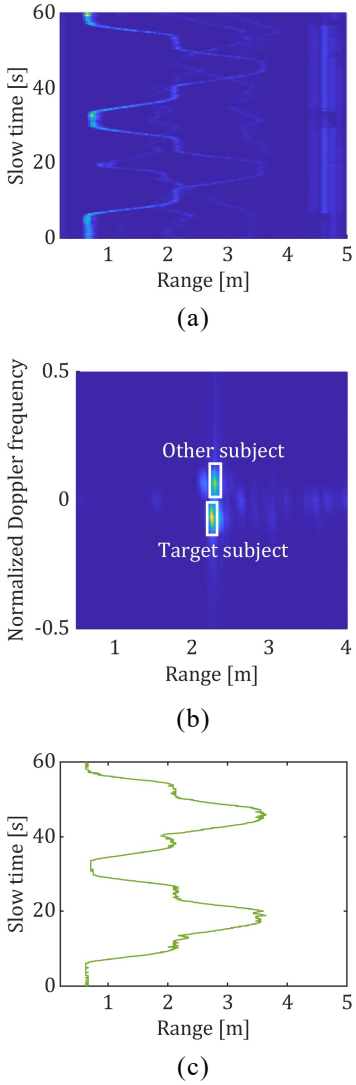

Fig. 5.15 The RPM (a) of the multi-subject scenario experiment, the RDM (b) of a certain frame during the measurement, and the optimal range bin results (c) of the target subject achieved by the IARBS method are shown in this figure.

Fig. 5.15 (a), (b), and (c) depict the RPM of the multi-subject scenario experiment, the RDM of a certain frame during the measurement, and the optimal range bin results of the target subject achieved by the IARBS method, respectively. The target subject was within the measurement range at all times and the rotation

of the radar module was not disturbed by other people. Fig. 5.15 (b) shows the RDM when the target subject and other subjects overlapped on the RPM. The IARBS method can adaptively adjust the peak-seeking range based on the velocity of the target subject in the previous time. It is robust to other subjects suddenly entering its peak-seeking range. Even if other subjects are at the same range bin as the target subject for an extended time, their heart rates can be separated by the ICEEMDAN method. Fig. 5.15 (c) shows that the IARBS method can accurately select the optimal range bin of the target subject in the multi-subject scenario. However, there are many interference factors in this case, such as the possible presence of multiple subjects' arm swings and body shaking simultaneously in one range bin cell.

As discussed in subsection 5.2, longer observation windows result in better interference immunity. Fig. 5.16 compares the heart IMF and ECG data in the frequency domain for each observation window in the multi-subject scenario experiment. The ECG data showed that the mean heart rate during the measurement period was 1.402 Hz. No significant peaks in the heart IMF made it challenging to estimate the heart rate, whether the observation window was 30, 40, or 50 s. The peak frequency is 1.417 Hz when the observation window is 60 s, and the absolute error is about 0.9 bpm compared to the ECG data, with an accuracy of 98.93%. The measurement accuracies of the six subjects were 95.37%, 98.93%, 95.55%, 96.28%, 95.49%, and 95.69%, respectively, with a mean value of 96.22%. The measurement accuracy of this experiment was also influenced by the random

movements of the non-target subjects, which were similar to the random route experiment. The experimental results show that the heart rate measurement for the target subject still maintains a high accuracy in multiple people scenarios.

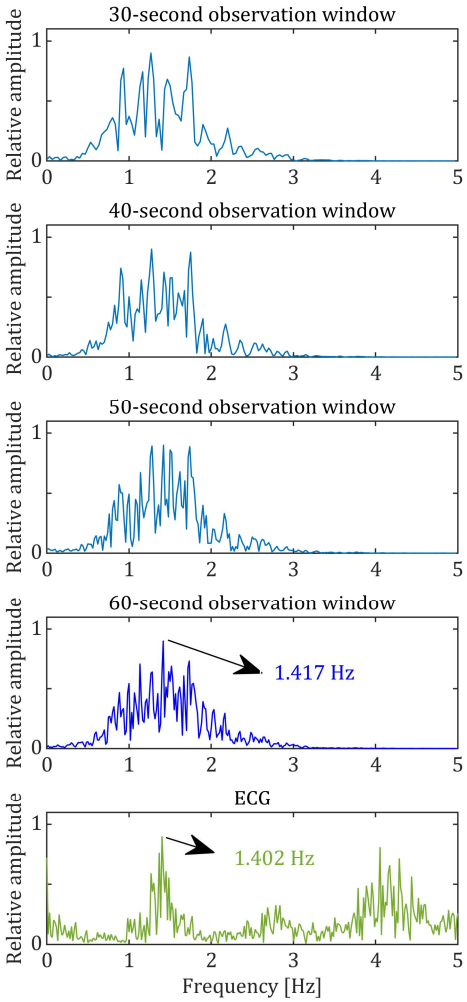

Fig. 5.16 Comparison of heart IMF and ECG data in the frequency domain for each observation window in the multi-subject scenario experiment.

In addition, it is challenging to improve real-time performance by shortening the observation window whenever heart rate is measured using FFT-based time-frequency domain analysis, including the ICEEMDAN method. For example, when the frame period is 0.05 s (typical), and the observation window is below 10 s and 5 s, the spectrum's frequency resolution will be as low as 0.1 Hz and 0.2 Hz.

Meanwhile, the EMD-based algorithm (ICEEMDAN) is required for the data's length, which is not sufficient to separate the individual frequency components if it is too short. [32], [77] using EMD-based algorithms to measure heart rate with the subject at stationary have employed an observation window of at least 15 s. Since the subject in this study was moving, the evaluation was attempted with an observation window of 30 s or more.

Fig. 5.17 shows two spectrums of heart IMF measured with a 10-second observation window. As shown in Fig. 5.17 (a) and (b), the heart rate can be easily detected when interference is low in the spectrum of the heart IMF. However, the low frequency resolution of the spectrum resulted in a measurement error of 0.2 Hz. Due to the shortness of the data, heart rate estimation will become difficult when ICEEMDAN cannot efficiently extract high-quality, low-interference heart IMF, as shown in Fig. 5.17 (c) and (d). Interference occurs randomly, and clearly, longer observation windows possess better robustness.

In order to trade off the real-time performance and stability of the measurement system, the following attempts are considered in future work. One is to shorten the frame period as much as possible to increase the data length, provided the radar hardware supports it. The other one is that the application uses an overall delayed dynamic display when displaying heartbeat waveforms. The next measurement and processing are performed simultaneously during the previous waveform display. When the previous waveform is just about finished, the next waveform is displayed immediately afterward.

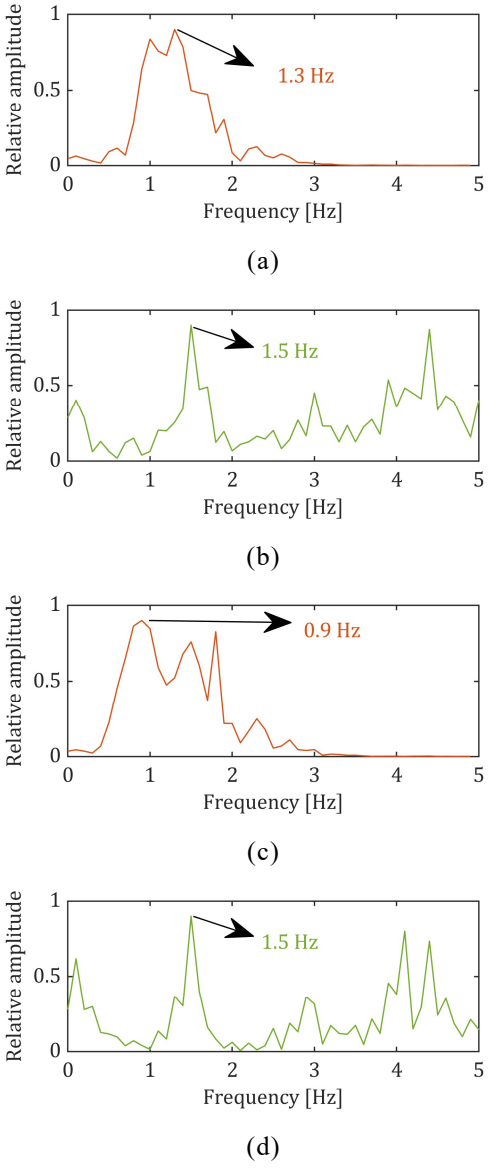

Fig. 5.17 In (a) and (c), the two spectrums of heart IMF were measured with a 10-second observation window, and the ECG data corresponding to them are shown in (b) and (d).

Because this study is the first to estimate the heart rate by adjusting the radar measurement range through stepping motors, the measurement results are difficult to compare quantitatively with other papers. Therefore, the main focus is the qualitative comparison and analysis of this experiment's results with those of other works' measurements.

Most radar-based heart rate estimation methods, such as those in [26], [44], [50], [61]-[62], [65]-[67], [71]-[80], cannot perform tracking measurements on moving targets, whereas the proposed method offers this possibility.

In the experiment in [69], the subject moved slowly and the heart rate was measured with 90% accuracy. In [59], the subjects made only backward and forward movements with a measurement error range of 0-8 bpm. By contrast, the subjects in this experiment were faster, and the RMSEs of the measurements were all below 7 bpm. Moreover, the average measurement accuracy for each route exceeded 96%. The measurement accuracy in our previous study [35] was 95.88%. This is because the subject was consistently inside the ideal measurement range in this experiment, which increased the accuracy.

The six participants in [77] were in a stationary state. At distances of 1 m, 1.5 m, 2 m, and 2.5 m from the radar, the mean values of the RMSE for heart rate estimation were approximately 2.39 bpm, 2.57 bpm, 3.23 bpm, and 4.69 bpm, respectively. Although the results for routes B and C were higher than 2.39 and 2.57 bpm, the farthest distance in route E was about 3.61 m, and the mean value of RMSE was only 3.67 bpm. In addition, the proposed method can change the radar orientation to adjust the measurement range and estimate the heart rate of a moving person, making it more advantageous for application.

5.4 Summary of Chapter 5

In conclusion, this chapter proposes a novel radar-based adaptive tracking method for measuring the heart rate of a moving subject. The proposed algorithm

is employed to determine the position of the subject to control a stepping motor that adjusts the radar measurement range. The results of the fixed-route experiments revealed that when the subject was moving at a speed of 0.5 m/s, the mean values of RMSE for heart rate measurements were all below 2.85 bpm, and when moving at a speed of 1 m/s, they were all below 4.05 bpm. When subjects walked at random routes and speeds, the RMSE of the measurements were all below 6.85 bpm, with a mean value of 4.35 bpm. In addition, this study not only evaluated the potential effect of arm swing (more normal walking motion) on heart rate measurement but also demonstrated the ability of the proposed method to measure heart rate in a multiple-person scenario.

Meanwhile, the overall measurement accuracy was greater than 96%, when the random route was included. Moreover, the RR intervals of the reconstructed heartbeat signal and ECG data were highly correlated, with a correlation coefficient of 0.9905. In the future, we plan to improve the experimental platform to reduce the noise generated by the radar as it rotates to improve the accuracy of the measurements.

Chapter 6 Vital Signs Monitoring Mobility Robot Based on Radar

6.1 Research Background for Chapter 6

In [32], we tried to measure from multiple directions. The improved adaptive range bin selection (IARBS) method is proposed to address the limitation of conventional measurements that require the subject to remain stationary [35]. Furthermore, the specifications of the radar module limit the valid measurement range. We also proposed a method to measure the heart rate while tracking the subject by mounting the radar module on an automated rotation pedestal [36]. However, the measurement accuracy decreases when the subject is far from the radar. [81] proposed the idea of combining robots for measurements, but the subject still needs to remain stationary.

This chapter proposes a novel measurement method combining radar and robotics, monitoring the heart rate of a moving subject by tracking him or her in real-time. This is the first attempt in this research area to our knowledge. Based on our previous work [88], a preliminary experimental platform is built, and the results of its measurements are shown.

6.2 Measurement Principle

Radar-based remote measurements are susceptible to factors such as distance and angle. Measurement becomes problematic when the subject is out of the valid measurement range. For this reason, we propose a novel measurement method in

which a radar module is mounted on a mobility robot, and its orientation is adjusted in time according to the subject's position. This method ensures that the subject is always within the appropriate measurement range.

The proposed method can be divided into two parts: tracking method and heart rate measurement, and its processing flowchart is shown in Fig. 6.1.

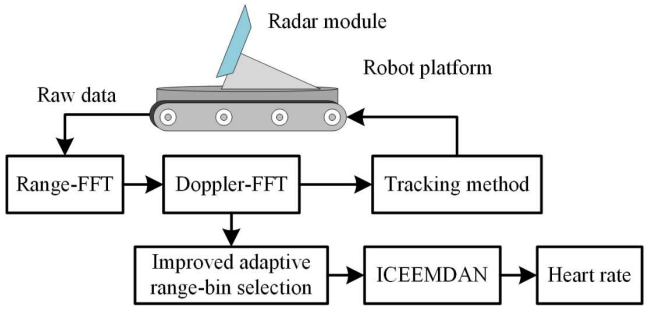

Fig. 6.1 The processing flowchart for proposed measurements method.

6.2.1 Tracking Method

In this study, as with conventional heart rate measurements, frame duration is set based on 2-5 times the usual maximum heart rate or higher. This value usually is 0.05 seconds at 20 Hz. The difference is that multiple chirp signals are emitted in each frame cycle to obtain the subject's distance, speed, and angle information. In contrast, in most past studies, there is typically only one chirp signal in a single frame.

The target is tracked using the classical 3D-FFT method in conjunction with the 2D-CFAR algorithm. Each IF signal is sampled and transmitted in frames as raw data to the computer. Range-FFT processing on each raw data matrix's fast time dimension yields a range profile matrix (RPM) containing target distance information. Doppler-FFT processing is then performed on the slow time

dimension of the RPM to obtain the range-Doppler matrix (RDM) containing the velocity information.

Since the quality of RDM may be interfered with by noise, the target is extracted from the RDM using the 2D-CFAR algorithm. The commonly used approaches are 2D-CA-CFAR, 2D-OS-CFAR, and others [83]-[84]. 2D-OS-CFAR is computationally intensive but performs better in the presence of strong interference targets [85]. This study's real-time response requirement is high, so the 2D-CA-CFAR algorithm is chosen because of its computational simplicity and good performance in pure-noise situations.

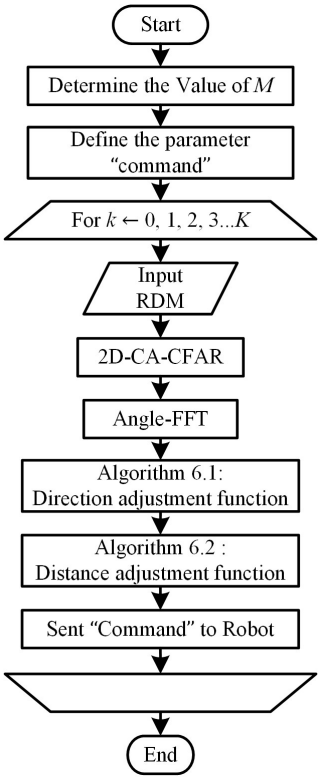

Fig. 6.2 The processing flowchart for tracking method.

The processing flowchart for tracking method is shown in Fig. 6.2. Since the subject walks slowly, performing target tracking processing for each RDM is

unnecessary. Assuming that tracking is performed every M frames, the number of frames requiring 2D-CA-CFAR processing is kM+1 (k=0, 1, …, K). After 2D-CA-CFAR processing, the angle information θ_s^{kM+1} of the current frame of the subject is extracted by angle-FFT.

The robot tracks the subject in two steps: direction adjustment and distance adjustment. The direction adjustment function and the distance adjustment function are implemented through Algorithm 6.1 and 6.2, respectively.

When the subject moves away from the radar module, it just reduces the measurement accuracy. However, when the angle of the subject changes significantly, it may go out of the effective measurement range, failing to monitor the heart rate. Therefore, Algorithm 6.1 should generally be prioritized to be executed to reorient the robot.

At the same time, a distance warning threshold R_w is set to prevent a situation where the subject is already far away from the radar module but is still in Algorithm 6.1. When the current distance R_0^{kM+1} exceeds the threshold value R_w, the computation of Algorithm 6.1 will be skipped so that Algorithm 6.2 can be directly executed to adjust the distance in time.

As minor angular variations do not affect the measurement, they are filtered out by the threshold θ_t for direction adjustment. Right steering or left steering only when the absolute value of the required adjustment angle is greater than θ_t and greater or less than zero. If the above conditions are not met, Algorithm 6.1 is skipped, or the operation is not performed.

Algorithm 6.1 Direction adjustment function.

θ_s^{kM+1} is the angle information of the subject ;

θ_t is the minimum threshold for direction adjustment ;

R_w is the distance warning threshold of the subject ;

R_0^{kM+1} is the distance information of the subject ;

Command is the command parameter passed to the robot ;

If $R_0^{kM+1} < R_w$ **then**

  If $\left|\theta_s^{kM+1}\right| > \theta_t$ **then**

    If $\theta_s^{kM+1} > 0$ **then**

      Command ← turn_right ;

    Else

      Command ← turn_left ;

  Else

    Command ← do nothing ;

Else

  Goto **Algorithm 6.2**

Return: Command ;

Algorithm 6.2 Distance adjustment function.

R_0^{kM+1} is the distance information of the subject ;

R_{mind} is the lower limit of the optimal measurement range ;

R_{maxd} is the upper limit of the optimal measurement range ;

Command is the command parameter passed to the robot ;

If $R_0^{kM+1} > R_{mind}$ **and** $R_0^{kM+1} < R_{maxd}$ **then**

  Command ← do nothing ;

Elseif $R_0^{kM+1} > R_{maxd}$ **then**

  Command ← advance ;

Elseif $R_0^{kM+1} < R_{mind}$ **then**

  Command ← backwards ;

Return: Command ;

Algorithm 6.2 adjusts the front and back position of the robot based on the real-time distance information of the subject to ensure that it is within the

appropriate measurement distance. This range's upper and lower thresholds are R_{maxd} and R_{mind}, respectively. No action will be taken if the subject is located in it. When greater than R_{maxd} or less than R_{mind}, the robot performs advancement or backward movement until the subject is within the optimal measurement range.

6.2.2 Heart Rate Measurement Part

The accuracy of heart rate measurements is evaluated in terms of observation windows. Splice all RPMs in the observation window period along the slow time dimension. The phase of the range bin where the subject is located is then sequentially extracted along that dimension by the IARBS method and stitched together into phase change information $\varphi(t)$ [35]. Immediately after that, based on Eq. 2.5, the chest displacement information $x(t)$ of the subject can be calculated.

The unprocessed $x(t)$ contains various noises, decomposed into several intrinsic mode functions (IMFs) and the residual $r_n(t)$ using the improved complete ensemble empirical mode decomposition with adaptive noise (ICEEMDAN) method, as shown in Eq. 6.1. FFT then processed all the decomposed components, and the IMF correlated with heart rate is extracted by IMF filter, and its peak frequency is the estimated heart rate value [32].

$$x(t) = \sum_{i=1}^{n} \text{IMF}_i(t) + r_n(t) \quad i = 1, 2, 3 \ldots n \tag{6.1}$$

6.2.3 Experimental Platform

The experimental platform is shown in Fig. 6.3 (a). A radar module used in this study is based on the IWR1443 millimeter-wave radar chip from Texas

Instruments Inc. in the United States, which has a maximum sweep range of 77 GHz to 81 GHz. The radar module is a MIMO radar in 3Tx4Rx mode. It complies with Japanese Radio Laws and FFC regulations and does not harm the human body. The main parameters of the radar module are listed in Table 6.1.

(a)

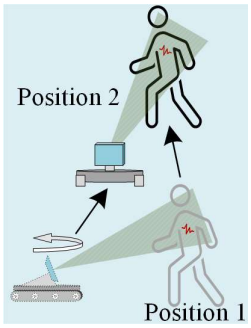

(b)

Fig. 6.3 The figure (a) is the actual experimental platform, and figure (b) is a schematic of how it works.

Table 6.1 The main parameters of the radar module.

Parameter	Value
Bandwidth	3.6 GHz
Sweep time	51.4 μs
Frame length	50 ms
Slope	70 MHz/μs

The mobility robot platform has a set of tracks on each side, each driven by a DC motor. The steering of the robot is realized by adjusting their speed difference. This allows for in-situ steering, which is more flexible than Ackerman steering.

The control board uses an Arduino's three-in-one series, connected to the computer and the motor's driver at each end. The control board receives the Command parameter from the computer at frame $kM+1$ (k=0, 1, …, K) and passes it to the motor drive to control the direction of movement of the motor. Furthermore, the motor set is powered by six dry-cell batteries, eliminating the need for an additional DC power supply.

The holder fixed the radar module on top of the robot platform. In [32], we have demonstrated the feasibility of making measurements of heart rate from the oblique front. Therefore, it is also feasible for the radar to take measurements from the subject's oblique underside in this study.

In general, the chest portion of the adult body is roughly 1.1 to 1.6 meters above the ground. Assume that the radar is at a distance of H_{r} meters from the ground and that the angle made with the horizontal plane is θ_{r} degrees. Then, the upper and lower thresholds of the optimal measurement range (R_{maxd} and R_{mind}) can be found by trigonometric relationships.

As shown in Fig. 6.3 (b), when the subject walks from position 1 to position 2, the robot will first steer to ensure that the subject's position does not exceed the valid measurement angle and then move forward to approach the subject to keep it at the appropriate distance.

6.3 Experiments

The experimental scenario is shown in Fig. 6.4 (a), where the subject walks in the range shown in Fig. 6.4 (b) with an average of 0.5 m/s in four directions: back, forth, left, and right. Since this was the first attempt in this field, the subject was slow, and the experiment was conducted in an ideal environment without interference from other objects. Second, the subject tried to face the radar as much as possible in a frontal direction during the measurement. A total of 14 measurements were taken, each of which lasted 60 seconds. The subject wore an ECG device to obtain ECG data to evaluate the measurements' accuracy.

(a)

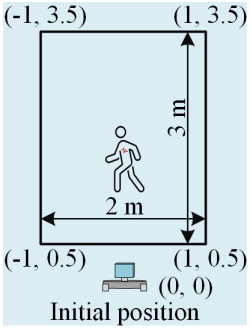

(b)

Fig. 6.4 The experimental scenario and the subject's walking range are shown in (a) and (b).

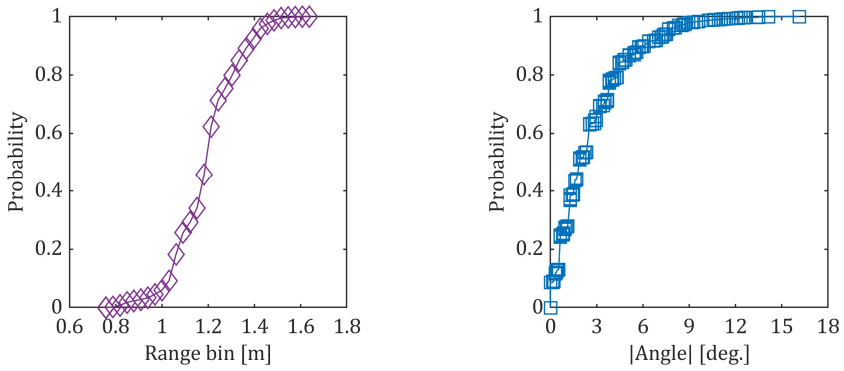

(a) (b)

Fig. 6.5 The cumulative distribution functions of the measured range bin and absolute angle are shown in (a) and (b).

In this experiment, H_r was about 0.1 m, and θ_r was 45 degrees, so the appropriate measurement range was 1-1.5 m. The horizontal half-power angle of the radar is plus or minus 35 degrees. The cumulative distribution functions of all tracking processing's measured range bin and the absolute angle are shown in Fig. 6.5 (a) and (b). The probability that the subject was at [R_{maxd}, R_{mind}] was 99.48%. The angles at which the subject was positioned were all below the half-power angle. Furthermore, the angles were less than 6 degrees in about 90% of the cases.

The results of heart rate measurements are listed in Table 6.2. The accuracy of the 10th and 14th measurements is slightly lower than the others. This is because of the faster walking speed of the subject and the longer time required for the robot to adjust the distance and direction, which leads to a loss of accuracy. Regardless, the accuracy of each measurement was higher than 92%. Most radar-based heart rate measurement studies, such as the methods in [35], [62], [65], [74]-[75], cannot perform tracking and measurements on moving targets, while the proposed method provides this possibility. Therefore, quantitatively comparing the measurements in

this study with conventional measurements is difficult. The mean absolute error was 0.063 Hz, and the mean accuracy was 95.47% in this study, comparable to the experimental results (95.88%) of our previous work [35], demonstrating the validity of the methodology of this proposed method.

Table 6.2 The results of heart rate measurements. [Hz]

No.	ECG	Measurement	Absolute Error	Accuracy
1	1.400	1.333	0.067	95.21%
2	1.359	1.283	0.076	94.11%
3	1.446	1.417	0.029	97.99%
4	1.253	1.217	0.036	97.13%
5	1.498	1.433	0.065	95.66%
6	1.459	1.400	0.059	95.96%
7	1.097	1.167	0.070	93.62%
8	1.006	1.017	0.011	98.91%
9	1.140	1.200	0.060	94.74%
10	1.518	1.417	0.101	93.35%
11	1.432	1.350	0.082	94.27%
12	1.598	1.667	0.069	95.68%
13	1.508	1.550	0.042	97.21%
14	1.492	1.389	0.109	92.69%
Mean			0.063	95.47%

6.4 Summary of Chapter 6

This chapter proposed a novel remote heart rate measurement method based on radar and a mobility robot. The method adaptively adjusts the radar to be in an appropriate measurement position and can also measure heart rate while the subject walks. In the future, we plan to add the ability to adjust the vertical angle of the radar module. In addition, to cope with the actual environments, it is necessary to

improve the algorithm to correctly discriminate between the subject and other objects before the continuous tracking process begins. It is also planned to consider the conditions to jump out of the tracking process to research for the subject's position.

Chapter 7 A Web Application for Remote Vital Signs Monitoring and Position Using Radar

7.1 Research Background for Chapter 7

Population aging is a concern for humanity, and according to a 2019 survey, Japan's population aging rate was the highest in the world, at 27% [3]. Because of longevity, radar-based non-contact vital sign measurements are beginning to be used in seniors living alone and in nursing homes. The mm-wave frequency modulated continuous wave (FMCW) radar is a type commonly used for vital sign monitoring [50], [79]-[80].

However, the subjects in the study of [50], [78]-[80] conducted their measurement under stationary conditions, which means their movements must be limited to obtain the results. Even though restricting the subject's movements leads to obtaining vital signs much more precisely, it results in challenges of applying in normal daily life. For this, we propose a method that measures the subject's vital signs while walking [35] and a measurement method that tracks the subject through an adaptive rotating platform [36].

In addition, how to inform the guardians and doctors about the measured data in real-time or notify the corresponding medical institutions in case of emergency is also an issue that needs attention. Preceding studies of monitoring vital signs through mobile devices use native applications [89]. As the native application is developed in the specified operating system (e.g., Windows, Android, and iOS), it

causes environmental dependency on users, resulting in low accessibility. On the other hand, web applications can be accessed through any environment with any third-party web browser. Besides, as standard markup languages are utilized when developing web applications, their maintenance is more cost-effective and convenient than native applications.

In this study, we propose a system design for a web application that can monitor the subject's heart rate and position data obtained by mm-wave FMCW radar. We use the signal processing methods proposed in previous work [35], [36] and [39] to obtain vital signs and position data. The system is designed to enable computing software to communicate with the cloud computing platform, making signal processing data suitable for monitoring. This study uses MATLAB for signal processing and Amazon Web Service (AWS) for the cloud platform.

7.2 System Configuration

A data transfer flowchart is shown in Fig. 7.1. It comprises three components: hardware, a computer, AWS. MATLAB software performs the suggested algorithm and signal processing. Then, the MATLAB Interface for Amazon Simple Storage Service (S3) sends the results to the AWS. Meanwhile, the Java Runtime Environment (JRE) is required for communication between MATLAB and AWS S3. In addition, specific Amazon S3 bucket information must be registered on a PC using the AWS Command Line Interface (CLI) [90]. Next, the heart rate and position data are converted into a comma-separated values (CSV) file and transferred to the cloud in real time.

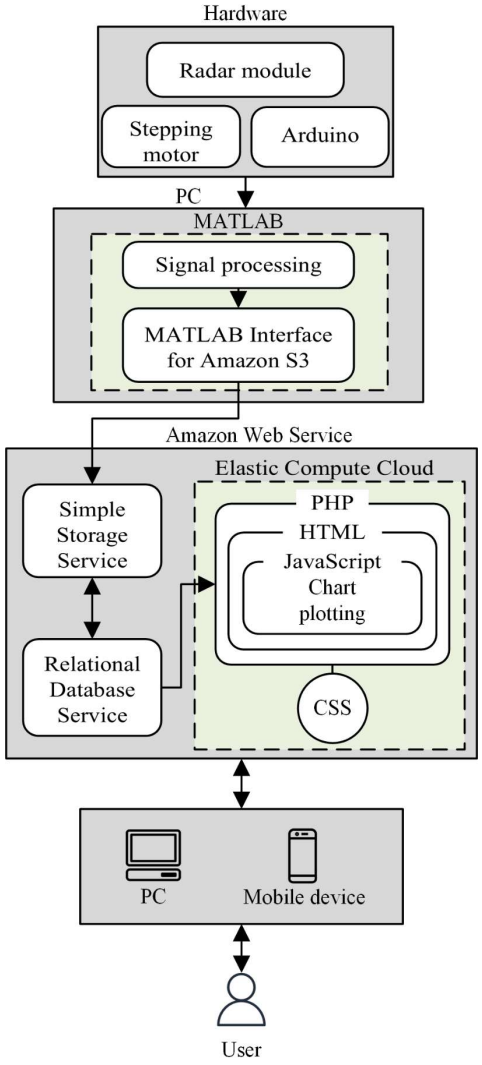

Fig. 7.1 The system configuration diagram.

Databases with heartbeat and position schemas are located on a relational database service (RDS) with MySQL installed. The AWS Elastic Compute Client (EC2) provides a virtual instance and is used as a web server. This study uses Ubuntu as a server operation system (OS) for its distribution [91]. The configuration of AWS EC2 is depicted in Fig. 7.1, which includes a PHP: Hypertext Preprocessor (PHP), HyperText Markup Language (HTML), JavaScript, and Cascading Style Sheets (CSS).

The PHP interacts with the AWS RDS to query databases that store position and heartbeat data. When the PHP requests data, HTML creates the document object model (DOM), which is divided into four sections: the position graph area, the current date, the time indication area, and the heartbeat graph area. CSS controls the output styles on the web browser and manages all the DOMs. In this manner, a user can access a web browser to view the measurements' results and the subject's real-time location.

7.2.1 Data Processing for Database

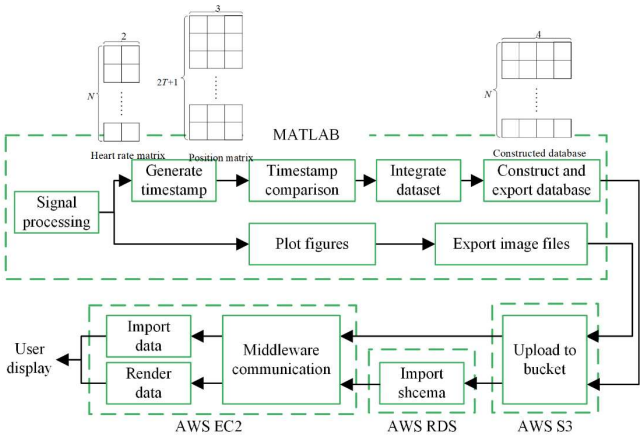

Fig. 7.2 The flow chart of data processing.

Obtained data consists of vital signs data and position data. About the former, the chest displacement information is extracted by performing the (IARBS) method on the range-Doppler matrix (RDM) [35]. The heartbeat signal, as well as the heart rate, is then obtained through the improved complete ensemble empirical mode decomposition with adaptive noise (ICEEMDAN) [32]. The obtained heartbeat data matrix length is $20T$ when the measurement period is T seconds and a frame period of 0.05 seconds. The latter, on the other hand, is calculated by angle-FFT,

which process of angle calculation is performed every 0.5 seconds. Therefore, the obtained position data matrix length is $2T$+1 [36].

As shown in Fig. 7.2, the heart rate dataset with a timestamp generated is determined as a time and frequency matrix with N rows and two columns. N is the total number of points obtained after instantaneous frequency estimation.

Likewise, the position dataset is determined as a form of time and two-dimensional coordinate with $2T$+1 rows and three columns. Timestamps of each dataset are compared for database construction. They are integrated as a format of JavaScript Object Notation (JSON), a file format for referring to the data from the database management system.

Transferring data to AWS is needed as the MAT-file output is stored in local storage. In order to communicate with AWS S3, Java Runtime Environment (JRE) is installed on local storage. Also, specified information such as AWS Identity and Access Management (IAM) and Amazon Resource Name (ARN) of the AWS S3 bucket is registered through the AWS CLI.

7.2.2 Implements of AWS

After transferring data from local storage to the AWS S3, image files and the dataset of heartbeat and position are stored in the bucket of the AWS S3. To utilize the dataset as a database schema, the AWS RDS with MySQL 8.0.32 installed query data from the AWS S3. Meanwhile, the AWS EC2 provides a virtual instance with Ubuntu 22.04 installed for its operating system. On the instance of the AWS EC2, Node.js 18.14, a V8 JavaScript Engine-based runtime, was installed for running WAS. Node.js processes events by non-blocking input and output method, which

is proper for the system, such as frequently updated data monitoring. From the perspective of effectiveness and stability for running the WAS, a database schema is not stored on AWS EC2. Instead, the server fetches data using Asynchronous JavaScript and XML (Ajax) when needed. This makes a web application able to update data without refreshing entire contents.

7.3 Web Application

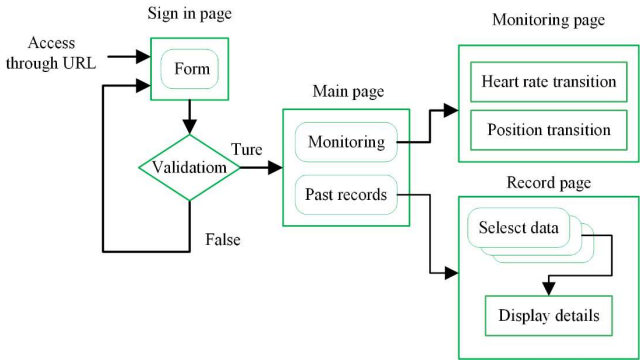

Fig. 7.3 Hierarchy diagram of web application.

The hierarchy diagram of the web application is depicted in Fig. 7.3. Each page is constructed by the Embedded JavaScript template (EJS) and rendered as HTML with CSS. In order to prevent privacy issues and to manage user data separately, the sign-in page verifies the users who access through a uniform resource locator (URL). The data accepted through the form component is validated with the database schema, which is stored on AWS RDS. The communication between the server and the database schema is conducted through middleware such as Express.js. After the process of validation returns true value, the users get access to other monitoring data.

The main page consists of two components, and each component calls back

the monitoring page or record page. The monitoring page is the page where the transition figures of heart rate and position are displayed. The displayed data dataset is transferred to the storage database schema. Furthermore, the heart rate and position transition are displayed as a chart rendered by the open-source JavaScript library, such as Google Charts.

The record page displays the preceding monitoring dataset by indexing it with date information. Thus, users can identify the difference between each table by interacting with table components and can check details of monitoring data such as waveform of heart rate signal, mean value of heart beats per minute (bpm), and monitored time. Data of images is loaded from the AWS S3.

7.3.1 Practical application

This study conducted an experiment of measuring data for T=120 seconds. Fig. 7.4 shows the transition of position data, and Fig. 7.5 depicts the heartbeat waveform. The former represents the position of true value, the exact position where the subject stands, obtained data by radar, and the data after database integration. Conversely, the latter represents the heartbeat waveform from the subject, which is measured by radar and electrocardiography (ECG) devices.

Fig. 7.6 and Fig. 7.7 are examples of running the web application, which is the monitoring and records pages, respectively. On the monitoring page, the user can check the transition of heart rate with a shifting time axis chart. Also, the position transition is noticed with the marker, which is refreshed by the timestamp. The monitoring page suggests the data of previous records so that the user can check or monitor their vital signs.

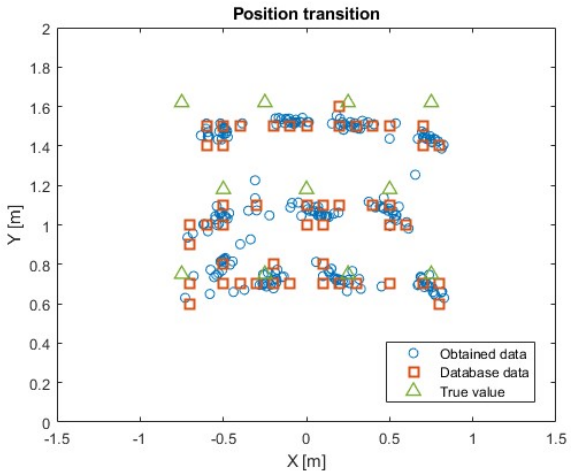

Fig. 7.4 The position transition.

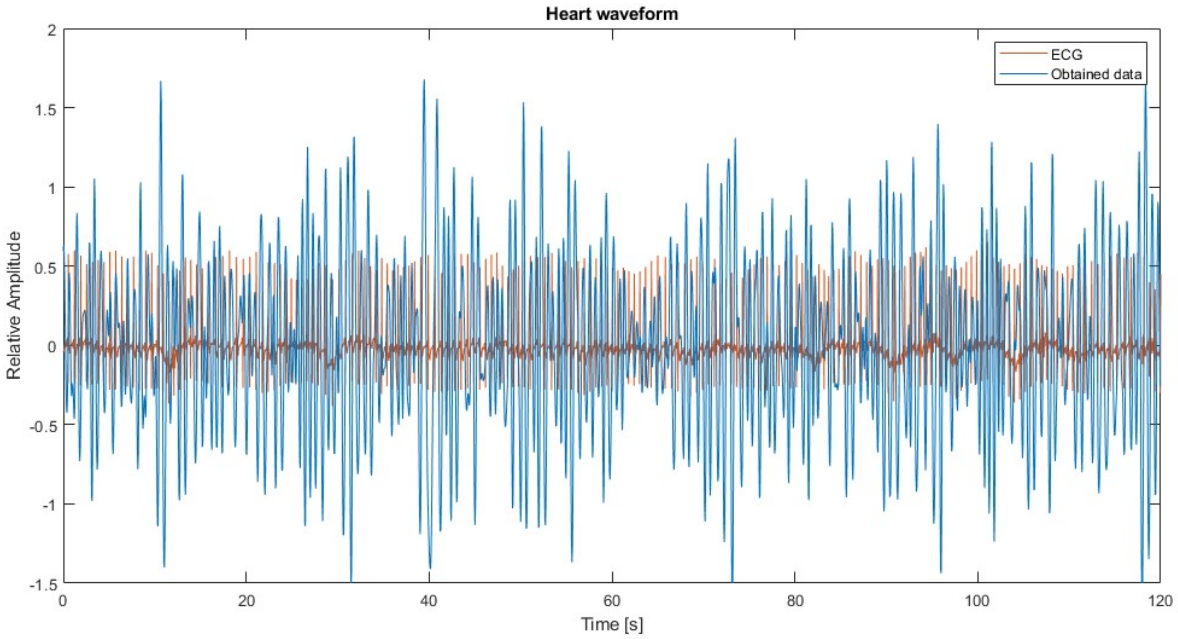

Fig. 7.5 The heartbeat waveform.

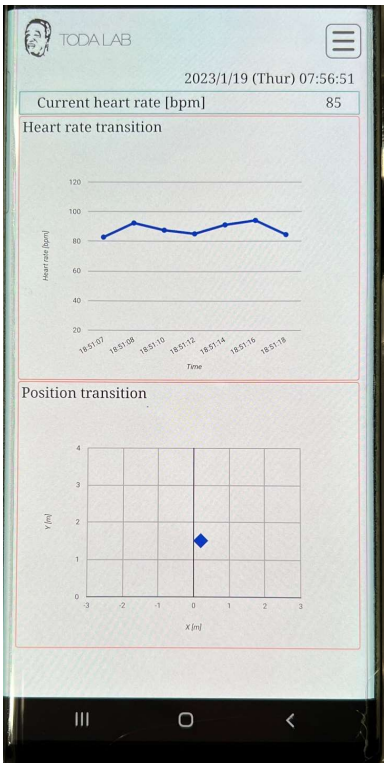

Fig. 7.6 The monitoring page.

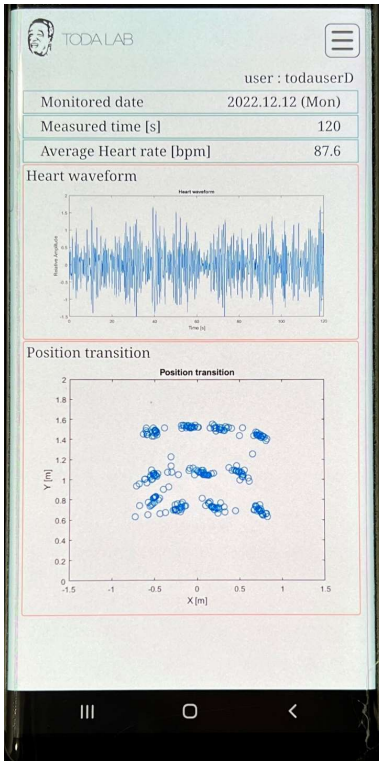

Fig. 7.7 The past records page.

7.4 Summary of Chapter 7

The system design in this study suggested a way of building a web application by connecting signal processing software with cloud service. Obtained data could be transferred immediately by utilizing cloud service, which increased the accessibility of monitoring data by radar. With potential audiences such as older people living alone, nursing homes, and medical isolation facilities, it has good application prospects. In the future, we consider making a parallel processing system configuration based on this design, which is expected to have little time latency.

Chapter 8 Conclusion

In this article, five vital signs measurement methods based on mm-wave FMCW radar proposed by the authors are presented. They are the PA-LI joint ICEEMDAN method, the improved adaptive range bin selection method, the radar joint stepping motor measurement method, the movable robot-based measurement method, and the web applications for real-time data visualization. These methods addressed the following five problems in this research field.

1. The problem of being able to measure only from the front or back of the person.

   Chapter 3 proposes a PA-LI joint ICEEMDAN method for mm-wave FMCW radar-based heart rate measurement. The method can address the effects of respiratory signal harmonics, adaptively decompose the radar vital sign to extract the heartbeat signal and estimate the heart rate. Meanwhile, the PA-LI method can effectively increase the SNR of ICEEMDAN heart IMF and make it more accurate to find the heart IMF spectrum's peak value. The mean value of the RMSE of heart rate estimation when the distance was 1 m was 3.08 bpm. Then, the reconstructed heartbeat signal has a high SNR, and the heart rate estimation is more accurate. Besides, we refined previous experimental approaches for investigating the influence of multi-directional observations on heart rate estimates. The experimental results show that the measurements' results in all directions (e.g., left, back, oblique front, and ceiling) are maintained at a high level of accuracy, except for the measurements from the "right" side, because the skin surface displacement

(due to the heartbeat) is basically not detected from the “right” side. Considering that non-contact heart rate measurement systems do not always face the subject in practice, in other words, the radar module is installed on the ceiling or high in the room to accommodate the real circumstances. Therefore, our proposed heart rate measurement method has the potential for practical applications.

2. The problem of being able to measure only when the subject remains stationary.

In Chapter 4, the author proposes a novel FMCW radar-based vital sign monitoring method for moving persons. The proposed improved adaptive range bin selection method efficiently selects the optimal range bin cells to obtain high-quality phase-change information, and the reconstructed heartbeat signal using the ICEEMDAN method is highly consistent with the ECG signal. The overall RMSE for heart rate estimation was 4.09 bpm, with an accuracy of 95.88%. The experimental results showed that the accuracy of the heart rate measurement remained high regardless of whether the subjects walked at 1 m/s or with the left side of their body facing the radar. Furthermore, random walk experiments have proved its good stability. Therefore, this measurement method has application potential.

3. The problem that the characteristics of the radar module limit the valid measurement range.

Chapter 5 proposes a novel radar-based adaptive tracking method for measuring the heart rate of a moving subject. The proposed algorithm is

employed to determine the position of the subject to control a stepping motor that adjusts the radar measurement range. The results of the fixed-route experiments revealed that when the subject was moving at a speed of 0.5 m/s, the mean values of RMSE for heart rate measurements were all below 2.85 bpm, and when moving at a speed of 1 m/s, they were all below 4.05 bpm. When subjects walked at random routes and speeds, the RMSE of the measurements were all below 6.85 bpm, with a mean value of 4.35 bpm. In addition, this study not only evaluated the potential effect of arm swing (more normal walking motion) on heart rate measurement but also demonstrated the ability of the proposed method to measure heart rate in a multiple-person scenario. Meanwhile, the overall measurement accuracy was greater than 96%, when the random route was included. Moreover, the RR intervals of the reconstructed heartbeat signal and ECG data were highly correlated, with a correlation coefficient of 0.9905.

4. The problem of measuring effectively when the subject is at a long distance.

   Chapter 6 proposes a novel remote heart rate measurement method based on radar and a mobility robot. The method adaptively adjusts the radar to be in an appropriate measurement position and can also measure heart rate while the subject walks. The mean absolute error was 0.063 Hz, and the mean accuracy was 95.47%.

5. The problem of how to visualize and upload measurement results to the application in real time.

Chapter 7 proposes a way of building a web application by connecting signal processing software with cloud service. Obtained data could be transferred immediately by utilizing cloud service, which increased the accessibility of monitoring data by radar. With potential audiences such as older people living alone, nursing homes, and medical isolation facilities, it has good application prospects.

Acknowledgments

This study not only reflects the results of my studies and research over the past few years but also condenses more of the support and help from my teachers, classmates, friends, and family. My supervisor, Prof. Toda, provided me with comprehensive and detailed guidance on the completion of my theses, from the selection of the topic, the formulation of the outline, and the commencement of the research work to the completion of the theses, all of which involved a great deal of Prof. Toda's efforts. Although he is usually busy at work, he often finds time to use e-mail, telephone, and other means to provide me with attentive guidance and support. He helped me to solve the problems and difficulties I encountered in my research so that I have taken fewer detours in my daily work and study. Also, I am very grateful to my classmates for helping me with the experiments and tedious data processing. And my family, they have given me every care and support in life and work, which has led to my current research results.

Finally, I express my deepest gratitude to my teachers and classmates who have supported, taught, and helped me in my studies and life during these years.

References

[1] A. Silvani, G. Calandra-Buonaura, Roger A. L. Dampney and P. Cortelli, “Brain–heart interactions: physiology and clinical implications,” physiology and clinical implications.Phil. Trans. R. Soc. A, no. 374, pp. 1–22, May 2016.

[2] F Sessa, V Anna, G Messina, G Cibelli, V Monda, G Marsala, M Ruberto, A Biondi, O Cascio, G Bertozzi, D Pisanelli, F Maglietta, A Messina, MP Mollica and M Salerno, “Heart rate variability as predictive factor forsudden cardiac death,” Aging (Albany NY), vol. 10, no. 2, pp. 166-177, Feb. 2018.

[3] United Nations, Department of Economic and Social Affairs, Population Division, “World Population Ageing 2019,” United Nations, New York, 2020. https://www.un.org/en/development/desa/population/theme/ageing/index.asp

[4] S. Yasuda, Y. Miyamoto and H. Ogawa, “Current Status of Cardiovascular Medicine in the Aging Society of Japan,” Circulation, vol. 138, no. 10, pp. 965-967, Sep. 2018.

[5] P. Mehrgardt, M. Khushi, S. Poon and A. Withana, “Deep Learning Fused Wearable Pressure and PPG Data for Accurate Heart Rate Monitoring,” IEEE Sensors Journal, vol. 21, no. 23, pp. 27106-27115, 1 Dec. 2021.

[6] D. Biswas, L. Everson, M. Liu, M. Panwar, B. Verhoef, S. Patki, C. H. Kim, A. Acharyya, C. V. Hoof, M. Konijnenburg and N. V. Helleputte, “CorNET: Deep Learning Framework for PPG-Based Heart Rate Estimation and Biometric Identification in Ambulant Environment,” IEEE Transactions on Biomedical Circuits and Systems, vol. 13, no. 2, pp. 282-291, Apr. 2019.

[7] E. Grooby, J. He, J. Kiewsky, D. Fattahi, L. Zhou, A. King, A. Ramanathan, A. Malhotra, G. A. Dumont and F. Marzbanrad, “Neonatal Heart and Lung Sound Quality Assessment for Robust Heart and Breathing Rate Estimation for Telehealth Applications,” IEEE Journal of Biomedical and Health Informatics, vol. 25, no. 12, pp. 4255-4266, Dec. 2021.

[8] S. Y. Lee, P. W. Huang, J. R. Chiou, C. Tsou, Y. Y. Liao and J. Y. Chen, “Electrocardiogram and Phonocardiogram Monitoring System for Cardiac Auscultation,” IEEE Transactions on Biomedical Circuits and Systems, vol. 13, no. 6, pp. 1471-1482, Dec. 2019.

[9] Syunsuke Sato, Ryosuke Koyanaka, Yaokun Hu and Takeshi Toda, “A Study of Frequency Selection Criterions for Discrete Wavelet Transform Without ECG-Data Reference in Heart Rate Estimation Using mm-Wave Radar,” 2021 International

Conference on Emerging Technologies for Communications (ICETC2021), D3-3, Dec. 2021.

[10] O. B. Lubecke, P. -. Ong and V. M. Lubecke, “10 GHz Doppler radar sensing of respiration and heart movement,” in Proceedings of the IEEE 28th Annual Northeast Bioengineering Conference (IEEE Cat. No.02CH37342), Philadelphia, PA, USA, 2002, pp. 55-56, Apr. 2002.

[11] C. Li, J. Cummings, J. Lam, E. Graves and W. Wu, “Radar remote monitoring of vital signs,” IEEE Microwave Magazine, vol. 10, no. 1, pp. 47-56, Feb. 2009.

[12] J. C. Lin, “Noninvasive microwave measurement of respiration,” Proceedings of the IEEE, vol. 63, no. 10, pp. 1530-1530, Oct. 1975.

[13] C. Li, V. M. Lubecke, O. Boric-Lubecke and J. Lin, “A Review on Recent Advances in Doppler Radar Sensors for Noncontact Healthcare Monitoring,” IEEE Transactions on Microwave Theory and Techniques, vol. 61, no. 5, pp. 2046-2060, May 2013.

[14] C. Li, Y. Xiao and J. Lin, “Experiment and Spectral Analysis of a Low-Power Ka-Band Heartbeat Detector Measuring From Four Sides of a Human Body,” IEEE Transactions on Microwave Theory and Techniques, vol. 54, no. 12, pp. 4464-4471, Dec. 2006.

[15] C. Li, Y. Xiao and J. Lin, “A 5GHz Double-Sideband Radar Sensor Chip in 0.18 μm CMOS for Non-Contact Vital Sign Detection,” IEEE Microwave and Wireless Components Letters, vol. 18, no. 7, pp. 494-496, Jul. 2008.

[16] C. Gu, C. Li, J. Lin, J. Long, J. Huangfu and L. Ran, “Instrument-Based Noncontact Doppler Radar Vital Sign Detection System Using Heterodyne Digital Quadrature Demodulation Architecture,” IEEE Transactions on Instrumentation and Measurement, vol. 59, no. 6, pp. 1580-1588, Jun. 2010.

[17] H. Zhao, H. Hong, L. Sun, Y. Li, C. Li and X. Zhu, “Noncontact Physiological Dynamics Detection Using Low-power Digital-IF Doppler Radar,” IEEE Transactions on Instrumentation and Measurement, vol. 66, no. 7, pp. 1780-1788, Jul. 2017.

[18] Antonio Lazaro, David Girbau, and Ramon Villarino, “Analysis of Vital Signs Monitoring Using an IR-UWB Radar,” Progress In Electromagnetics Research, vol. 100, pp. 265-284, Jan. 2010.

[19] J. Li, L. Liu, Z. Zeng and F. Liu, “Advanced Signal Processing for Vital Sign Extraction With Applications in UWB Radar Detection of Trapped Victims in

Complex Environments," IEEE Journal of Selected Topics in Applied Earth Observations and Remote Sensing, vol. 7, no. 3, pp. 783-791, Mar. 2014.

[20] A. G. Yarovoy, L. P. Ligthart, J. Matuzas and B. Levitas, "UWB radar for human being detection," IEEE Aerospace and Electronic Systems Magazine, vol. 21, no. 3, pp. 10-14, Mar. 2006.

[21] J. Li, Z. Zeng, J. Sun and F. Liu, "Through-Wall Detection of Human Being's Movement by UWB Radar," IEEE Geoscience and Remote Sensing Letters, vol. 9, no. 6, pp. 1079-1083, Nov. 2012.

[22] M. He,Y. Nian and Y. Gong, "Novel signal processing method for vital sign monitoring using FMCW radar," Biomedical Signal Processing and Control, vol. 33, pp. 335-345, Mar. 2017.

[23] D. Zhang, M. Kurata and T. Inaba, "FMCW Radar for Small Displacement Detection of Vital Signal Using Projection Matrix Method," International Journal of Antennas and Propagation , vol. 2013, ID 571986, Dec. 2013.

[24] A. Ahmad, J. C. Roh, D. Wang and A. Dubey, "Vital signs monitoring of multiple people using a FMCW millimeter-wave sensor," IEEE Radar Conference (RadarConf18), Oklahoma City, OK, 2018, pp. 1450-1455, Apr. 2018.

[25] L. Anitori, A. de Jong and F. Nennie, "FMCW radar for life-sign detection," IEEE Radar Conference, Pasadena, CA, 2009, pp. 1-6, May 2009.

[26] G. Wang, J. Muñoz-Ferreras, C. Gu, C. Li and R. Gómez-García, "Application of Linear-Frequency-Modulated Continuous-Wave (LFMCW) Radars for Tracking of Vital Signs," IEEE Transactions on Microwave Theory and Techniques, vol. 62, no. 6, pp. 1387-1399, Jun. 2014.

[27] Adib F., Mao H., Kabelac Z, D. Katabi and Robert C. M., "Smart homes that monitor breathing and heart rate," Proceedings of the 33rd annual ACM conference on human factors in computing systems, ACM, 2015, pp. 837-846, Apr. 2015.

[28] J. Muñoz-Ferreras, Z. Peng, R. Gómez-García and C. Li, "Random body movement mitigation for FMCW-radar-based vital-sign monitoring," IEEE Topical Conference on Biomedical Wireless Technologies, Networks, and Sensing Systems (BioWireleSS), Austin, TX, 2016, pp. 22-24, Jan. 2016.

[29] S. Wang, A. Pohl, T. Jaeschke, M. Czaplik, Marcus K., S. Leonhardt and N. Pohl, "A novel ultra-wideband 80 GHz FMCW radar system for contactless monitoring of vital signs," 2015 37th Annual International Conference of the IEEE Engineering in Medicine and Biology Society (EMBC), Milan, 2015, pp. 4978-4981, Aug. 2015.

[30] Yaokun Hu and Takeshi Toda, “Remote heart-rate estimation based on phase accumulation-linear interpolation method for mm-wave FMCW radar,” IEICE Communications Express, vol.10, no.2, pp.56-61, Feb. 2021.

[31] Yaokun Hu, Shunsuke Sato and Takeshi Toda, “Multi-directional Vital Signs Monitoring on Improved Complete Ensemble Empirical Mode Decomposition with Adaptive Noise using mm-Wave FMCW Radar,” 2020 International Conference on Emerging Technologies for Communications (ICETC 2020), A2-5, Dec. 2020.

[32] Yaokun Hu and Takeshi Toda, “The Effect of Multi-directional on Remote Heart Rate Measurement Using PA-LI Joint ICEEMDAN Method with mm-Wave FMCW Radar,” IEICE Transactions on Communications, vol. E105-B, No.2, Feb. 2022.

[33] Ryosuke Koyanaka, Shunsuke Sato, Yaokun Hu and Takeshi Toda, “A study on pre-filter design for improving accuracy in heart rate estimation from backside using discrete wavelet transform with mm-wave radar,” IEICE Communications Express, vol.10, no.12, pp.1009-1014, Dec. 2021.

[34] Yaokun Hu and Takeshi Toda, “A novel adaptive range-bin selection method for remote heart-rate measurement of an indoor moving person using mm-wave FMCW radar,” IEICE Communications Express, vol.10, no.5, pp.277-282, May 2021.

[35] Yaokun Hu and Takeshi Toda, “Remote Vital Signs Measurement of Indoor Walking Persons Using mm-Wave FMCW Radar,” IEEE Access, vol. 10, pp. 78219-78230, Jul. 2022.

[36] Xuanyu Peng, Yaokun Hu, Takeshi Toda, “Design and evaluation of remote tracking heart rate measurement based on millimeter-wave FMCW radar,” IEICE Communications Express, vol.11, no.6, pp.330-335, Jun. 2022.

[37] Yaokun Hu, Xuanyu Peng and Takeshi Toda, “A Novel Remote-tracking Heart Rate Measurement Method Based on Stepping Motor and mm-Wave FMCW Radar,” IEICE Transactions on Communications. (Oct. 18, 2023: Conditional Acceptance)

[38] Yaokun Hu, Xuanyu Peng and Takeshi Toda, “Vital signs monitoring mobility robot based on mm-wave FMCW radar,” IEICE Communications Express. (Oct. 30, 2023: Accepted)

[39] Joonyoung Lee, Yaokun Hu and Takeshi Toda, “An application for Remote Tracking Heart Rate Measurement Using mm-Wave Radar Module with Stepping Motor,” 2022 International Conference on Emerging Technologies for Communications (ICETC2022), S11-3, Dec. 1 2022.

[40] Yaokun Hu, Joonyoung Lee and Takeshi Toda, “A design of a web application for

remote vital signs monitoring and position using radar," IEICE Communications Express. (Under Review)

[41] Dennis R. Morgan and Michael G. Zierdt, "Novel signal processing techniques for Doppler radar cardiopulmonary sensing," Elsevier Signal Processing, vol. 89, issue 1, pp. 45-66, Jan. 2009.

[42] S. Sato, Y. Hu and T. Toda, "A Study of Multi-directional Heart-rate-estimation with Discrete Wavelet Transform and Band Pass Filter with 77 GHz-band FMCW Radar," IEICE 1st Int. Conf. on Emerging Technologies for Communs. (ICETC), G1-4, Dec. 2020.

[43] N.E. Huang, Z. Shen, S. R. Long, M. L. C. Wu, H. H. Shih e, Q. Zheng, N. C. Yen, C. Tung and H. H. Liu, "The Empirical Mode Decomposition and the Hilbert Spectrum for Nonlinear and Non-stationary Time Series Analysis," Proc. R. Soc. Lond. A, vol. 454, issue 1971, pp. 903-995, Mar. 1998.

[44] D. Yang, Z. Zhu and B. Liang, "Vital Sign Signal Extraction Method Based on Permutation Entropy and EEMD Algorithm for Ultra-Wideband Radar," IEEE Access, vol. 7, pp. 178879-178890, Dec. 2019.

[45] M. Adjrad, S. Dudley and M. Ghavami, "Experimental vital signs estimation using commercially available IR-UWB radar," 2014 Int. Radar Conf., Lille, pp. 1-4, Oct. 2014.

[46] R. Koyanaka, Y. Hu and T. Toda, "A Study of Heart Rate Estimation with Empirical Mode Decomposition for 77 GHz FMCW Radar" IEICE 1st Int. Conf. on Emerging Technologies for Communs. (ICETC), A4-1, Dec. 2020.

[47] Z. Wu and N.E. Huang, "Ensemble empirical mode decomposition: a noise-assisted data analysis method," World Scientific, Advances in Adaptive Data Analysis, Vol. 1, No. 1, pp. 1-41, 2009.

[48] M. E. Torres, M. A. Colominas, G. Schlotthauer and P. Flandrin, "A complete ensemble empirical mode decomposition with adaptive noise," IEEE Int. Conf. on Acoustics, Speech and Signal Processing (ICASSP), Prague, pp. 4144-4147, Jul. 2011.

[49] M. A. Colominas, G. Schlotthauer and M. E. Torres, "Improve complete ensemble EMD: A suitable tool for biomedical signal processing," Elsevier Biomedical Signal Processing and Control, vol. 14, pp. 19-29, Nov. 2014.

[50] M. Alizadeh, G. Shaker, J. C. M. D. Almeida, P. P. Morita and S. Safavi-Naeini, "Remote Monitoring of Human Vital Signs Using mm-Wave FMCW Radar," IEEE

Access, vol. 7, pp. 54958-54968, Apr. 2019.

[51] J. Wang, X. Wang, Z. Zhu, J. Huangfu, C. Li and L. Ran, “1-D Microwave Imaging of Human Cardiac Motion: An Ab-Initio Investigation,” IEEE Trans. on Microwave Theory and Techniques, vol. 61, no. 5, pp. 2101-2107, May 2013.

[52] T. Sakamoto, M. Muragaki, K. Tamura, S. Okumura, T. Sato, K. Mizutani, K. Inoue, T. Fukuda, and H. Sakai, “Measurement of instantaneous heart rate using radar echoes from the human head,” Electron. Lett., vol.54, no.14, pp.864-866, 2018.

[53] F. Zhu, K. Wang, and K. Wu, ‘‘A fundamental-and harmonic dual-frequency Doppler radar system for vital signs detection enabling radar movement self-cancellation,’’ IEEE Trans. Microw. Theory Techn., vol. 66, no. 11, pp. 5106–5118, Nov. 2018.

[54] Jingxia Zhang, Yinghai Guo, Yulin Shen, Difei Zhao and Mi Li, “Improved CEEMDAN–wavelet transform de-noising method and its application in well logging noise reduction,” Journal of Geophysics and Engineering, vol. 15, Issue 3, pp. 775-787, Jun. 2018.

[55] T. Sakamoto, P. J. Aubry, S. Okumura, H. Taki, T. Sato and A. G. Yarovoy, “Noncontact Measurement of the Instantaneous Heart Rate in a Multi-Person Scenario Using X-Band Array Radar and Adaptive Array Processing,” IEEE Journal on Emerging and Selected Topics in Circuits and System, vol. 8, no. 2, pp. 280-293, Jun. 2018.

[56] C. Ye, K. Toyoda and T. Ohtsuki, “A Stochastic Gradient Approach for Robust Heartbeat Detection with Doppler Radar Using Time-Window-Variation Technique,” IEEE Trans. on Biomedical Engineering, vol. 66, no. 6, pp. 1730-1741, Jun. 2019.

[57] W. Lv, Y. Zhao, W. Zhang, W. Liu, A. Hu and J. Miao, “Remote Measurement of Short-Term Heart Rate With Narrow Beam Millimeter Wave Radar,” IEEE Access, vol. 9, pp. 165049-165058, 2021.

[58] K. Shyu, L. Chiu, P. Lee, T. Tung and S. Yang, “Detection of Breathing and Heart Rates in UWB Radar Sensor Data Using FVPIEF-Based Two-Layer EEMD,” IEEE Sensors Journal, vol. 19, no. 2, pp. 774-784, 15 Jan.15, 2019.

[59] Y. Rong, K. V. Mishra and D. W. Bliss, “Multiple moving targets heartbeat estimation and recovery using multi-frequency radars,” in 2021 IEEE Radar Conference (RadarConf21), 2021, pp. 1-5.

[60] X. Yang, X. Zhang, H. Qian, Y. Ding and L. Zhang, “MMT-HEAR: multiple moving targets heartbeats estimation and recovery using IR-UWB radars,” in 2020 42nd Annual International Conference of the IEEE Engineering in Medicine & Biology

Society (EMBC), 2020, pp. 5733-5736.

[61] V. L. Petrović, M. M. Janković, A. V. Lupšić, V. R. Mihajlović and J. S. Popović-Božović, “High-Accuracy Real-Time Monitoring of Heart Rate Variability Using 24 GHz Continuous-Wave Doppler Radar,” IEEE Access, vol. 7, pp. 74721-74733, 2019.

[62] J. Park, Y. Jeong, G. Lee, J. Oh and J. Yang, “915-MHz Continuous-Wave Doppler Radar Sensor for Detection of Vital Signs,” Electronics 2019, 8, 561.

[63] H. Chuang, H. Kuo, F. Lin, T. Huang, C. Kuo and Y. Ou, “60-GHz millimeter-wave life detection system (MLDS) for noncontact human vital-signal monitoring,” IEEE Sensors Journal, vol. 12, no. 3, pp. 602-609, Mar. 2012.

[64] M. Sekine and K. Maeno, “Non-contact heart rate detection using periodic variation in Doppler frequency,” in 2011 IEEE Sensors Applications Symposium, 2011, pp. 318-322.

[65] M. Mercuri, Y. Liu, I. Lorato, T. Torfs, F. Wieringa, A. Bourdoux and C. V. Hoof, “A Direct Phase-Tracking Doppler Radar Using Wavelet Independent Component Analysis for Non-Contact Respiratory and Heart Rate Monitoring,” IEEE Transactions on Biomedical Circuits and Systems, vol. 12, no. 3, pp. 632-643, Jun. 2018.

[66] N. T. Phuong Nguyen, P. -Y. Lyu, M. H. Lin, C. -C. Chang and S. -F. Chang, “A Short-Time Autocorrelation Method for Noncontact Detection of Heart Rate Variability Using CW Doppler Radar,” in 2019 IEEE MTT-S International Microwave Biomedical Conference (IMBioC), 2019, pp. 1-4.

[67] G. Wang, C. Gu, T. Inoue and C. Li, “A hybrid FMCW-interferometry radar for indoor precise positioning and versatile life activity monitoring,” IEEE Trans. on Micro. Theory and Tech., vol. 62, no. 11, pp. 2812-2822, Nov. 2014.

[68] M. Shibao and A. Kajiwara, “Heart-rate monitoring of moving persons using 79 GHz ultra-wideband radar sensor,” IEICE Commun. Express, vol. 9, no. 5, pp. 125-130, Feb. 2020.

[69] A. Morimatsu, S. Matsuguma and A. Kajiwara, “Heart rate estimation of a moving person using 79GHz-Band UWB radar,” in 2019 IEEE Sensors Applications Symposium (SAS), Sophia Antipolis, France, pp. 1-5, May. 2019.

[70] I. Nejadgholi, S. Rajan and M. Bolic, “Time-frequency based contactless estimation of vital signs of human while walking using PMCW radar,” in IEEE 18th Int. Conf. on e-Health Networking, Applications and Services (Healthcom), Munich, pp. 1-6,

Sep. 2016.

[71] Y. Xiong, Z. Peng, C. Gu, S. Li, D. Wang and W. Zhang, “Differential Enhancement Method for Robust and Accurate Heart Rate Monitoring via Microwave Vital Sign Sensing,” IEEE Transactions on Instrumentation and Measurement, vol. 69, no. 9, pp. 7108-7118, Sep. 2020.

[72] L. Qiao X. Li, B. Xiao, M. He, X. Bi, W. Li and X. Gao, “Learning-Refined Integral Null Space Pursuit Algorithm for Noncontact Multisubjects Vital Signs Measurements Using SFCW-UWB and IR-UWB Radar,” IEEE Transactions on Instrumentation and Measurement, vol. 71, pp. 1-13, Art. 2022.

[73] X. Shang, J. Liu and J. Li, “Multiple Object Localization and Vital Sign Monitoring Using IR-UWB MIMO Radar,” IEEE Transactions on Aerospace and Electronic Systems, vol. 56, no. 6, pp. 4437-4450, Dec. 2020.

[74] H. Shen, C. Xu, Y. Yang, L. Sun, Z. Cai, L. Bai, E. Clancy and X. Huang, “Respiration and Heartbeat Rates Measurement Based on Autocorrelation Using IR-UWB Radar,” IEEE Transactions on Circuits and Systems II: Express Briefs, vol. 65, no. 10, pp. 1470-1474, Oct. 2018.

[75] P. Wang, F. Qi, M. Liu, F. Liang, H. Xue, Y. Zhang, H. Lv and J. Wang “Noncontact Heart Rate Measurement Based on an Improved Convolutional Sparse Coding Method Using IR-UWB Radar,” IEEE Access, vol. 7, pp. 158492-158502, Oct. 2019.

[76] W. Xia, Y. Li and S. Dong, “Radar-Based High-Accuracy Cardiac Activity Sensing,” IEEE Transactions on Instrumentation and Measurement, vol. 70, pp. 1-13, Art . 2021.

[77] L. Sun, S. Huang, Y. Li, C. Gu, H. Pan, H. Hong and X. Zhu, “Remote Measurement of Human Vital Signs Based on Joint-Range Adaptive EEMD,” IEEE Access, vol. 8, pp. 68514-68524, Apr. 2020.

[78] X. Zhang, Z. Liu, Y. Kong and C. Li, “Mutual Interference Suppression Using Signal Separation and Adaptive Mode Decomposition in Noncontact Vital Sign Measurements,” IEEE Transactions on Instrumentation and Measurement, vol. 71, no. 4001015, pp. 1-15, Art . 2022.

[79] T. K. V. Dai, K. Oleksak, T. Kvelashvili, F. Foroughian, C. Bauder, P. Theilmann, A. E. Fathy and O. Kilic, “Enhancement of Remote Vital Sign Monitoring Detection Accuracy Using Multiple-Input Multiple-Output 77 GHz FMCW Radar,” IEEE Journal of Electromagnetics, RF and Microwaves in Medicine and Biology, vol. 6, no. 1, pp. 111-122, Mar. 2022.

[80] J. Liu, Y. Li, C. Li, C. Gu and J. -F. Mao, “Accurate Measurement of Human Vital Signs With Linear FMCW Radars Under Proximity Stationary Clutters,” IEEE Transactions on Biomedical Circuits and Systems, vol. 15, no. 6, pp. 1393-1404, Dec. 2021.

[81] P. Zhao, C. X. Lu, B. Wang, C. Chen, L. Xie, M. Wang, N. Trigoni and A. Markham, “Heart Rate Sensing with a Robot Mounted mmWave Radar,” 2020 IEEE International Conference on Robotics and Automation (ICRA), pp. 2812-2818, Aug. 2020.

[82] K. Gupta, S. M. B., S. J, O. J. Pandey and L. R. Cenkeramaddi, "Automatic Contact-Less Monitoring of Breathing Rate and Heart Rate Utilizing the Fusion of mmWave Radar and Camera Steering System,” IEEE Sensors Journal, vol. 22, no. 22, pp. 22179-22191, 15 Nov.15, 2022.

[83] Q. Zheng, L. Yang, J. Li, T. Hu, J. Zhu, C. Song and Z. Xu, “A Target Detection Scheme With Decreased Complexity and Enhanced Performance for Range-Doppler FMCW Radar,” IEEE Transactions on Instrumentation and Measurement, vol. 70, no. 8001113, pp. 1-13, Art. 2021.

[84] V. V. Tien, T. Vu Hop, L. H. Nam, N. Van Loi and T. T. Thanh, “AN ADAPTIVE 2D-OS-CFAR THRESHOLDING IN CLUTTER ENVIRONMENTS: TEST WITH REAL DATA,” in 2018 5th International Conference on Signal Processing and Integrated Networks (SPIN), pp. 116-119, Sep. 2018.

[85] M. Kronauge and H. Rohling, “Fast Two-Dimensional CFAR Procedure,” IEEE Transactions on Aerospace and Electronic Systems, vol. 49, no. 3, pp. 1817-1823, Jul. 2013.

[86] T. K. V. Dai, Y. Yu, P. Theilmann, A. E. Fathy and O. Kilic, “Remote vital sign monitoring with reduced random body swaying motion using heartbeat template and wavelet transform based on constellation diagrams,” IEEE Journal of Electromagnetics, RF and Microwaves in Medicine and Biology, Jan. 2022.

[87] M. Li and J. Lin, “Wavelet-transform-based data-length-variation technique for fast heart rate detection using 5.8-GHz CW Doppler radar,” IEEE Transactions on Microwave Theory and Techniques, vol. 66, no. 1, pp. 568-576, Jan. 2018.

[88] Y. Hu and T. Toda, “A Study of Non-contact Heart Rate Monitoring Mobile Robot Using mm-Wave Radar,” IEICE Society Conference, B-19-12, Sep. 2023.

[89] R. A. Z. Daou, E. Aad, F. Nakhle, A. Hayek and J. Börcsök, “Patient vital signs monitoring via android application,” 2015 International Conference on Advances in

Biomedical Engineering (ICABME), Beirut, Lebanon, 2015, pp. 166-169.

[90] The MathWorks, Inc., “Transfer Data To Amazon S3 Buckets and Access Data Using MATLAB Datastore,” MATLAB & Simulink. https://www.mathworks.com/help/cloudcenter/ug/transfer-data-to-amazon-s3-buckets.html (accessed Oct 1, 2022).

[91] M. Tabassum and K. Mathew, “Software evolution analysis of linux (Ubuntu) OS,” in 2014 International Conference on Computational Science and Technology (ICCST), pp. 1-7, Aug. 2014.